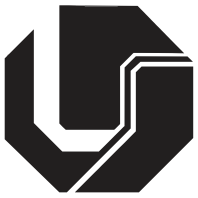

UNIVERSIDADE FEDERAL DE UBERLÂNDIA
FACULDADE DE ENGENHARIA MECÂNICA
PÓS-GRADUAÇÃO EM ENGENHARIA MECÂNICA

Detection and Control of Transverse Cracks on Rotating Machines

Leandro de Souza Leão

Uberlândia

2019

Leandro de Souza Leão

Detecção e Controle de Trincas Transversais em Máquinas Rotativas

Tese apresentada ao Programa de Pós-graduação em Engenharia Mecânica da Universidade Federal de Uberlândia, como parte dos requisitos para obtenção do grau de Doutor em Engenharia Mecânica.

Área de Concentração: Mecânica dos Sólidos e Vibrações
Linha de pesquisa: Dinâmica de Máquinas Rotativas

Prof. Dr. Valder Steffen Jr.,
Orientador

Prof. Dr. Aldemir Aparecido Cavalini Jr.,
Co-orientador

Prof. Dr. Washington Martins da Silva Junior
Coordenador do PPG em Engenharia Mecânica

Uberlândia
2019

Leandro de Souza Leão

Detecção e Controle de Trincas Transversais em Máquinas Rotativas

Tese apresentada ao Programa de Pós-graduação em Engenharia Mecânica da Universidade Federal de Uberlândia, como parte dos requisitos para obtenção do grau de Doutor em Engenharia Mecânica.

Área de Concentração: Mecânica dos Sólidos e Vibrações
Linha de pesquisa: Dinâmica de Máquinas Rotativas

Uberlândia, 29 de novembro de 2019.

Banca examinadora:

Prof. Dr. Valder Steffen Jr., Orientador (UFU)
Prof. Dr. Aldemir Aparecido Cavalini Jr., Co-orientador (UFU)
Prof. Dr. Francisco José de Souza (UFU)
Prof. Dr. Gregory Bregion Daniel (Unicamp)
Prof. Dr. Leopoldo Pisanelli Rodrigues de Oliveira (EESC - USP)

Ficha Catalográfica Online do Sistema de Bibliotecas da UFU
com dados informados pelo(a) próprio(a) autor(a).

L439 Leão, Leandro de Souza, 1987-
2019 Detection and Control of Transverse Cracks on Rotating Machines [recurso eletrônico] / Leandro de Souza Leão. - 2019.

Orientador: Valder Steffen Junior.
Coorientador: Aldemir Aparecido Cavalini Junior.
Tese (Doutorado) - Universidade Federal de Uberlândia, Pós-graduação em Engenharia Mecânica.
Modo de acesso: Internet.
Disponível em: http://doi.org/10.14393/ufu.te.2019.2515
Inclui bibliografia.

1. Engenharia mecânica. I. Steffen Junior, Valder, 1952-, (Orient.). II. Cavalini Junior, Aldemir Aparecido, 1983-, (Coorient.). III. Universidade Federal de Uberlândia. Pós-graduação em Engenharia Mecânica. IV. Título.

CDU: 621

Bibliotecários responsáveis pela estrutura de acordo com o AACR2:
Gizele Cristine Nunes do Couto - CRB6/2091
Nelson Marcos Ferreira - CRB6/3074

UNIVERSIDADE FEDERAL DE UBERLÂNDIA
Coordenação do Programa de Pós-Graduação em Engenharia Mecânica
Av. João Naves de Ávila, nº 2121, Bloco 1M, Sala 212 - Bairro Santa Mônica, Uberlândia-MG, CEP 38400-902
Telefone: (34) 3239-4282 - www.posgrad.mecanica.ufu.br - secposmec@mecanica.ufu.br

ATA DE DEFESA - PÓS-GRADUAÇÃO

Programa de Pós-Graduação em:	Engenharia Mecânica				
Defesa de:	Tese de Doutorado, nº 282, COPEM				
Data:	vinte e nove de novembro de dois mil e dezenove	Hora de início:	14:00	Hora de encerramento:	17:00
Matrícula do Discente:	11523EMC014				
Nome do Discente:	Leandro de Souza Leão				
Título do Trabalho:	Detection and Control of Transverse Cracks on Rotating Machinery				
Área de concentração:	Mecânica dos Sólidos e Vibrações				
Linha de pesquisa:	Dinâmica de Sistemas Mecânicos				
Projeto de Pesquisa de vinculação:					

Reuniu-se na Sala de Defesa da Pós Graduação 1M206- Bloco 1M, Campus Santa Mônica, da Universidade Federal de Uberlândia, a Banca Examinadora, designada pelo Colegiado do Programa de Pós-graduação em Engenharia Mecânica, assim composta: Professores Doutores: Aldemir Aparecido Cavalini Júnior - FEMEC/UFU; Francisco José de Souza - FEMEC/UFU; Valder Steffen Júnior - FEMEC/UFU, orientador do candidato. Ressalta-se que os Professores. Leopoldo Pisanelli Rodrigues de Oliveira - EESC/USP e Gregory Bregion Daniel - UNICAMP; participaram da defesa por meio de Skype desde a cidade de São Carlos/SP e Campinas/SP e os demais membros da banca e o aluno participaram *in loco.*

Iniciando os trabalhos o presidente da mesa, Dr. Valder Steffen Júnior, apresentou a Comissão Examinadora e o candidato, agradeceu a presença do público, e concedeu ao Discente a palavra para a exposição do seu trabalho. A duração da apresentação do Discente e o tempo de arguição e resposta foram conforme as normas do Programa.

A seguir o senhor(a) presidente concedeu a palavra, pela ordem sucessivamente, aos(às) examinadores(as), que passaram a arguir o(a) candidato(a). Ultimada a arguição, que se desenvolveu dentro dos termos regimentais, a Banca, em sessão secreta, atribuiu o resultado final, considerando o(a) candidato(a):

Aprovado.

Esta defesa faz parte dos requisitos necessários à obtenção do título de Doutor.

O competente diploma será expedido após cumprimento dos demais requisitos, conforme as normas do Programa, a legislação pertinente e a regulamentação interna da UFU.

Nada mais havendo a tratar foram encerrados os trabalhos. Foi lavrada a presente ata que após lida e achada conforme foi assinada pela Banca Examinadora.

Documento assinado eletronicamente por **Valder Steffen Junior**, **Professor(a) do Magistério Superior**, em 29/11/2019, às 16:36, conforme horário oficial de Brasília, com fundamento no art. 6º, § 1º, do Decreto nº 8.539, de 8 de outubro de 2015.

Documento assinado eletronicamente por **Aldemir Aparecido Cavalini Junior**, **Professor(a) do Magistério Superior**, em 29/11/2019, às 16:37, conforme horário oficial de Brasília, com fundamento no art. 6º, § 1º, do Decreto nº 8.539, de 8 de outubro de 2015.

Documento assinado eletronicamente por **Leopoldo Pisanelli Rodrigues de Oliveira**, **Usuário Externo**, em 29/11/2019, às 16:37, conforme horário oficial de Brasília, com fundamento no art. 6º, § 1º, do Decreto nº 8.539, de 8 de outubro de 2015.

Documento assinado eletronicamente por **Francisco José de Souza**, **Professor(a) do Magistério Superior**, em 29/11/2019, às 16:38, conforme horário oficial de Brasília, com fundamento no art. 6º, § 1º, do Decreto nº 8.539, de 8 de outubro de 2015.

Documento assinado eletronicamente por **GREGORY BREGION DANIEL**, **Usuário Externo**, em 29/11/2019, às 16:39, conforme

horário oficial de Brasília, com fundamento no art. 6º, § 1º, do Decreto nº 8.539, de 8 de outubro de 2015.

A autenticidade deste documento pode ser conferida no site https://www.sei.ufu.br/sei/controlador_externo.php?acao=documento_conferir&id_orgao_acesso_externo=0, informando o código verificador **1718431** e o código CRC **5FEC80D2**.

Referência: Processo nº 23117.102240/2019-54 SEI nº 1718431

Acknowledgements

Agradeço a Deus pela vida e saúde para realizar este trabalho tão desafiador. Agradeço a Ele também pelas pessoas tão especiais que Ele colocou no caminho para tornar esta jornada possível.

Agradeço ao professor Valder e ao professor Aldemir, meus orientadores, que não mediram esforços para me auxiliar. Mesmo com suas agendas lotadas com compromissos importantes, sempre havia tempo para mim e para os meus problemas. Ambos são grandes exemplos para mim, de trabalho, caráter, parceria e lealdade.

Agradeço aos colegas do laboratório (LMEst) que também estavam sempre à disposição para discutir os problemas da minha tese, bem como para me motivar e me fazer acreditar que daria tudo certo. Em especial, agradeço aos colegas: André, Felipe (Véio), Vinícius (Sushi), Iago, Marcus (Gaúcho), Adriano, Lucas (Batuta), Denner, Lázaro (Lazim), Philippe, Ulisses, Luiz Fernando (Cowboy), Izabela e Fabrício.

Um velho amigo, com quem tive a oportunidade de seguir quase toda minha vida profissional. Um grande irmão que a vida me deu, André. Muito obrigado por sempre pôr a amizade como a maior das prioridades.

Um novo amigo, que também se tornou um irmão. A você, Felipe, todo o meu respeito e admiração. Obrigado por nos fazer dar risada até de um msoquito voando. Manteremos nossa parceria, irmão, por onde caminharmos na vida.

Iago, outro amigo feito na época do doutorado, mas que a amizade será para sempre! Muito obrigado por todo aprendizado que construímos juntos.

Aos meus pais, José Roberto e Geni e às irmãs, Lara e Lucília, que sempre foram meu porto seguro. Muito obrigado por sempre me incentivarem e por me darem o suporte necessário para que eu pudesse voar.

À minha esposa Laysa e minhas filhas Isabela e Serena, que foram geradas durante este doutorado, meu muito obrigado. Vocês me deram raízes sem me tirar as

asas e me mostraram que ser feliz em família é muito mais forte do que ser feliz sozinho.

Em especial, muito obrigado Laysa, meu amor! Você é minha maior parceira e incentivadora. Obrigado por fazer dos meus sonhos os seus, por me motivar e me inspirar. Você enche meu coração de amor e me faz forte. Vou dar sempre o meu melhor pra você e pra nossa família.

Finally, I'd like to acknowledge professor Jerzy T. Sawicki, from the Center for Rotating Machinery Dynamics and Control (RoMaDyC), at Cleveland State University (CSU). You were a great advisor and showed me the power of team work. Thank you for all your advices and for believing in me.

Also, thank you so much, Alican Sahinkaya, from RoMaDyC. You were always ready to help me whenever I needed. You are the most intelligent, humble and easy going person I have ever known.

Thank you Andrea Bisconti. You were and will always be an angel in our lives. The most funny and life lover person of the whole world. Thank you for sharing your home with me and my family and for giving us such great moments.

Deus abençoe a cada um de vocês e lhes dê em dobro tudo o que vocês me deram neste período tão rico da minha vida!

À Laysa, Isabela e Serena,

com todo o meu amor!

Resumo

Leão, L. S. *Detecção e Controle de Trincas Transversais em Máquinas Rotativas*. Tese de Doutorado - Universidade Federal de Uberlândia, Novembro 2019.

Esta tese considera detecção e controle de uma trinca transversal em máquinas rotativas. Os objetivos deste estudo envolvem a obtenção e o ajuste de um modelo matemático que represente o comportamento dinâmico de uma máquina rotativa real, a aplicação numérica e experimental de um método de detecção de falhas baseado no sinal de vibração do rotor e de um método de controle ativo de trincas que reduza os níveis dos super-harmônicos $2X$ e $3X$ excitados pela presença da trinca no espectro de frequência do rotor. A novidade desta tese está no fato de se realizar detecção e controle de trinca em um único projeto de pesquisa. Além disso, o controle ativo de trincas ainda é um assunto novo nesta área. A modelagem matemática do rotor utiliza o método dos Elementos Finitos (FE) e considera elementos de viga de Timoshenko, com seção circular e raio constates. O comportamento dinâmico da trinca transversal é modelado pelo modelo de Mayes, que considera abertura e fechamento da trinca de maneira progressiva. Mecânica da fratura linear é aplicada, a fim de relacionar a profundidade da trinca com o aumento da flexibilidade do eixo. O observador de estado modal (MSO) foi utilizado nesta tese quando do estudo do problema de detecção de trincas. Já para o controle ativo da trinca, a técnica de controle PID foi aplicada. Os resultados evidenciam a possibilidade de se diagnosticar uma trinca e diminuir seus efeitos (através do controle ativo) sobre uma máquina rotativa em operação. Desta forma, manutenções que exigem a parada da máquina podem ser realizadas com menor frequência e, mesmo assim, a segurança da máquina rotativa é garantida.

Palavras-chave: Dinâmica de Máquinas Rotativas. Detecção de Trincas. Controle Ativo de Vibrações. Monitoramento da Integridade Estrutural . Auto-Reparação.

Abstract

Leão, L. S. *Detection and Control of Transverse Cracks on Rotating Machines*. PhD Dissertation - Federal University of Uberlândia, November 2019.

In this dissertation, crack detection and crack control of rotating machinery are addressed. The objectives of this study involves building and validating a numerical model capable of simulating the dynamic behavior of a real rotating machine. Numerical and experimental results for crack detection based on the shaft vibration signals are obtained. Besides, numerical and experimental results from an active control method, capable of suppressing $2X$ and $3X$ super-harmonics are obtained, excited by the crack presence. The innovation of this thesis lays on the fact of merging crack detection and crack control techniques in one single study. It is worth mentioning that the subject of crack control is quite new in the literature. The rotor is modeled by the finite element (FE) method, considering Timoshenko beam elements with circular cross section and constant radius. The Mayes model is addressed for simulating the breathing behavior of a transverse crack in a progressive way. The linear fracture mechanics theory is applied to correlate the crack depth with the corresponding additional shaft flexibility. The so-called modal state observer (MSO) technique was chosen to verify the existence of a transverse crack on a rotating machine. Moreover, the PID active control technique was addressed to perform crack control, suppressing crack signatures over the rotor frequency spectrum. Both numerical and experimental results highlight the possibility of detecting the existence of a crack and also how to decrease its effects (through active control) of an operating rotating machine. In this way, inspections requiring full stop of the machine can be performed less often while keeping the rotating machine safety.

Keywords: Rotordynamics. Crack Detection. Active Vibration Control. Structure Health Monitoring (SHM). Self-Healing (SH).

Publications

The research associated with the development of this PhD Dissertation resulted the publications listed below:

Journal Papers

- Leão. L. S., Cavalini Jr, A. A., Morais, T. S., Melo, G. P. and Steffen Jr, V. (2019). “Fault detection in rotating machinery by using the modal state observer approach”. Journal of Sound and Vibration, 458:123-142 (2019) 39:2447–2458, DOI 10.1016/j.jsv.2019.06.022

- Morais, T. S., Leão, L. S., Cavalini Jr, A. A. and Steffen Jr, V. (2019). "Rotating machinery health evaluation by modal force identification". Inverse Problems in Science and Engineering, DOI: 10.1080/17415977.2019.1644331

Conference Presentation and Proceedings

- Morais, T. S., Leão, L. S., Cavalini Jr, A. A. and Steffen Jr, V. (2017). "Rotating machinery health monitoring through modal force identification", Proceedings of the International Conference on Structural Engineering Dynamics ICEDyn, 3-5 July, 2017, Ericeria, Portugal.

- Leão. L. S., Cavalini Jr, A. A., Morais, T. S., Melo, G. P. and Steffen Jr, V. (2017). “Fault detection in rotating machinery by using the modal state observer approach”, Proceedings of the ASME 2017 International Design Engineering Technical Conferences and Computers and Information in Engineering Conference - IDETC/CIE, August 6-9, 2017, Cleveland, OH, USA. DETC2017-67044

- Leão. L. S., Sahinkaya, A., Cavalini Jr, A. A., Steffen Jr and Sawicki, J. T. (2018). “The influence of the vibration suppression on the rotor crack detection performance”, Proceedings of the International Federation for the Promotion of Mechanism and Machine Science IFToMM, 23-27 September, 2018, Rio de Janeiro, Brasil.

- Leão. L. S., Pereira, I. A., Cavalini Jr, A. A. and Steffen Jr (2019). “Vibration suppression on a rotating machine by the use of electromagnetic actuators and

a pid controller", Proceedings of the XXVI Congresso Nacional de Estudantes de Engenharia Mecânica, CREEM, Ilhéus/Itabuna, Ba.

- Pereira, I. A., Leão. L. S., Cavalini Jr, A. A. and Steffen Jr (2019). "Comparação de Amplificadores de Corrente para Sistemas de Controle Ativo de Vibração", Proceedings of the XXVI Congresso Nacional de Estudantes de Engenharia Mecânica, CREEM, Ilhéus/Itabuna, Ba.

- Leão. L. S., Pereira, I. A., Cavalini Jr, A. A. and Steffen Jr (2019). "A model-based crack identification approach", Proceedings of the 25th ABCM International Congress of Mechanical Engineering, October 20-25, 2019, Uberlândia, MG, Brasil, COBEM2019-0814 (ACCEPTED)

- Pereira, I. A., Del Claro, V. T. S., Leão. L. S., Oliveira, F. V., Cavalini Jr, A. A. and Steffen Jr (2019). "A Didatic Test-Rig for Teaching Vibration Modes", Proceedings of the 25th ABCM International Congress of Mechanical Engineering, October 20-25, 2019, Uberlândia, MG, Brasil, COBEM2019-0814 (ACCEPTED)

- Pereira, I. A., Leão. L. S., Sicchieri, L. C., Carvalho, V. N., Cavalini Jr, A. A. and Steffen Jr (2019). "Dynamic Characterizations of Electromagnetic Actuators ", Proceedings of the 25th ABCM International Congress of Mechanical Engineering, October 20-25, 2019, Uberlândia, MG, Brasil, COBEM2019-0814 (ACCEPTED)

Table of Contents

List of Figures

List of Tables

List of Symbols

Abbreviations

H_∞ H_∞ control synthesis

ABD Auto-Balancer Device

AMB Active Magnetic Bearing

CRDE Mutation Ration among the DE Individuals

DE Differential Evolution

DFFT Discrete Fast Fourier Transfer

dof Degrees of Freedom

EMA Electromagnetic Actuators

FDE Difference Amplification among the DE individuals

FE Finite Element

FFT Fast Fourier Transfer

FRF Frequency Response Function

GA Genetic Algorithms

GEP Generalized Equivalent Parameters

LMEst Laboratory of Structure Mechanics

LQR Linear Quadratic Regulator

LTI Linear Time-Invariant

MSO Modal State Observer

PD Proportional Derivative controller

PID Proportional Integral Derivative controller

SAE Society of American Engineers

SH Self-Healing

SHM Structural Health Monitoring

TF Transfer Function

UFU Federal University of Uberlândia

Greek Symbols

α width of the electromagnetic actuator central branch

α/D Crack depth, relative to the shaft diameter

α_x Crack depth

δ Shaft vibration, which continuously alters the air gap

$\Delta_{\mathbf{Kq}}$ Crack force

η Horizontal axis of the rotating frame

$\Im$ Magneto-motive force

μ Poisson's ratio

μ_o Constant air magnetic permeability

μ_r Relative magnetic permeability of each electromagnetic actuator

Ω Angular speed of the rotor (rev/min)

Ψ Total magnetic flux

ψ Magnetic flux

$\Re$ Reluctance of the magnetic circuit

ρ Volumetric density

θ Angular position of the rotating frame, in function of the fixed frame

θ_i Node rotating around the X direction

φ_i Node rotating around the Z direction

ϑ_y Constant which considers the shear effect of the Timoshenko beam element

ξ Vertical axis of the rotating frame

ξ_i Modal damping ratio of the i-th mode

Latin Symbols

$\bar{c}_c$ matrix containing the dimensionless additional flexibility terms

$\dot{z}_{mi}(t)$ Temporal velocity, associated with the i-th mode of vibration

$\hat{\mathbf{y}}(t)$ Observer output vector

$\mathbf{A}$ Dynamic matrix on the state space form

$\mathbf{A}_m$ Dynamic matrix on the modal block-diagonal state space form

$\mathbf{B}$ Input matrix on the state space form

$\mathbf{B}_m$ Input matrix on the modal block-diagonal state space form

$\mathbf{C}$ Output matrix on the state space form

$\mathbf{C}_m$ Output matrix on the modal block-diagonal state space form

$\mathbf{D}$ Damping matrix

$\mathbf{D}_g$ Gyroscopic matrix

$\mathbf{F}_u$ Unbalance force

$\mathbf{F}_{EMA}$ Control forces, fixed in space, applied by the electromagnetic actuators

$\mathbf{K}$ Stiffness matrix

$\mathbf{K}_C$ Stiffness matrix of a shaft containing a transverse crack

$\mathbf{k}_{FMayes}$ Cracked shaft stiffness in fixed coordinates

$\mathbf{k}_{RMayes}$ Cracked shaft stiffness in rotating coordinates

$\mathbf{L}$ Observer gain matrix

$\mathbf{M}$ Mass matrix

$\mathbf{Q}$ Observer gain associated with the Kalman filter method

$\mathbf{Q}$ Observer gain associated with the dynamic matrix, calculated by the Kalman filter method

$\mathbf{Q}$ Observer gain associated with the input matrix, calculated by the Kalman filter method

$\mathbf{q}$ Generalized coordinate vector

$\mathbf{W}$ Weight force

$\mathbf{x}(t)$ State vector of the real system

$\mathbf{y_h}(t)$ Vibration responses of the system in the healthy condition

$\mathbf{y_u}(t)$ Vibration responses of the system in the unknown condition

$\mathbf{y}(t)$ Real system output vector

$\mathbf{z_{mh}}(t)$ Modal state vector of the of the helathy system

$\mathbf{z_{mu}}(t)$ Modal state vector of the of the unknown system

$\mathbf{z}(t)$ State vector of the system observer

a, b, c, d, e, f Geometric parameters of the electromagnetic actuaotr

b Horizontal limit of the crack

B_1 Bearing 1

B_2 Bearing 2

C_i Cosine of i times θ

c_{ij} Additional flexibility term due to the crack

D_1 Disc 1

D_2 Disc 2

E Damage index

E Young modulus

e Air gap of the electromagnetic actuator

f Estimated density function

f_{mh} Estimated density function, associated with the healthy system

f_{mu} Estimated density function, associated with the unknown system

h Smoothing parameter of the Kernel function

h_x Height of the line passing at the infinitesimal square, considered inside the crack

I Electric current present on the coil

I_y Moment of inertia of area, with respect to the Y axis

k Control gain, which alters the control forces

K_D Derivative gain of the PID controller

K_e Kernel function

K_I Integrative gain of the PID controller

k_o Healthy shaft stiffness, along the ξ direction

K_P Proportional gain of the PID controller

$k_{\eta Mayes}$ Angular dependent cracked shaft stiffness, along the ξ direction

$k_{\xi Mayes}$ Angular dependent cracked shaft stiffness, along the ξ direction

K_{t_coup} Torsional stiffness of the coupling

K_{xx_b1} Stiffness of bearing 1, on the X direction

K_{xx_b2} Stiffness of bearing 2, on the X direction

K_{zz_b1} Stiffness of bearing 1, on the Z direction

K_{zz_b2} Stiffness of bearing 2, on the Z direction

L Magnetic inductance

N Number of windings on the electromagnetic actuator

P_i Mechanical efforts, acting on the cracked element

R Radius of the circular shaft cross section

s Complex frequency parameter, used at the Laplace domain

S_{ij_X} Displacement sensor at node #ij, measuring on the X direction

S_{ij_Z} Displacement sensor at node #ij, measuring on the Z direction

U_c Additional strain energy, due to the crack

u_i Node displacement on the X direction

w_i Node displacement on the Z direction

W_{mag} Magnetic energy

$z_{mi}(t)$ Temporal displacement, associated with the i-th mode of vibration

Chapter 1

Introduction

1.1 Introduction

This Ph.D. dissertation is organized according to two main parts. In the first part, the crack detection problem is addressed. In the second one, the crack control problem is studied. Thus, the main objective is to perform both structural health monitoring (SHM) and self-healing (SH) dedicated to the same engineering system, simultaneously. In this way, the present contribution aims at detecting the crack and then to control its severity, thus avoiding different types of structure failure.

1.2 Crack Detection

The development of online health monitoring techniques for crack detection in shafts of rotating machines were motivated by a series of accidents, such as the catastrophic failure, which occurred in a General Electric Co. turbine in the early 70s, Dimarogonas et al. (2013). After 1972, as a continuation of Dimarogonas work, Pafelias (1974) published a formal General Electric Co. report proposing a methodology for crack detection based on the monitoring of the $2X$ super-harmonic and the half critical speed sub-harmonic, Dimarogonas (1996). A considerable academic effort on crack detection techniques was observed along the 80s, resulting high economic impact in various industries. Researches on structural health monitoring (SHM) techniques for early fault detection has been growing since then.

According to Cavalini-Jr. et al. (2015), there have been several SHM techniques

proposed in the literature for crack detection in rotating machines. Visual examination, radiographic tests, ultrasonic tests, and dye penetrant inspection are examples of widely used non-destructive techniques for crack detection. However, these methods have proved to be costly since satisfactory results rely on detailed and periodic inspections, according to Saavedra and Cuitiño (2001). As a full stop of the machinery is required for inspection, production losses proportional to the time spent on these inspections are verified, which is undesirable by the industry.

Therefore, SHM techniques based on vibration measurements, which may occur continuously while the machine deliveries power, are much more interesting and industry applicable, according to Cavalini-Jr. et al. (2015), Doebling et al. (1998), Darpe et al. (2004). Consequently, SHM techniques help to increase both the equipment's lifetime and operation safety throughout the aging of the system.

According to Carden and Fanning (2004), the SHM techniques based on vibration signals are sensitive to mass, damping, and stiffness changes in the structure, which may indicate the presence of faults. Cavalini-Jr. et al. (2016) mention that nowadays it is already possible to identify incipient cracks (i.e., which has a depth smaller than 25% of the shaft diameter) in rotors by applying sophisticated SHM methods.

The developement of vibration-based SHM techniques require both experimental and numerical approaches. This means that a reliable rotor mathematical model needs to be derived. These techniques are called model-based, and the quality of their results depends directly on the accuracy of the mathematical model used for representing the real rotating machine.

If these techniques are not applied, accidents may occur. One of the most important and recent turbine accidents, caused by fatigue cracks, took place on Sayano-Shushenskaya hydroelectric power station.

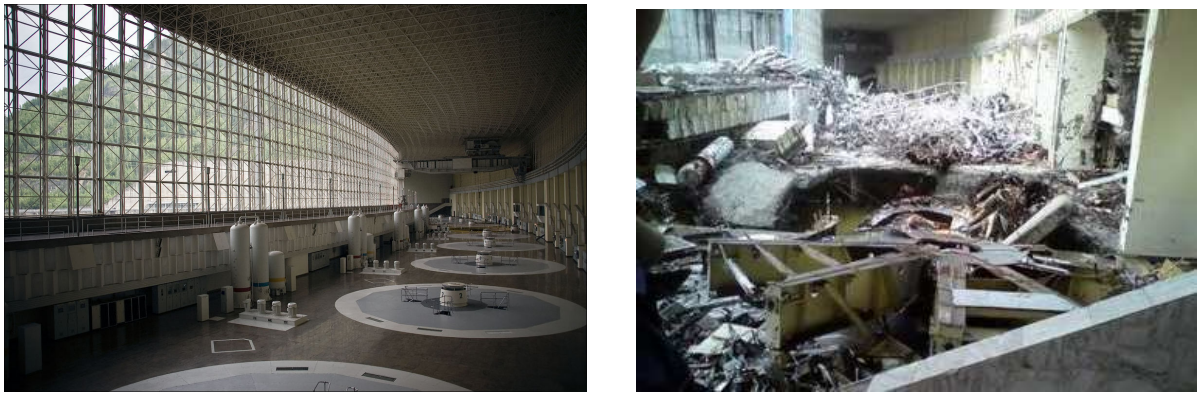

(a) (b)

Figure 1.1: Turbine hall of the power station: (a) before, and (b) after the accident. Source: http://4044415.livejournal.com/51884.html

Figure 1.1 presents the hall of turbines of the power station before, and after the accident, which caused 75 people casualties.

The main results of this first part of the present dissertation was published in Leao et al. (2019), which followed the methodology presented by Cavalini-Jr (2009) to derive a fault detection technique based on the so-called modal state observer (MSO). There are several model-based techniques dealing with crack detection, and quite often new methods are proposed. A brief state-of-the-art is now presented for highlighting the main contributions to this field.

1.3 State-of-the-Art for Crack Detection

According to Zhao (2013), the first model-based approach devoted to fault detection in mechanical systems was proposed by Isermann (1995). Before that, only experimental techniques were used Pafelias (1974). The model-based technique developed by Isermann (1995) was applied to various mechanical systems, such as electric motors, actuators, pumps, and machine tools, presenting encouraging results.

On the rotating machinery field, Bachschmid et al. (2000) presented the possibility of identifying the crack existence in a rotating machine by using a model-based technique allied to the $1X$, $2X$, and $3X$ harmonic components of the vibration responses. It is important to perform SHM on rotating machinery to early detect fatigue cracks. This

is the context of the first part of this Ph.D. dissertation.

Some other SHM methods are briefly cited. Market et al. (2001) proposed a model-based approach in which the crack was identified over the rotor by relating the fault parameters with fictitious equivalent forces. Sawicki et al. (2011) have experimentally detected a crack by applying specified harmonic forces on the rotor by means of a single magnetic bearing. The presence of the damage led to spectral responses with additional peaks at frequencies that are combinations of the rotor speed, its critical speed, and the frequency of the diagnostic force. Cavalini-Jr (2013) applied the combination resonance method, combined with the multiple scales non-linear approach, for deriving numerical results for different crack conditions. This author also performed experimental tests on a test-rig found at the LMEst laboratory, at the Federal University of Uberlândia (UFU). Later, Cavalini-Jr. et al. (2016), also performed model-based combination resonances SHM techniques together with a pseudo-random optimization code, known as Differential Evolution (DE), in order to characterize the signatures of the crack in the spectral responses of a flexible rotor.

The MSO technique was chosen in this study, among other methods, because it is capable of combining the main advantages of both time and modal domain analyses, as described in Cavalini-Jr et al. (2008). It is well known that time-domain vibration responses are more sensitive than modal characteristics (natural frequencies and mode shapes) for performing fault detection in mechanical systems. However, interesting information can be obtained by monitoring modal parameters. Besides, only converting the time domain vibration responses to the modal domain does not ensure that it will become more sensitive to the fault presence. Thus, according to Cavalini-Jr et al. (2008), the MSO serves as a filter designed specifically for crack detection in combination with the mathematical model of the system.

This is possible because the mathematical model of the healthy system is incorporated into the MSO, which is tuned to estimate the vibration responses of the system for its healthy condition. Then, the estimated modal vibration responses are compared with a baseline (i.e., modal vibration response of the healthy rotor) for crack detection purposes. Amplitude increases on $2X$ or $3X$ super-harmonics are due to the existence of a transverse crack.

Mohamad et al. Mohamad et al. (2018a), Mohamad, Samadani, and Nataraj Mo-

hamad et al. (2018b), and Mohamad et al. Mohamad et al. (2019) demonstrate that vibration signals acquired in high sampling frequencies are more sensitive for damage existence in gears, rolling bearings, and cracked shafts. These works show that much information useful for damage detection is found on time vibration responses. Otherwise, only severe faults can be detected in mechanical systems if only natural frequencies and mode shapes are monitored. However, interesting information can be obtained by using modal parameters, such as stiffness and damping properties.

For the MSO technique applied in this dissertation, the condition monitoring is based on the kernel density function estimate, which is able to deal with the probability density estimation of a given data sample. The mathematical model of the rotating machine is formulated according to the FE method by considering the Timoshenko beam theory. The crack behavior is simulated according to the Mayes model and the additional flexibility in the shaft, related to the crack depth, is determined through the linear fracture mechanics theory. Numerical and experimental results obtained demonstrated that the MSO technique represents a good alternative to detect faults in rotating machines.

1.4 Crack Control

The second part of this Ph.D. study lays on the vibration control context. In this way, active vibration control is applied for suppressing the effects of a transverse crack along a rotating machine (decreasing $2X$ and $3X$ super-harmonics amplitudes).

Koroishi (2013) designed a test rig for performing vibration control studies for his Ph.D. dissertation, at the same LMEst laboratory, at the Federal University of Uberlândia (UFU). A similar test rig was also mounted for the present research work, serving from the components designed by Koroishi (2013). Some hardware updating was performed and it is explained in Chap.6. There are several references in the literature about control applications as used in rotating machinery. In this way, a state-of-the-art on this subject is furnished, for placing the present research effort.

1.5 State-of-the-Art for Crack Control

Koroishi (2013) compared various active control methods to be applied on a rotating machine with one fixed bearing and one hybrid bearing. The hybrid bearing was able to both support and move the rotating shaft by the action of four electromagnetic actuators (EMAs) in order to compensate for the shaft lateral vibrations. In this context, the above mentioned author compared the following active control methods: LQR, H_∞, and Fuzzy logic. The controlled rotor was tested under several conditions, such as run-up, run-down, steady state, and at rest. The results obtained, both numerically and experimentally, demonstrate the success of active control techniques in reducing lateral vibrations of the shaft.

The control action under the shaft lateral vibrations is quite important, since it increases the rotor efficiency regarding power delivering, prevents premature bearing failures, decreases the machine shutdown and maintenance frequencies, besides preventing rotor failure, Koroishi (2013). For reaching this objective, there are three control strategies to be considered, namely passive, semi-active, and active.

Still, according to Koroishi (2013), passive vibration control is usually obtained by modifying dynamic characteristics of the machine, such as mass, stiffness, or damping. An example of a passive controller of a rotating machine is presented in Ribeiro et al. (2015). In their work, they present a robust methodology based on generalized equivalent parameters (GEP) for the optimal design of viscoelastic supports of rotating machinery. The control approach aims at for minimizing the unbalance frequency response. For this purpose, a hybrid optimization technique, which combines genetic algorithms (GA) and Nelder–Mead method, was performed. Figure 1.2 presents the viscoelastic support developed by the authors.

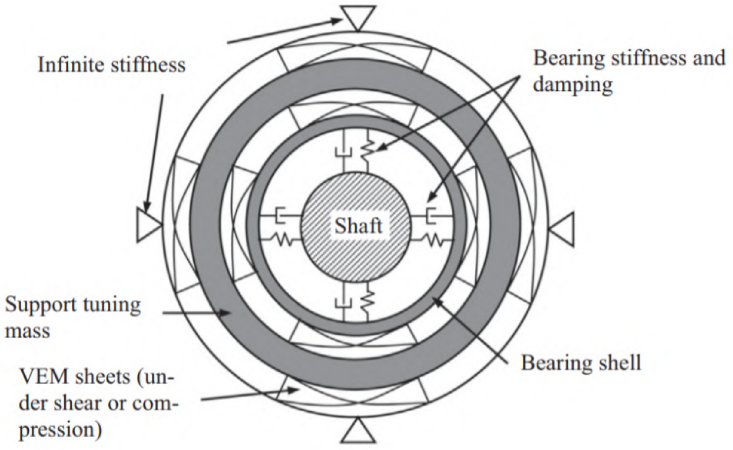

Figure 1.2: Viscoelastic Support; extracted from Ribeiro et al. (2015).

Ribeiro et al. (2015) performed numerical tests and concluded that the use of viscoelastic supports absorbs 97.5% of the shaft lateral vibrations, as compared to ball bearings and 86.4% compared to hydrodynamic bearings.

As an example of the application of a semi-active vibration controller of rotating machines, Jung and DeSmidt (2018) presented the results of an auto-balancer device (ABD). According to this author, auto-balancers contain freely moving eccentric masses, which naturally adjust to cancel the rotor unbalances at certain operating speeds. This passive device is capable of applying unbalance changes without requiring power, sensors, or a control system. Moreover, under certain conditions, such as the unstability limit condition, the passive control is switched to an active control law that drives an active magnetic bearing (AMB) for suppressing the vibrations for a given speed range. Then, the active controller is turned off once the system moves into the estimated region of attraction, where the passive device is able to deal with the system vibrations again. Figure 1.3 presents the passive device considered in the above mentioned reference.

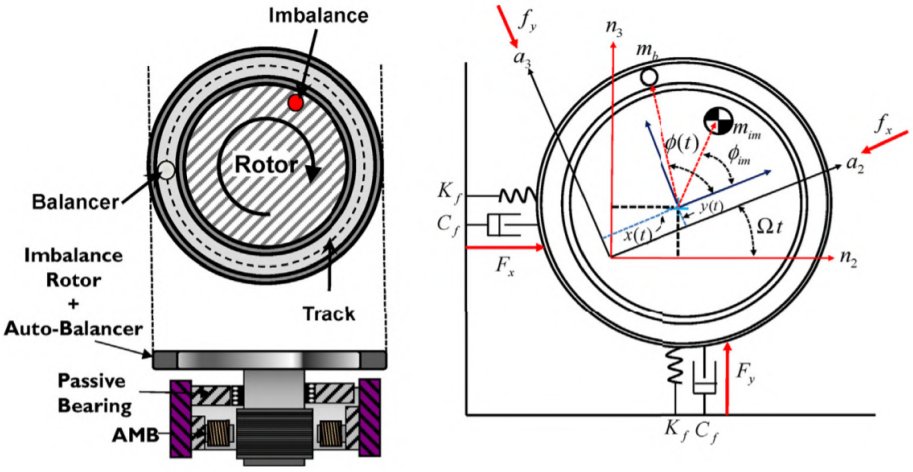

Figure 1.3: Auto-balancer device (ABD) scheme with its rigid and rotating frames depicted; extracted from Jung and DeSmidt (2018).

Jung and DeSmidt (2018) concluded that the simulation results demonstrate that the hybrid ABD/AMB system is able to control the rotor unbalance vibrations efficiently. Both devices complemented each other's function. This semi-active control system may be relevant to limited power applications such as satellite reaction wheels or flywheel energy storage batteries.

Other applications of active vibration control can be found in the literature, such as Koroishi et al. (2012), Morais et al. (2012), Morais et al. (2013). However, in the present dissertation, the focus is not only on actively controlling shaft lateral vibrations. The active control law, applied to the EMAs is expected to decrease crack signatures ($2X$ and $3X$ super-harmonics) from the rotor frequency signal responses. This technique was not found in the state-of-the-art performed for this Ph.D. dissertation.

1.6 Objectives and Contributions of this Ph.D. work

The main objectives of this research work are the following:

1. Detect a crack along a rotating machine;
2. Use control action on the rotor to keep crack size and crack severity below a defined threshold.

For both objectives, the results are obtained numerically and validated experimentally on the test-rig found at the LMEst laboratory, at the Federal University of Uberlândia (UFU), Brazil.

There are also some other objectives regarding this Ph.D. dissertation, among which the main ones are listed in the following:

1. Update the LMEst numerical Finite Element (FE) codes related to rotating machinery;

2. Compare different crack detection techniques for choosing the best adapted one to be used in the context of the present research work;

3. Mount and validate the test-rig to perform crack detection techniques at the LMEst laboratory;

4. Compare different crack control techniques for choosing the best adapted one to be used in the context of the present work;

5. Mount and validate the test-rig to perform crack control under laboratory conditions.

1.7 Organization of this Ph.D. dissertation

Besides this first chapter, which introduces the context, objective, and contributions of this Ph.D. work, six additional chapters complete this dissertation. A brief description of each chapter is provided below.

Chapter 2 presents the test-rig to be used for crack detection studies. It starts by describing the main components of the test-rig. The equation of motion of the system is derived by using the FE model to simulate the dynamic behavior of the test rig. Finally, it presents the model updating procedure used for validating the numerical model by fitting this model to the experimental data from the test-rig.

Chapter 3 presents the application of the chosen model-based crack detection method, i.e., the Modal State Observer. This method is applied to the numerical model built in Chap. 2. Details about the MSO modeling, besides crack modeling details, are

discussed in Chap. 3. Numerical and experimental results concerning crack detection are presented in this chapter.

In Chap. 4, the test-rig to be used for the crack control studies is described. This chapter follows the same steps of Chap. 2, describing the test-rig main components and also introducing the equation of motion that is able to simulate the test-rig dynamic behavior. Finally, the updating results for the validation of the numerical model are furnished.

Chapter 5 is devoted to describing the control actuators to be used in this work, i.e., the electromagnetic actuators - EMAs. A brief electromagnetism background is revisited, introducing the main concepts to be applied to the present work. It is also explained how to model the EMA behavior and how to introduce the EMA into the FE model developed in Chap. 5.

In Chap. 6 , the crack control studies are presented. For this purpose, PID concepts are described and some control background is reviewed, presenting the poles and zeros meaning, and how the control characteristics influences the stability of the system. In the sequence, numerical and experimental PID results devoted to crack control are discussed.

Finally, the conclusions are drawn in Chap. 7, which also suggests some future research directions.

Lastly, bibliographic references are provided.

Chapter 2

Crack Detection in Rotating Machinery

2.1 Introduction

In this chapter, the test rig used to test the various techniques devoted to crack detection is presented together with its main components, which are described in detail. In the sequence, the equation of motion of the rotor is solved by a numerical FE model. Finally, the numerical updating procedure is described, both in the time and frequency domain. The goal is to obtain a representative numerical model of the rotating system, so that numerical and experimental results are satisfactorily comparable. Then, it is possible to develop a reliable crack detection approach.

2.2 Rotor Test Rig for Crack Detection

In the present work, two dedicated test rigs were built. The first one is used for crack detection tests, and the second is used for crack control (see Chap.4).

This chapter is devoted to present the test rig used for generating all the experimental data used for the crack detection part of this dissertation. This test rig is found at the Laboratory of Mechanical Structures (LMEst) of the Federal University of Uberlândia (UFU), as presented in Fig.2.1(a), while its corresponding FE mesh is presented in 2.1(b).

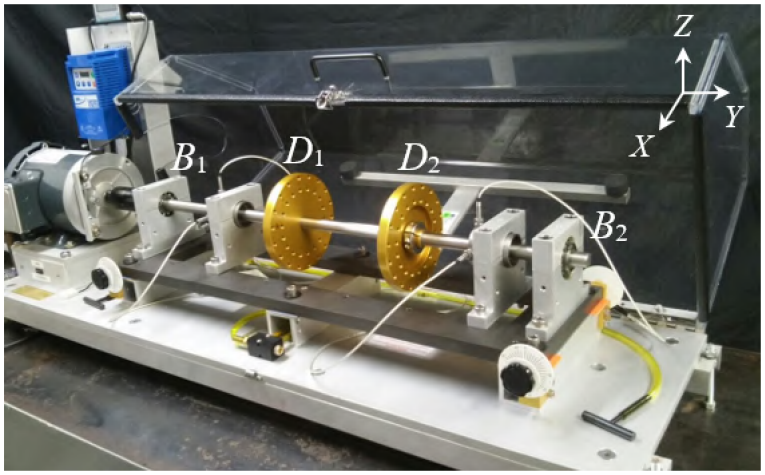

(a)

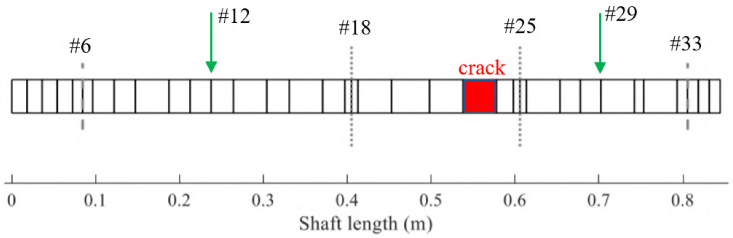

(b)

Figure 2.1: Test rig used for performing crack detection: (a) rotating machine; (b) FE model.

This test rig was manufactured by Spectra Quest Inc., model $Machinery\ Fault\ \&\ Rotor\ Dynamics\ Simulator$ and was mounted on a vibration isolated table so that external vibration influences are attenuated. The flexible shaft was made of SAE 1045 steel, rectified type $h7$ and has a diameter of $19\ mm$ and is $850\ mm$ long. Its main mechanical properties are the following: $E = 182\ GPa$, $\rho = 7930\ kg/m^3$, and $\mu = 0.29$. The numerical model for representing the rotating machine behavior was developed by using the FE method, and its mesh was discretized in 35 elements. More details of the FE model will be presented later in the section 2.3. Two aluminum rigid discs are coupled to the shaft, namely D_1 $(0.658\ kg)$, at node $\#18$ and D_2 $(0.656\ kg)$, at node $\#25$. The shaft contains a 50% relative depth crack, which is described in section 3.5.

A transverse crack with 50% relative depth was produced in this shaft at the position of element $\#22$, as depicted by Fig.2.2. Crack modeling is detailed in Chap.3.

Figure 2.2: Transverse crack on the shaft.

A double row self aligning ball bearing furnished by FAG®, model $1204-K-TVH-C3$ supports the shaft, as shown in Fig 2.3. The bearings B_1 and B_2 are located at the nodes $\#6$ and $\#33$, respectively.

Figure 2.3: Self aligning ball bearing.

The bearings are mounted on two aluminium rigid bases, as shown in figure 2.4.

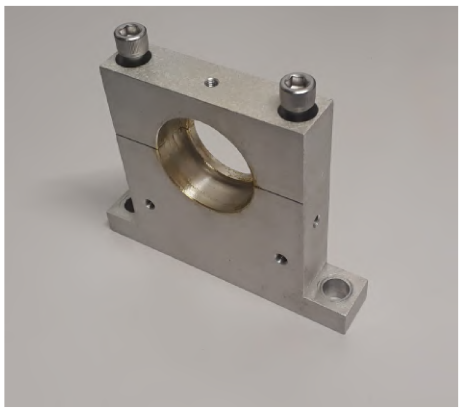

Figure 2.4: Bearing rigid base.

Displacement sensors are orthogonally mounted at the nodes $\#12$ (S_{12_X} and S_{12_Z}) and $\#29$ (S_{29_X} and S_{29_Z}) to collect the shaft vibration responses. The proximity probes used are made by SKF®, model CMSS 65-002-00-12-10, and their drivers are also

from SKF®, model CMSS 665. These sensors, are able to work linearly in the range from 0 to 2 mm and are shown by Fig. 2.5.

Figure 2.5: Proximity probes.

An alternative current electric motor Marathon®, model $VC56T34F5301J$, possessing $1/2\ hp$ of power and a maximum speed of $3450\ rev/min$ is used in the test rig to drive the shaft. It is shown in Fig. 2.6.

Figure 2.6: Shaft driving system.

Figure 2.6 also presents a Lenze® frequency inverter, type $ESV371N01SXB$, which is responsible for setting the shaft at a chosen rotating speed.

A RoCom® flexible coupling, model $DT000175 - C.750 - C.625$ (shown in Fig. 2.7) was used for filtering misalignment and axial motions coming from the motor to the shaft.

Figure 2.7: Self aligning ball bearing.

2.3 Rotor Equation of Motion

According to Lallane and Ferraris (1997), a mathematical model capable of representing the dynamic behavior of a rotating machine is given by:

$$\mathbf{M}\ddot{\mathbf{q}} + [\mathbf{D} + \Omega\mathbf{D}_g]\,\dot{\mathbf{q}} + \mathbf{K}\mathbf{q} = \mathbf{W} + \mathbf{F}_u \tag{2.1}$$

where $\mathbf{M}$ stands for the mass matrix, $\mathbf{D}$ represents the damping matrix, $\mathbf{D}_g$ is the gyroscopic effect and $\mathbf{K}$ is the stiffness matrix. All these matrices are related to moving parts of the rotating machine, such as disks, couplings and shaft. The generalized coordinate vector is represented by $\mathbf{q}$ and the rotating speed, by Ω. On the right hand side of Eq.2.1, the forces are presented, such as $\mathbf{W}$, the weight force, and $\mathbf{F}_u$, the unbalance force.

This section contains the general approach on how to obtain the numerical model and how to validate it by using the experimental rotor responses. Details are not included since they have been already extensively explained in previous books and dissertation. For the interested reader, the full description on how to obtain the matrices $\mathbf{M}$, $\mathbf{D}$, $\mathbf{D}_g$, $\mathbf{K}$, and the forces $\mathbf{W}$, and $\mathbf{F}_u$ is found in the reference Lallane and Ferraris (1997).

As previously mentioned, the equation of motion (Eq.2.1) was solved by the FE method, which considers the Timoshenko beam theory to describe the shaft finite elements. Each element possesses two nodes, as depicted in Fig.2.8. It was considered 4 degrees of freedom per node, being two displacements (u_i and w_i) and two rotations (θ_i and φ_i), where $i = 1, 2, ..., nodes$.

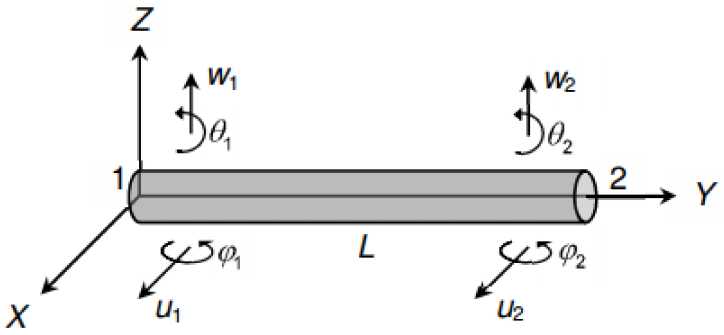

Figure 2.8: Finite element representing the shaft.

In this way, the generalized coordinate vector, for the first element, becomes:

$$\mathbf{q} = \begin{bmatrix} u_1 & w_1 & \theta_1 & \varphi_1 & u_2 & w_2 & \theta_2 & \varphi_2 \end{bmatrix}^T \tag{2.2}$$

The elementary matrices are mounted by considering this coordinate vector and the connectivity matrix. Finally, global FEM matrices are determined. The frequency and time responses from this model are then compared with those stemming from the test rig both for validation and model updating purposes.

2.4 System Reduction - Pseudo Modal Method

The physical FE model possesses very high order matrices (nxn), where $n = dof = 144$. Then, when the system is converted to the state space form, these matrices become $(2nx2n)$.

It is not convenient to consider matrices with such a high order because of the computational cost. In this way, it is preferable to consider the system in the modal domain, taking into account only its natural modes of interest. Thereby, the system order is considerably reduced.

According to Skogestad and Postlethwaite (2005) the Hankel singular values distribution may be used for measuring the relative energy of each state with respect to the whole system. Consequently, one may choose how many states should be considered for obtaining a good representation of the system.

Figure 2.9 presents the Hankel singular values distribution for the rotating machine considered in this dissertation, presented in Chap.4, in the modal domain.

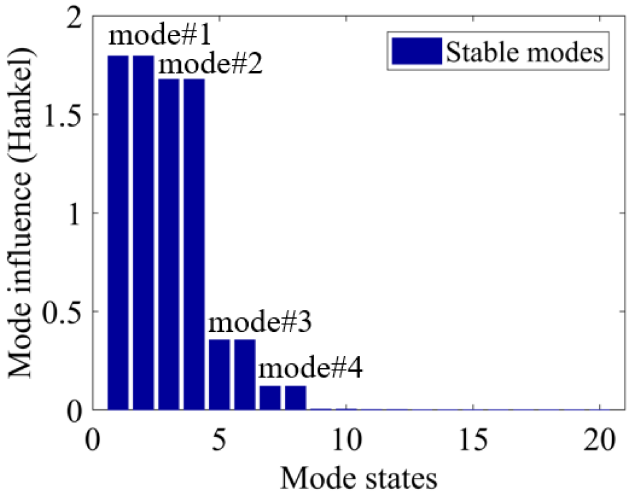

Figure 2.9: Hankel singular values of the FE model in the modal domain.

By the analysis of Fig. 2.9, it is possible to notice that the first four natural modes are the most important for representing the dynamic behavior of the rotating machine. Even though, for being more conservative, the first twelve natural modes are considered. In this way, the number of modes considered for the modal domain reduction is $N_{mod} = 12$. Then, the dynamic matrices of the system in the state space representation are reduced from $288x288$ to $24x24$.

The method applied to converting the system from time domain to modal domain is the so-called Pseudo-Modal Method and can be found in the book wrote by Lallane and Ferraris (1997).

2.5 FE Model Updating

In this section, the objective is to explain how to update the FE model so that the dynamic behavior of the test rig can be adequately represented.

In this way, one defines a frequency range and adjusts the numerical model accordingly. Then, it is expected that the numerical model behaves similarly to the test rig for the adopted frequency range. The model adjustment is performed for both frequency and time domains. Frequency Response Functions (FRFs) are determined for the frequency domain, while time plots and orbits of the rotating machine are obtained for the time domain identification.

2.5.1 Frequency Domain Model Updating

A heuristic optimization code based on Differential Evolution, Storn and Price (1995) was used for determining the optimal parameters that fit the experimental frequency domain curves. This method was chosen due to its fast convergence, simplicity, and good performance for solving inverse problems, besides its capacity to avoid local minima Cavalini-Jr (2013).

The minimization problem was formed by 90 individuals that compose the initial population (10 individuals for each parameter to be optimized). Other parameters used were the following: $F_{DE} = 0.8$, which concerns the difference amplification among the individuals and $CR_{DE} = 0.5$, related to the mutation ratio, as recommended by Viana et al. (2007).

Excitation was applied to both disc 1 and disc 2 on the vertical and horizontal directions by using a PCB® hammer, model $086C01$. The responses were measured at the positions S_{12} and S_{29}, also along the vertical and horizontal directions, by using the proximity probes SKF® model $CMSS65$. Finally, a total of eight FRFs were measured on the experimental test rig for the rotor at rest. The corresponding data was used to feed the optimization code. For collecting all the FRFs, a dynamic analyzer (Agilent®, model $35670A$), in a range of 0 to $250Hz$, and steps of $0.25Hz$ were considered. Table 2.1 summarizes the results from all the collected FRFs.

Table 2.1: Direction and name of each FRF collected.

Excitation Direction	Response Direction	FRF Name
D_1 vertical	S_{12} vertical	FRF #1
D_2 vertical	S_{12} vertical	FRF #2
D_1 horizontal	S_{12} horizontal	FRF #3
D_2 horizontal	S_{12} horizontal	FRF #4
D_1 vertical	S_{29} vertical	FRF #5
D_2 vertical	S_{29} vertical	FRF #6
D_1 horizontal	S_{29} horizontal	FRF #7
D_2 horizontal	S_{29} horizontal	FRF #8

Nine parameters were optimized, namely the stiffness on vertical and horizontal di-

rections of the first and second bearing $K_{xx_{b1}}, K_{zz_{b1}}, K_{xx_{b2}}$, and $K_{zz_{b2}}$; the modal damping factors of the first four natural modes ξ_1, ξ_2, ξ_3 and ξ_4 and the torsional stiffness due to the coupling between the shaft and the electric motor $K_{t_{coup}}$. In this case, $K_{t_{coup}}$ was added around the orthogonal directions X and Z of the nodes #1 and #2. Table 2.2 presents all the nine parameters to be optimized as well as their upper and lower bounds.

Table 2.2: Design space of the optimization problem: k [N/m], ξ [dimensionless] and $k_{t_{coup}}$ [Nm/rad]

	Variables	Design Space	
		Upper Bound	Lower Bound
Bearing 1	$k_{xx_{b1}}$	$9x10^9$	$5x10^7$
	$k_{zz_{b1}}$	$9x10^8$	$1x10^6$
Bearing 2	$k_{xx_{b2}}$	$9x10^9$	$1x10^7$
	$k_{zz_{b2}}$	$9x10^8$	$1x10^6$
Modal Damping	ξ_1	$2x10^{-1}$	$1x10^{-3}$
	ξ_2	$2x10^{-1}$	$1x10^{-3}$
	ξ_3	$1x10^{-1}$	$1x10^{-3}$
	ξ_4	$1x10^{-1}$	$1x10^{-3}$
Torsional Stiffness	$k_{t_{coup}}$	$1x10^4$	$1x10^3$

The optimization runs were performed ten times in order to guarantee that the minimum reached was not a local one. Each time the optimization process was re-initialized, a different population was generated, which mathematically means that the problem was solved through different points along the design space. Then, the solution presenting the smallest fitness function value was the one corresponding to the closest position to the global minimum. Table 2.3 presents the results of the mentioned ten optimization processes and the values of their corresponding fitness functions.

Table 2.3: Outputs of all the optimization processes: k [N/m], ξ [dimensionless] and $k_{t_{coup}}$ [Nm/rad].

Process	1	2	3	4	5	6	7	**8**	9	10
Fitness	2.697	2.587	2.968	2.436	2.874	**2.458**	2.523	2.352	2.569	2.841
$k_{xx_{b1}}$	$4.652x10^9$	$4.859x10^9$	$3.785x10^9$	$3.489x10^9$	$2.105x10^9$	$\mathbf{3.857x10^9}$	$2.965x10^9$	$2.699x10^9$	$1.754x10^9$	$6.857x10^9$
$k_{zz_{b1}}$	$7.587x10^7$	$8.652x10^7$	$9.428x10^7$	$8.658x10^7$	$6.358x10^7$	$\mathbf{8.657x10^7}$	$8.698x10^7$	$9.541x10^7$	$6.589x10^7$	$8.659x10^7$
$k_{xx_{b2}}$	$2.369x10^9$	$4.658x10^9$	$3.059x10^9$	$4.698x10^9$	$2.369x10^9$	$\mathbf{3.547x10^9}$	$2.698x10^9$	$3.979x10^9$	$4.698x10^9$	$2.369x10^9$
$k_{zz_{b2}}$	$5.369x10^7$	$8.698x10^7$	$6.987x10^7$	$8.058x10^7$	$7.968x10^7$	$\mathbf{7.987x10^7}$	$8.064x10^7$	$8.935x10^7$	$9.687x10^7$	$9.605x10^7$
ξ_1	0.269	0.223	0.099	0.112	0.258	**0.098**	0.122	0.130	0.096	0.127
ξ_2	0.092	0.086	0.103	0.155	0.087	**0.101**	0.077	0.105	0.198	0.081
ξ_3	0.055	0.068	0.052	00.064	0.051	**0.063**	0.047	0.060	0.069	0.049
ξ_4	0.057	0.099	0.077	0.085	0.068	**0.073**	0.088	0.075	0.058	0.087
$k_{t_{coup}}$	2589	3058	3368	3987	3589	**3638**	3554	3377	4098	3238

The global minimum corresponds to the one presented in column 6 of Tab. 2.3. It means this is the best possible solution determined by the optimizer. In the following, one presents the results of the frequency domain model updating. The experimental test rig FRFs and the ones derived from the FE model, considering the chosen optimized parameters are compared.

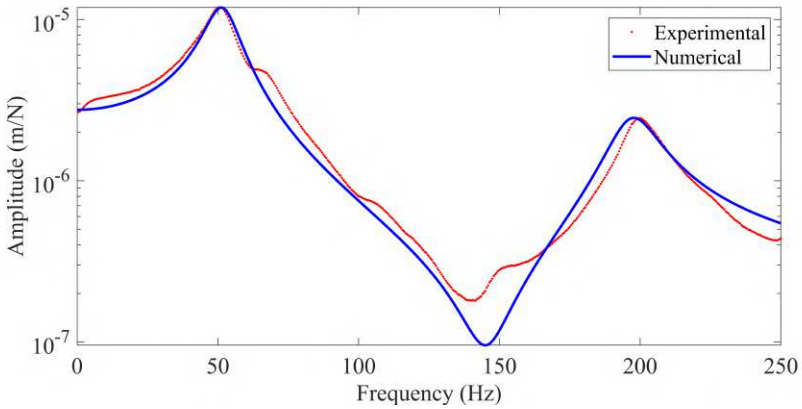

Figure 2.10: FRF#1

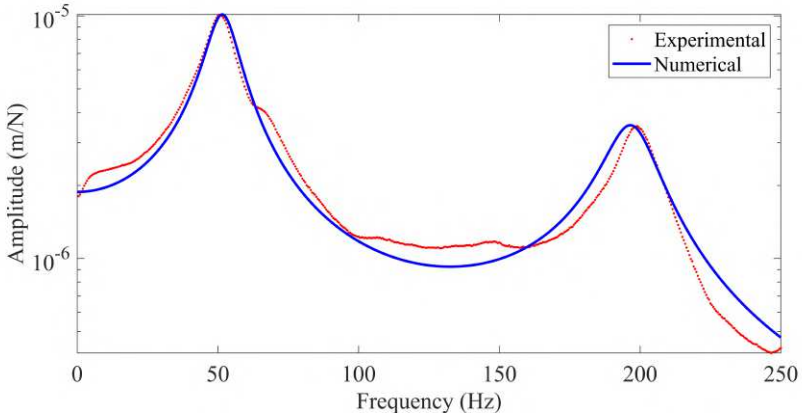

Figure 2.11: FRF#2

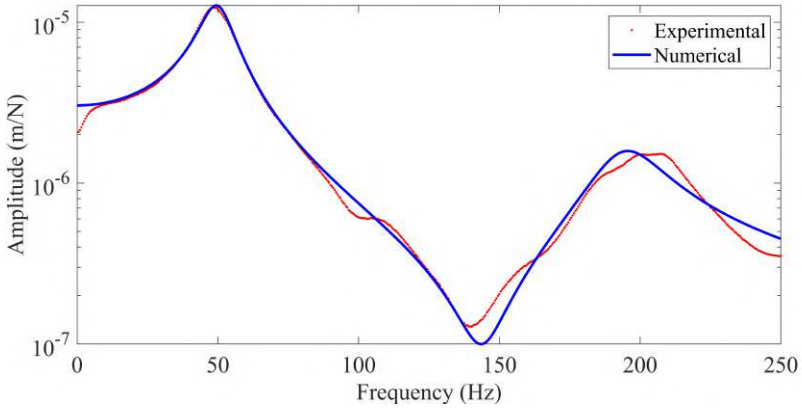

Figure 2.12: FRF#3

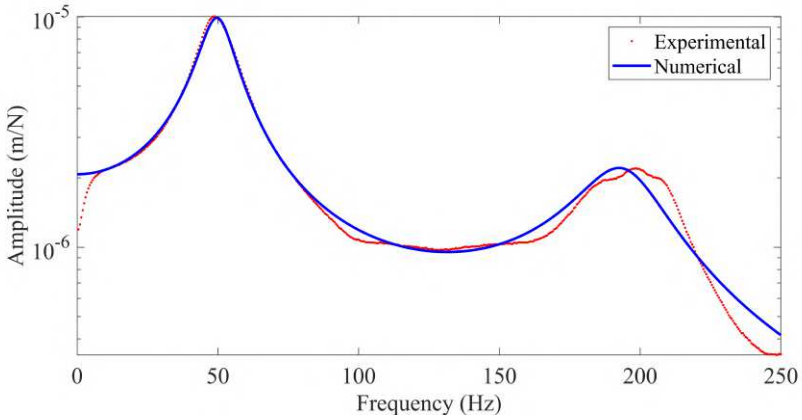

Figure 2.13: FRF#4

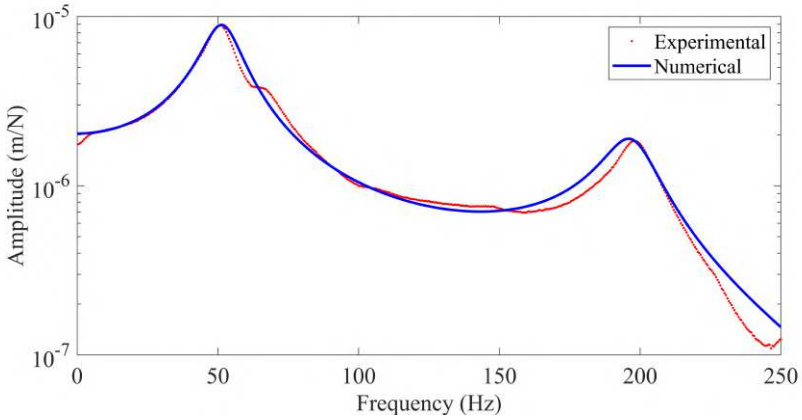

Figure 2.14: FRF#5

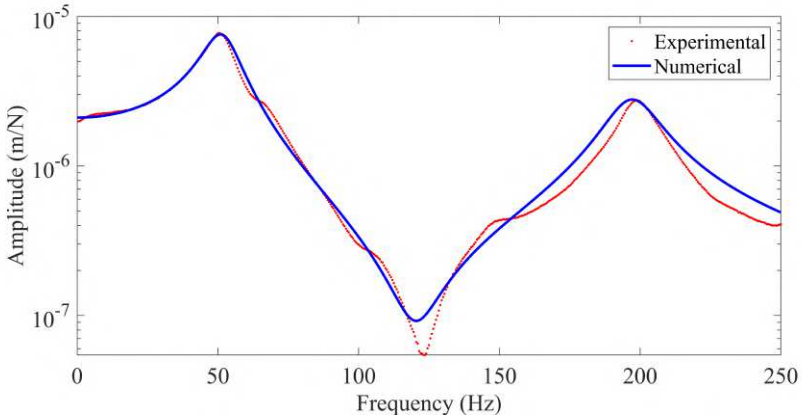

Figure 2.15: FRF$\#6$

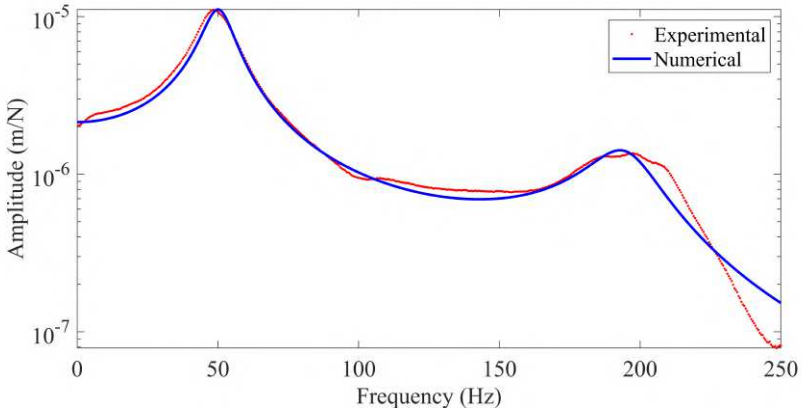

Figure 2.16: FRF$\#7$

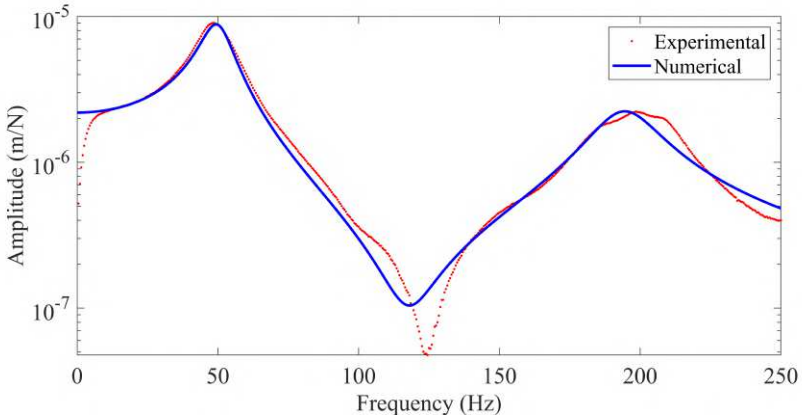

Figure 2.17: FRF$\#8$

One may note that the experimental and numerical curves are well fitted, which validates the numerical model in the frequency domain, in the range from 0 - $250Hz$.

As previously mentioned, the numerical and experimental FRFs correspond to the rotor response at rest. This procedure is acceptable because the gyroscopic effect associated with the rotor first two modes is small, i.e., for rotation speeds below 3450 rev/min (57.50 Hz). Figure 2.18 presents the Campbell Diagram, collected from the numerical model, which was now validated.

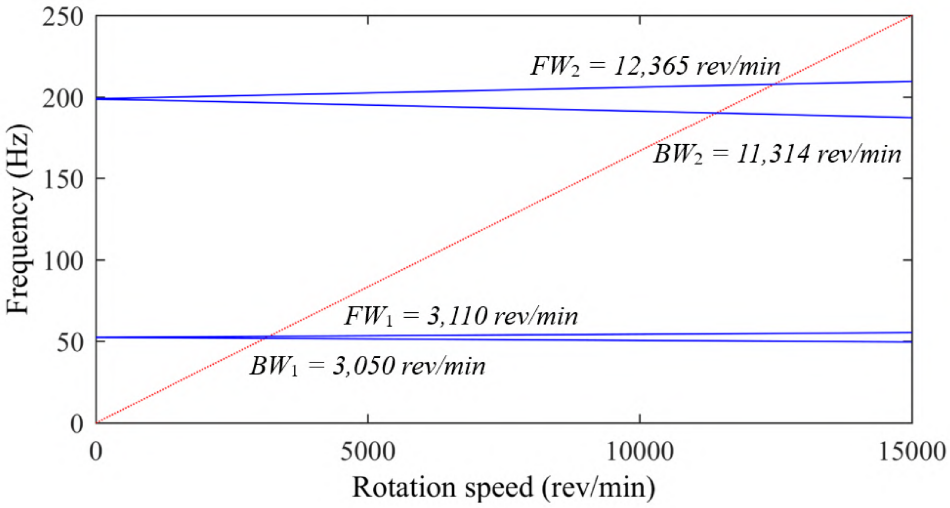

Figure 2.18: Campbell Diagram.

One may notice from the Campbell Diagram of the validated numerical model that the first four critical speeds of the rotor are found as $3,050rev/min$ ($50.83Hz$); $3,110rev/min$ ($51.83Hz$); $11,314rev/min$ ($188.57Hz$) and $12,365rev/min$ ($206.08Hz$).

The shapes of the first four vibration modes, shown in the Campbell Diagram are depicted in Fig. 2.19.

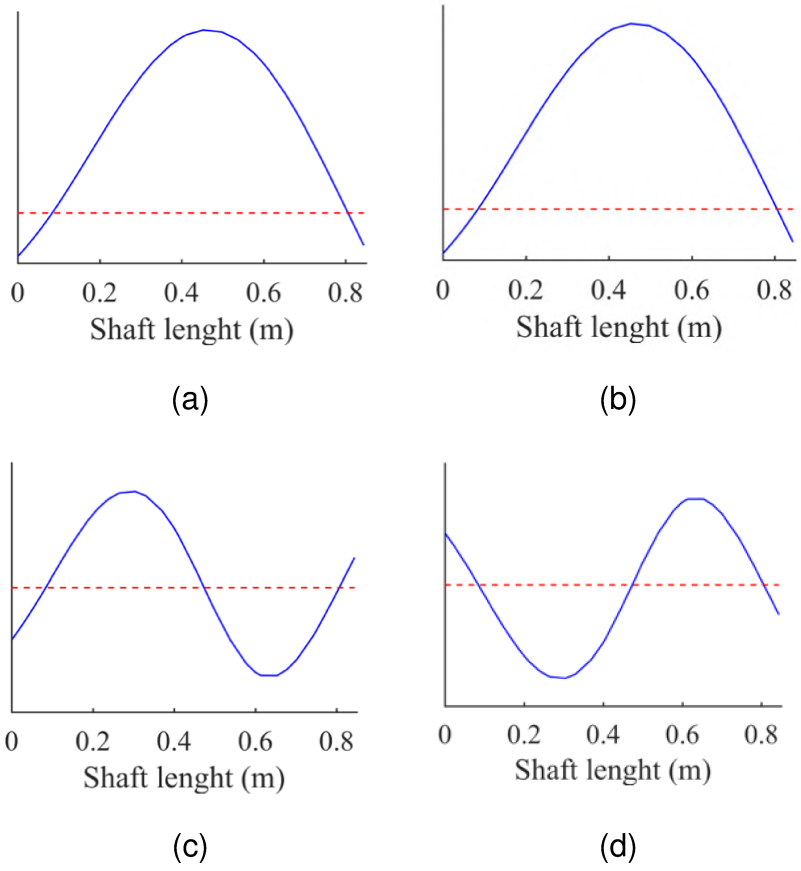

Figure 2.19: First four natural modes: (a) first; (b) second; (c) third; (d) fourth.

2.5.2 Time Domain Updating

Besides validating the model in the frequency domain, it is also important to guarantee that the time domain responses are well fitted to the experimental responses of the test rig. The time-domain responses measured on the experimental test rig and those derived from the numerical model are compared in figure 2.20. This result was obtained for the shaft operating at $900rev/min$, with an unbalance of $1.276x10^{-3}Kgm$.

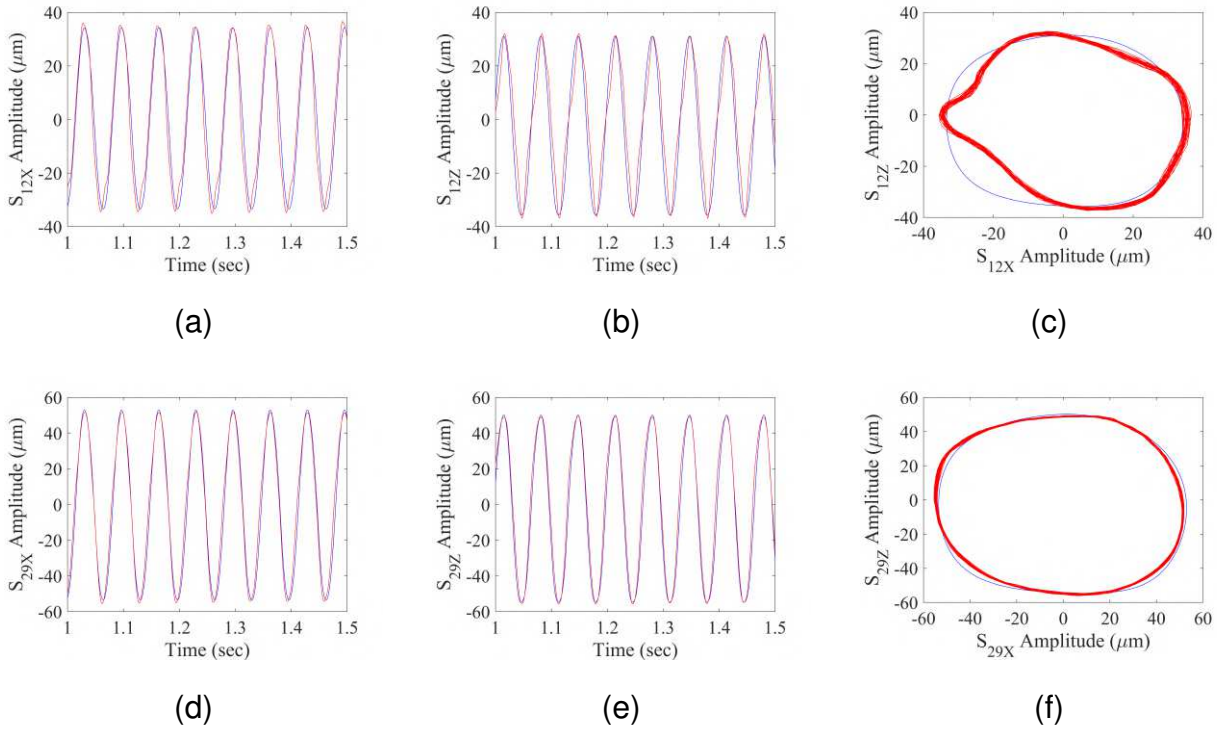

Figure 2.20: Results of model updating for lateral vibrations in time domain: (—) Experimental; (—) Numerical: (a) S_{12_x}; (b) S_{12_z}; (c) orbit S_{12_x} Vs. S_{12_z}; (d) S_{29_x}; (e) S_{29_z}; (f) orbit S_{29_x} Vs. S_{29_z};

For adjusting the time domain responses, two experimental procedures were necessary. The first experimental test comparing *Stress Vs. Strain* was performed for a sample of the same material and the same diameter of the shaft that is used in the experimental test rig. This was done for obtaining the Young's Modulus (E) of the material, which was found to be $1.8806x10^{11}Pa$. In the second experimental test, the dimensions of the shaft were measured and its volume was calculated. Then, the shaft mass was measured. Finally, the density (ρ) of the material was calculated and found to be $7.509x10^{3}kg/m^{3}$.

Having determined the above-mentioned parameters, together with the optimized variables that were presented in the previous section, the numerical model exhibits a good agreement with respect to the experimental test rig, both in time and frequency domains.

Chapter 3

Fault Detection in Rotating Machinery by Using the Modal State Observer Approach

3.1 Introduction

In the last chapter, a FE model for crack detection was developed and updated with respect to the dynamic responses obtained from the test rig in both time and frequency domains. Now, it is time to test some model-based crack detection techniques for checking if all that effort is effective. In this way, the present chapter introduces a fault detection methodology based on the so-called modal state observer (MSO) for detecting transverse cracks along a horizontal rotating shaft. The rotating machine used for applying this technique is the one presented in the previous chapter, containing a flexible horizontal shaft, two rigid discs, two self-aligning ball bearings, and four proximity probes for measuring shaft lateral vibrations along two directions at two different nodes.

This study is important due to the fact that the existence of transverse cracks in rotating shafts may lead to failures, which imply economic losses and security issues. For this reason, in the last decades, attention has been devoted to this subject promoting the development of several vibration-based structural health monitoring (SHM) techniques. The MSO technique was chosen because it combines the advantages of both time and frequency domains for increasing crack detection performance. The

Luenberger state observer is formulated in the modal domain to estimate the rotor vibration responses described in modal coordinates. Consequently, the most affected vibration modes due to the crack existence can be determined.

Numerical and experimental investigations are presented in this chapter, aiming at highlighting the efficiency of the MSO technique. The monitoring is based on the kernel density function estimate, which is able to deal with the probability density estimation of a given data sample. This technique is similar to histograms, however leading to better results.

Both open and breathing crack behaviors are considered. The breathing behavior of the crack is simulated according to the Mayes model, and the additional flexibility introduced in the shaft by the crack is determined by using the linear fracture mechanics theory.

Numerical and experimental results obtained demonstrate that the methodology conveyed represents a good alternative technique to detect faults in rotating machines.

3.2 State Space Representation of the System

The MSO technique is applied to both the test rig and the FE model presented in Chap.2. The eqauation of motion of the cracked rotor will be presented in section 3.5, by Eq.3.6. For applying the present crack detection method, the equation of motion is rewritten in the state space form, as described by Eq.3.1.

$$\begin{aligned} \dot{\mathbf{x}} &= \mathbf{A}\mathbf{x} + \mathbf{B}\mathbf{u} \\ \mathbf{y} &= \mathbf{C}\mathbf{x} \end{aligned} \tag{3.1}$$

where **A** represents the dynamic matrix, **B** the input matrix,and **C** the output matrix. It is worth mentioning that the matrix **D** was not represented, since it is a null matrix for this system.

For the interested reader, more details about state space representation can be found in Franklin et al. (2014).

3.3 Luenberger State Observer

Luenberger (1964) introduced the concept of state observers. A state observer is a

virtual system, which is linear and time-invariant, possesses arbitrary eigenvalues and is fed by the inputs and outputs of the physical system, Simon and Mitter (1968). Figure 3.1 presents a real system with the state vector represented by $\mathbf{x}(t)$ and a state observer whose state vector is given by $\mathbf{z}(t)$. The observer output vector, $\hat{\mathbf{y}}(t)$, converges to the real system output vector $\mathbf{y}(t)$, through the correct tuning of the observer gain matrix, **L**. In this case, $\mathbf{u}(t)$ stands for the input vector applied to both the real system and the corresponding state observer.

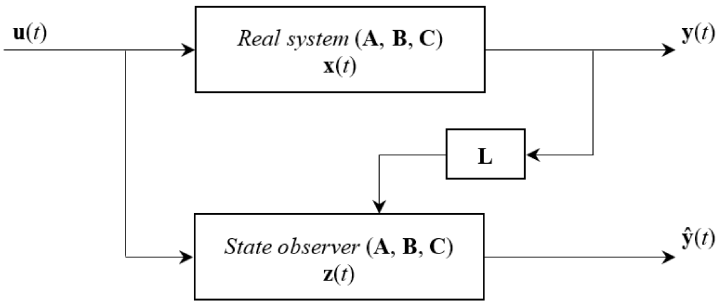

Figure 3.1: Luenberger state observer.

The mathematical definition of the Luenberger state observer, Luenberger (1964), is given by:

$$\begin{aligned} \dot{\mathbf{z}}(t) &= (\mathbf{A} - \mathbf{LC})\mathbf{z}(t) + \mathbf{Bu}(t) + \mathbf{Ly}(t) \\ \hat{\mathbf{y}}(t) &= \mathbf{Cz}(t) \end{aligned} \tag{3.2}$$

where **A-LC** represents the so-called observer matrix.

There are several methods dedicated to the calculation of the gain matrix **L**, in which the Linear Quadratic Regulator and the Kalman filter are among the most widely used approaches, Simon and Mitter (1968). In the present work, the Kalman filter method is applied to determine the observer gain, since it represents a quite simple procedure. It can be done, basically by using the command *lqe*, in MatLab®.

3.4 Modal State Observer

The MSO was proposed by Cavalini-Jr et al. (2008), in which faults were detected in a truss structure. First, the representative model of the healthy mechanical system described in modal coordinates has to be identified. The system model (matrices $\mathbf{A}$, $\mathbf{B}$, and $\mathbf{C}$ in Fig.3.1) are represented in the block-diagonal state space form, as suggested

by Skogestad and Postlethwaite (1996). In the present work, the MatLab® command *canon* was used to obtain the matrices $\mathbf{A}$, $\mathbf{B}$, and $\mathbf{C}$ in the modal block-diagonal state space form (matrices $\mathbf{A_m}$, $\mathbf{B_m}$, and $\mathbf{C_m}$, respectively). The advantages of time and modal domains are combined by inputting time-domain data measured by 1, 2, ... or N sensors available into the MSO. The measured vibration responses are used by the MSO to determine temporal displacement and velocity vectors associated with the first, second, third, ..., nth vibration mode considered in the modal model of the system.

Figure 3.2 shows an example where 2 sensors (N = 2; sensors $y_1(t)$ and $y_2(t)$) are used to measure the vibration responses of a rotating machine. Four vibration modes are considered in the rotor modal model ($n = 4$). Consequently, $\mathbf{A_m}$ is a $8x8$ matrix and $\mathbf{C_m}$ is a $2x8$ matrix; the number 8 stands for the four modal displacements and four modal velocities estimated by the MSO (see the vector $z_m(t)$ in Fig.3.2). The matrix $\mathbf{B_m}$ $(8x2)$ is not used in this application since the vibration responses $y_1(t)$ and $y_2(t)$ are enough to obtain a satisfactory estimation. Thus, MSO is able to estimate the temporal displacement associated with the first vibration mode $z_{m1}(t)$,the temporal velocity associated with the first vibration mode $\dot{z}_{m1}(t)$, the temporal displacement associated with the second vibration mode $z_{m2}(t)$, the temporal velocity associated with the second vibration mode $\dot{z}_{m2}(t)$, and so on, until the fourth mode, by following this sequence. The time length of the estimated temporal modal vector is the same of the time domain vibration responses measured on the rotating machine. The estimated vibration responses $\hat{\mathbf{y}}_\mathbf{1}(t)$ and $\hat{\mathbf{y}}_\mathbf{2}(t)$ are compared with $\mathbf{y_1}(t)$ and $\mathbf{y_2}(t)$, respectively, to evaluate if the MSO is working properly.

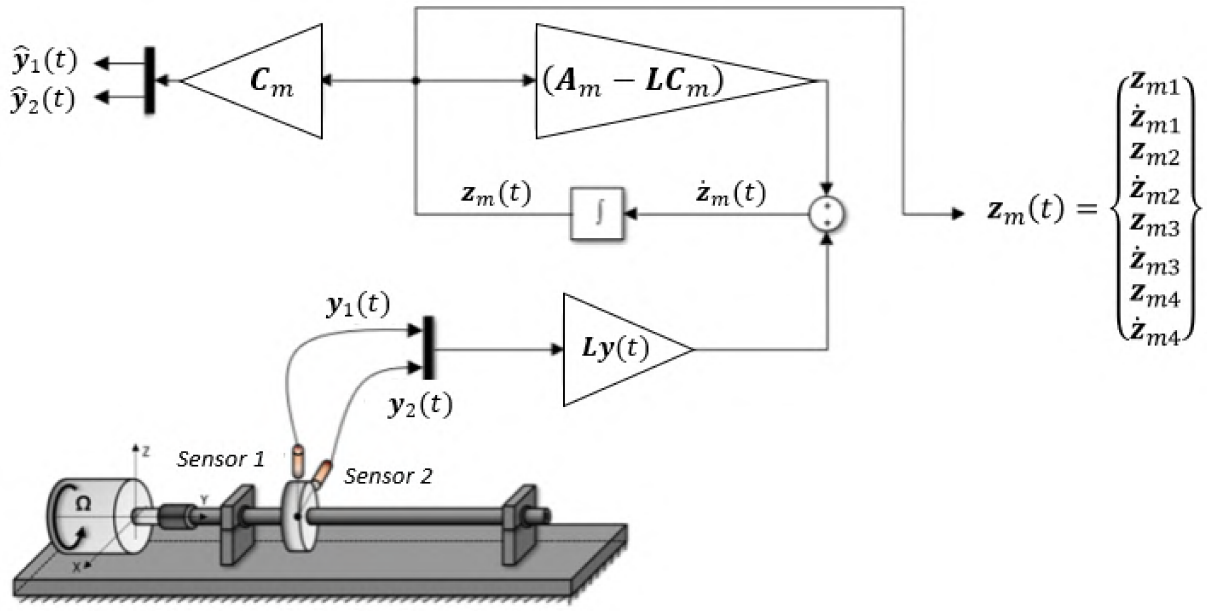

Figure 3.2: MSO representation.

Figure 3.3 shows the scheme of the SHM technique based on MSO. The system condition is continuously monitored by the MSO from the measured vibration responses, which are represented by the vector $\mathbf{y_u}(t)$ in Fig.3.3. The vector $\mathbf{y_h}(t)$ represents the vibration responses in the time domain of the healthy system. Any deviation between the obtained modal state vector $\mathbf{z_{mu}}(t)$ and the reference $\mathbf{z_{mh}}(t)$ (i.e., the modal state vector of the healthy system) is interpreted as fault existence. Then, a damage index is defined. MSO estimates the modal state vectors from the measured vibration responses in the time domain. Thus, the most affected vibration mode, due to the fault existence can be indicated.

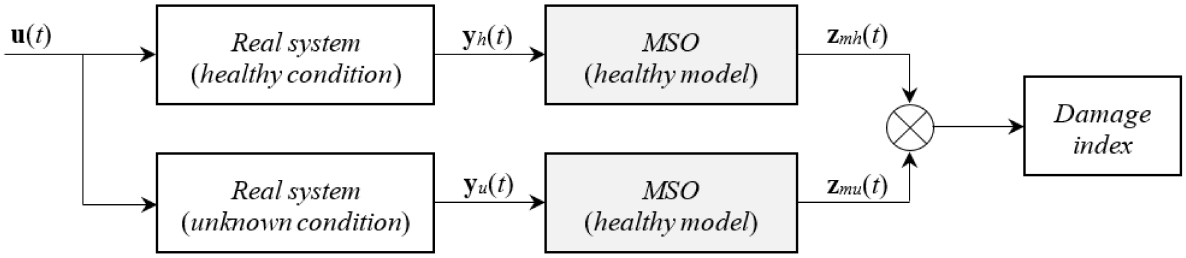

Figure 3.3: SHM technique based on MSO.

In the present chapter, the so-called kernel density estimator is applied to $\mathbf{z_{mh}}(t)$ and $\mathbf{z_{mu}}(t)$ aiming at quantifying the influence of a given fault on the estimated modal vibration responses of the monitored system. Thus, let $\mathbf{X} = [x_1, x_2, \ldots, x_n]$ be an

independent and identically distributed sampled data drawn from a distribution with an unknown density function. The shape of this function can be estimated by its kernel density estimator, Samadani et al. (2015) as defined by Eq.(3.3).

$$f = \frac{1}{nh}\sum_{i=1}^{n} K_e\left(\frac{x - x_i}{h}\right) \tag{3.3}$$

where f is the estimated density function, $h \geq 0$ is a smoothing parameter calling bandwidth and Ke is the kernel function which satisfies the following requirements:

$$\begin{gathered}\int_{-\infty}^{+\infty} K_e(s)ds = 1 \\ K_e(-s) = K_e(s) \quad \forall s\end{gathered} \tag{3.4}$$

Thus, the damage index E presented in Fig.3.3 is calculated according to Eq.(3.5).

$$E = \frac{\|f_{mu} - f_{mh}\|}{\|f_{mh}\|}100\% \tag{3.5}$$

where f_{mh} and f_{mu} are the estimated density functions associated with $\mathbf{z_{mh}}(t)$ and $\mathbf{z_{mu}}(t)$, respectively.

The MSO is based on the association of the Luenberger state observer with features derived from the modal domain. Equation 3.2 is equally valid for MSO, being necessary only the state space matrices to be described in the modal domain. In this case, the MSO estimates the modal states related to the points where, for instance, the vibration responses of the shaft in the time domain were measured, Cavalini-Jr et al. (2008). Consequently, it is expected more sensitive modal vibration responses with respect to fault existence stemming from the application of the MSO technique.

3.5 Crack Modeling

For the crack detection method to be presented in this chapter, a crack is generated on the FE model of the test rig presented on Chap.2. This changes Eq.2.1 by the addition of a term which represents the force derived from the crack existence. The new equation, considering the crack presence is given by Eq.3.6:

$$\mathbf{M}\ddot{\mathbf{q}} + [\mathbf{D} + \Omega\mathbf{D}_g]\,\dot{\mathbf{q}} + \mathbf{K}\mathbf{q} = \mathbf{W} + \mathbf{F}_u + \Delta\mathbf{K}\mathbf{q} \tag{3.6}$$

where $\Delta\mathbf{Kq}$ stands for the crack force, which is considered to be concentrated only at the cracked element. All the other terms where previously presented in Chap.2.

For modeling the breathing behavior of transversal cracks, two of the most widely used methods are the so-called Gasch's, Gasch (1976) and Mayes', Mayes and Davis (1976) models. The model used in this study for simulating crack behavior is the one proposed by Mayes, since it gives a more realistic crack behavior. However, before entering in the details of this model, it is necessary to consider some background information.

Basically, there are two types of cracks. The open and the breathing ones. Open cracks are kept open during a shaft revolution and are usually artificially produced. Real cracks are fatigue generated and present a breathing behavior when static loads are higher than dynamic loads (weight dominance condition). This can be observed especially for heavy horizontal rotors with low unbalance values. Breathing crack behavior produces one opening and one closure of the crack for each revolution of the shaft. When the crack is facing down, it tends to open due to static loads; on the other hand, when it is facing up, it tends to close. This behavior represents a dangerous condition for the rotating machine since it favors crack propagation.

Both Mayes and Gasch methods do not consider stress nor strain distributions. These methods do not correlate stiffness losses as a function of the crack depth. This way, additional theories are needed for calculating the extra flexibility imposed by the crack. In this study, linear fracture mechanics theory is applied to fulfill this gap. According to Cavalini-Jr (2013), some cases are not covered by this theory, such as very deep cracks (much greater than half of the diameter), multiple cracks into a single cross-section, not flat cracked cross-section and friction in the cracked area. Nevertheless, in the present work, none of these conditions occur and, according to Morais (2010), linear fracture mechanics theory furnishes results accurate enough to be used in rotating machines.

3.5.1 Additional flexibility due to the crack

The presence of a crack along a shaft produces a local decrease of the stiffness (or an increase of the flexibility). Figure 3.4 presents a finite element with a central transverse crack, of depth α.

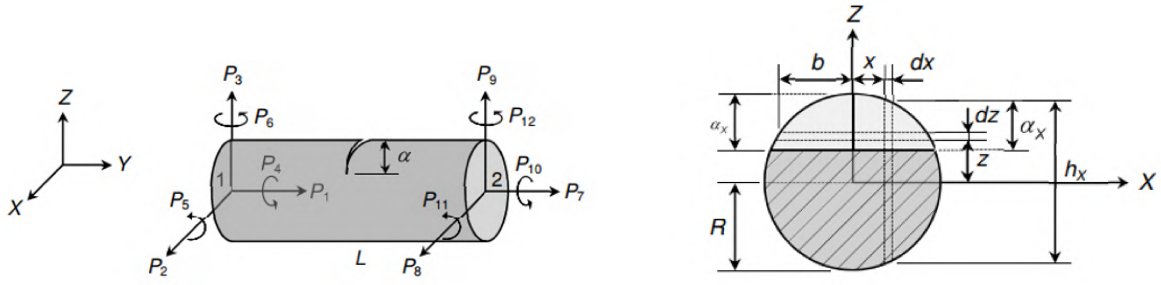

(a) (b)

Figure 3.4: Finite element with a transverse crack. (a) Applied efforts; (b) Cross section.

This element receives axial forces ($P1$ and $P7$), shear forces ($P2, P3, P8$ and $P9$), torsion moments ($P4$ and $P10$) and bending moments($P5$, $P6$, $P11$ and $P12$). Figure 3.4(b) presents the cracked cross section with a crack depth α_x. The hatched area represents the healthy part of the shaft.

According to Cavalini-Jr (2013), the additional flexibility imposed by the crack is calculated by:

$$c_{ij} = \frac{\partial^2 U_c}{\partial P_i \partial P_j} \tag{3.7}$$

where U_c stands for the additional strain energy, due to the crack.

This way,the matrix containing dimensionless additional flexibility terms can be written as:

$$\bar{\mathbf{c}}_c = \begin{bmatrix} \bar{c}_{11} & 0 & 0 & 0 & \bar{c}_{15} & \bar{c}_{16} \\ & \bar{c}_{22} & 0 & \bar{c}_{24} & 0 & 0 \\ & & \bar{c}_{33} & \bar{c}_{34} & 0 & 0 \\ & & & \bar{c}_{44} & 0 & 0 \\ & SIM. & & & \bar{c}_{55} & \bar{c}_{56} \\ & & & & & \bar{c}_{66} \end{bmatrix} \tag{3.8}$$

The matrix coefficients are shown below:

$$
\begin{aligned}
&[l]\bar{c}_{11} = \tfrac{ER}{1-\mu^2}c_{11} = \tfrac{2}{\pi}\int_0^{\bar{\alpha}_x}\int_{-\bar{b}}^{\bar{b}} \bar{x}F_1^2\tfrac{\bar{z}}{\bar{h}_x}d\bar{x}d\bar{z} \\
&\bar{c}_{15} = \tfrac{ER^2}{1-\mu^2}c_{15} = \tfrac{8}{\pi}\int_0^{\bar{\alpha}_x}\int_{-\bar{b}}^{\bar{b}} \bar{z}\sqrt{(1-\bar{x}^2)}F_1\tfrac{\bar{z}}{\bar{h}_x}F_2\tfrac{\bar{z}}{\bar{h}_x}d\bar{x}d\bar{z} \\
&\bar{c}_{16} = \tfrac{ER^2}{1-\mu^2}c_{16} = \tfrac{4}{\pi}\int_0^{\bar{\alpha}_x}\int_{-\bar{b}}^{\bar{b}} \bar{x}\bar{z}F_1^2\tfrac{\bar{z}}{\bar{h}_x}d\bar{x}d\bar{z} \\
&\bar{c}_{22} = \tfrac{ER}{1-\mu^2}c_{22} = \tfrac{2}{\pi}\int_0^{\bar{\alpha}_x}\int_{-\bar{b}}^{\bar{b}} \bar{z}F_{III}^2\tfrac{\bar{z}}{\bar{h}_x}d\bar{x}d\bar{z} \\
&\bar{c}_{24} = \tfrac{ER^2}{1-\mu^2}c_{24} = \tfrac{4}{\pi}\int_0^{\bar{\alpha}_x}\int_{-\bar{b}}^{\bar{b}} \sqrt{(1-\bar{x}^2)}\bar{z}F_{III}^2\tfrac{\bar{z}}{\bar{h}_x}d\bar{x}d\bar{z} \\
&\bar{c}_{33} = \tfrac{ER}{1-\mu^2}c_{33} = \tfrac{2}{\pi}\int_0^{\bar{\alpha}_x}\int_{-\bar{b}}^{\bar{b}} \bar{z}F_{II}^2\tfrac{\bar{z}}{\bar{h}_x}d\bar{x}d\bar{z} \\
&\bar{c}_{34} = \tfrac{ER^2}{1-\mu^2}c_{34} = \tfrac{4}{\pi}\int_0^{\bar{\alpha}_x}\int_{-\bar{b}}^{\bar{b}} \bar{x}\bar{z}F_{II}^2\tfrac{\bar{z}}{\bar{h}_x}d\bar{x}d\bar{z} \\
&\bar{c}_{44} = \tfrac{ER^3}{1-\mu^2}c_{44} = \tfrac{8}{\pi}\int_0^{\bar{\alpha}_x}\int_{-\bar{b}}^{\bar{b}} \bar{x}^2\bar{z}F_{II}^2\tfrac{\bar{z}}{\bar{h}_x} + (1+\nu)(1-\bar{x}^2)\bar{z}F_{III}^2\tfrac{\bar{z}}{\bar{h}_x}d\bar{x}d\bar{z} \\
&\bar{c}_{55} = \tfrac{ER^3}{1-\mu^2}c_{55} = \tfrac{32}{\pi}\int_0^{\bar{\alpha}_x}\int_{-\bar{b}}^{\bar{b}} \bar{z}(1-\bar{x}^2)F_2^2\tfrac{\bar{z}}{\bar{h}_x}d\bar{x}d\bar{z} \\
&\bar{c}_{56} = \tfrac{ER^3}{1-\mu^2}c_{56} = \tfrac{32}{\pi}\int_0^{\bar{\alpha}_x}\int_{-\bar{b}}^{\bar{b}} \bar{x}\bar{z}\sqrt{(1-\bar{x}^2)}F_1\tfrac{\bar{z}}{\bar{h}_x}F_2\tfrac{\bar{z}}{\bar{h}_x}d\bar{x}d\bar{z} \\
&\bar{c}_{66} = \tfrac{ER^3}{1-\mu^2}c_{66} = \tfrac{16}{\pi}\int_0^{\bar{\alpha}_x}\int_{-\bar{b}}^{\bar{b}} \bar{x}^2\bar{z}F_1^2\tfrac{\bar{z}}{\bar{h}_x}d\bar{x}d\bar{z}
\end{aligned}
\tag{3.9}
$$

where $\bar{x} = \frac{x}{R}$, $\bar{z} = \frac{z}{R}$, $\bar{h_x} = \frac{h_x}{R}$, $\bar{b} = \frac{b}{R}$ and $\bar{\alpha_x} = \frac{\alpha_x}{R}$.

The integral limits in Eq. 3.9 are described in Papadopoulos (2004). The crack has the limits $-b$ and b in the X direction, while having limits 0 and α_x in the Z direction, according to Fig.3.4(b). Geometrically, b can be defined as:

$$b = \sqrt{R^2 - (R-\alpha)^2} \tag{3.10}$$

Also, *b* can be written as it can be shown on its dimensionless form:

$$\bar{b} = \sqrt{1 - (1-\bar{\alpha})^2} \tag{3.11}$$

The height h_x can be defined by the following relation:

$$h_x = 2\sqrt{R^2 - x^2} \tag{3.12}$$

while its dimensionless form can be written as:

$$\bar{h}_x = 2\sqrt{1 - \bar{x}^2} \tag{3.13}$$

The crack superior limit in the Z direction, for each x value, can be calculated according to:

$$\alpha_x = \frac{h_x}{2} - (R - \alpha) = \sqrt{R^2 - x^2} - (R - \alpha) \tag{3.14}$$

Finally, this term in its dimensionless form can be written as:

$$\bar{\alpha}_x = \frac{\bar{h}_x}{2R} - (1 - \frac{\alpha}{R}) = \sqrt{1 - x^2} - (1 - \bar{\alpha}) \tag{3.15}$$

More details are not furnished in this dissertation. For the interested reader, more information can be found in Cavalini-Jr (2013); Papadopoulos (2004); Anderson (2005).

3.5.2 Mayes Model

The Mayes model, Mayes and Davis (1976), considers the crack transition from fully open to fully closed in a progressive way, being described by a cosine function. Also, this model is valid only when the weight dominance condition is satisfied. The use of a cosine function in this model represents a simplification since it converts the nonlinear equations of motion to linear equations with time-varying coefficients, Friswell et al. (2010).

Two coordinate frames are necessary to derive the equations of motion of the cracked shaft, namely OXZ and $O\eta\xi$, as presented in Fig.3.5. The former reference frame is fixed in space and the second one rotates according to the shaft position ($\theta = \Omega t$; where θ is the angular position of the shaft and t is the time).

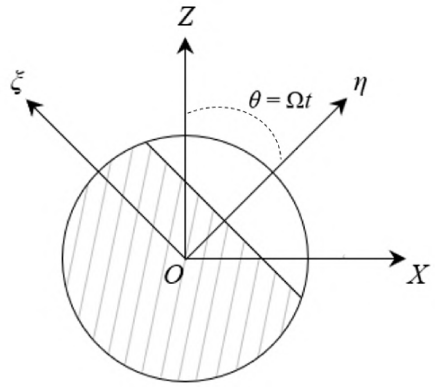

Figure 3.5: Shaft cross-section with a crack (η is assumed to be perpendicular to the crack edge).

According to the Mayes model, the stiffness of the cracked shaft along the η and ξ directions (Fig.3.5) can be defined as:

$$\begin{aligned} k_{\xi Mayes}(\theta) &= \tfrac{1}{2}\left(k_o + k_\xi\right) + \tfrac{1}{2}\left(k_o - k_\xi\right) C_1 \\ k_{\eta Mayes}(\theta) &= \tfrac{1}{2}\left(k_o + k_\eta\right) + \tfrac{1}{2}\left(k_o - k_\eta\right) C_1 \end{aligned} \tag{3.16}$$

where $k_{\eta Mayes}$ and $k_{\xi Mayes}$ are the angular dependent stiffnesses along the η and ξ directions, respectively, k_o represents the healthy stiffness of the shaft, k_η and k_ξ stands for shaft stiffness with a crack along η and ξ directions, respectively, and $C_1 = cos(\theta)$. If $\theta = 0^o$, the stiffness $k_{\xi Mayes}(0^o) = k_{\eta Mayes}(0^o) = k_o$. Thus, the crack remains fully closed. However, if $\theta = 180^o$, $k_{\xi Mayes}(180^o) = k_\xi$ and $k_{\eta Mayes}(180^o) = k_\eta$. In this case, the crack remains fully opened, Cavalini-Jr. et al. (2016).

Figure 3.6 represents the variation of the stiffness of the cracked shaft as a function of the angular position, according to Eq.3.16.

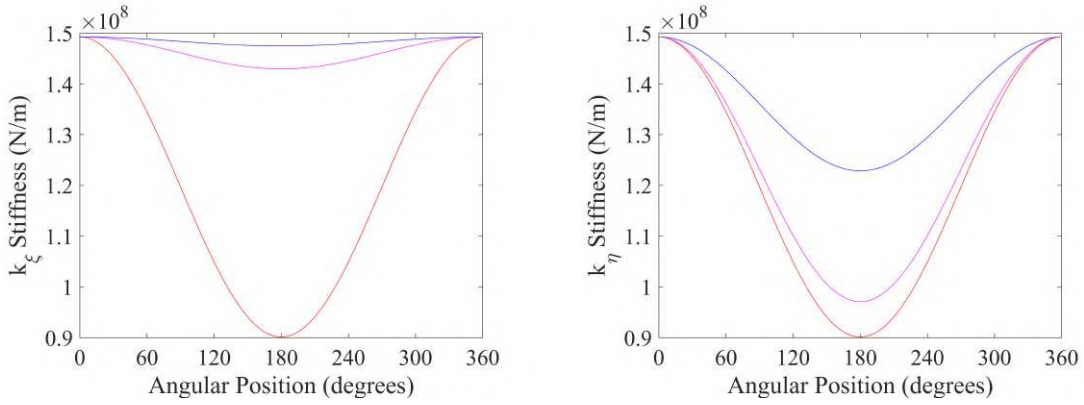

(a) (b)

Figure 3.6: Stiffness variations considering the rotating frames ξ and η, according to the Mayes model (—)$\frac{\alpha}{D} = 0.20$ (—)$\frac{\alpha}{D} = 0.35$ (—)$\frac{\alpha}{D} = 0.50$. a) $k_{\xi M}$; b) $k_{\eta M}$

In the matricial form, the stiffness of the cracked shaft in rotating coordinates ($\mathbf{k}_{RMayes}$) is given by:

$$\mathbf{k}_{RMayes} = \begin{bmatrix} k_{M\xi} + k_{D\xi}C_1 & 0 \\ 0 & k_{M\eta} + k_{D\eta}C_1 \end{bmatrix} \tag{3.17}$$

where $k_{M\xi} = (k_o + k_x i)/2$, $k_{M\eta} = (k_o + k_\eta)/2$, $k_{D\xi} = (k_o - k_x i)/2$, and $k_{D\eta} = (k_o - k_\eta)/2$.

The stiffness of the cracked shaft in fixed coordinates ($\mathbf{k}_{FMayes}$) is determined by using the following transformation:

$$\mathbf{k}_{FMayes} = \begin{bmatrix} C_1 & S_1 \\ -S_1 & C_1 \end{bmatrix}^T \mathbf{k}_{RMayes} \begin{bmatrix} C_1 & S_1 \\ -S_1 & C_1 \end{bmatrix} = \begin{bmatrix} k_{FMayes(11)} & k_{FMayes(12)} \\ k_{FMayes(21)} & k_{FMayes(22)} \end{bmatrix} \tag{3.18}$$

where $S_i = sin(i\theta)$ and $C_i = cos(i\theta)$, with $i = 1, 2, \ldots, n$. The terms of $\mathbf{k}_{FMayes}$ are presented in Eq.(3.19).

$$[l]k_{FMayes(11)} = \tfrac{1}{2}\left(k_{M\xi} - k_{M\eta}\right) + \tfrac{1}{4}\left(3k_{D\xi} - k_{D\eta}\right)C_1 + \tfrac{1}{4}\left(k_\xi - k_\eta\right)C_2 - \tfrac{1}{8}\left(k_\xi - k_\eta\right)C_3$$

$$k_{FMayes(12)} = \tfrac{1}{4}\left(k_{D\xi} - k_{D\eta}\right)S_1 + \tfrac{1}{2}\left(k_{M\xi} - k_{M\eta}\right)S_2 + \tfrac{1}{4}\left(k_{D\xi} - k_{D\eta}\right)S_3$$

$$k_{FMayes(22)} = \tfrac{1}{2}\left(k_{M\xi} + k_{M\eta}\right) + \tfrac{1}{4}\left(k_{D\xi} - 3k_{D\eta}\right)C_1 - \tfrac{1}{4}\left(k_\xi - k_\eta\right)C_2 - \tfrac{1}{8}\left(k_\xi - k_\eta\right)C_3 \tag{3.19}$$

Figure 3.7 presents the stiffness variations of a cracked shaft element, according to the vertical and horizontal fixed frame directions.

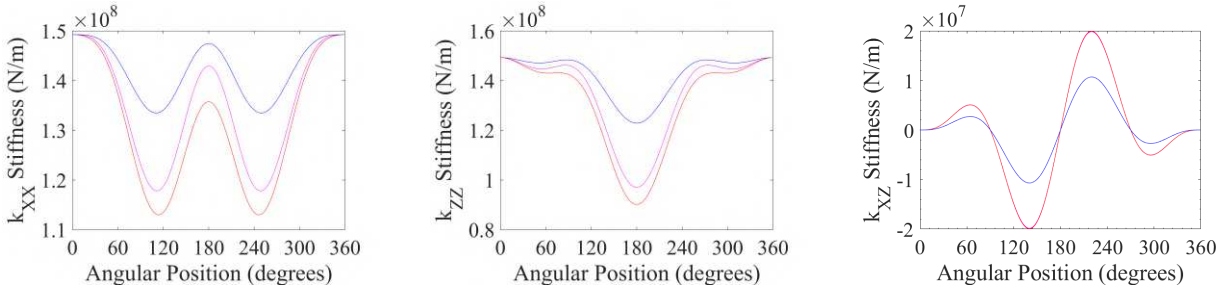

(a) (b) (c)

Figure 3.7: Stiffness behaviour in fixed coordinates (— $\alpha/D = 0.20$; — $\alpha/D = 0.35$; — $\alpha/D = 0.50$; α stands for the crack depth and D is the shaft diameter).

The stiffness matrix of a shaft presenting a transverse crack $\mathbf{K}_C$ (a $8x8$ matrix in agreement with the element shown in Fig.3.2) is determined by including the terms $k_{FMayes(11)}$ and $k_{FMayes(22)}$ of Eq.(3.19) into Eq.(3.20) and Eq.(3.21), according to Firswell and Penny (2002).

$$\mathbf{K}_{CXY} = \frac{12EI_Y}{L^3\left(1+\vartheta_Y\right)} \begin{bmatrix} -1 & 0 \\ L & -1 \\ 1 & 0 \\ 0 & 1 \end{bmatrix} \begin{bmatrix} k_{FMayes(11)} & \frac{L}{2} \\ \frac{L}{2} & \frac{(4+\vartheta_Y)}{12}L^2 \end{bmatrix} \begin{bmatrix} -1 & -L & 1 & 0 \\ 0 & -1 & 0 & 1 \end{bmatrix} \tag{3.20}$$

$$\mathbf{K}_{CYZ} = \frac{12EI_Y}{L^3\left(1+\vartheta_Y\right)} \begin{bmatrix} -1 & 0 \\ -L & -1 \\ 1 & 0 \\ 0 & 1 \end{bmatrix} \begin{bmatrix} k_{FMayes(22)} & -\frac{L}{2} \\ -\frac{L}{2} & \frac{(4+\vartheta_Y)}{12}L^2 \end{bmatrix} \begin{bmatrix} -1 & -L & 1 & 0 \\ 0 & -1 & 0 & 1 \end{bmatrix} \tag{3.21}$$

where I_Y is the inertia moment with respect to the Y axis and ϑ_Y is a constant that takes into account the shear effect of the Timoshenko beam FE. The stiffness matrix K_C is clearly a combination of the matrices shown in Eq.(3.20) and Eq.(3.21).

It is worth mentioning that $k_{FMayes(12)}$ (see Eq.(3.19)) is disregarded in Eq.(3.20) and Eq.(3.21) since it is much smaller than the stiffness along the X and Z directions, Cavalini-Jr. et al. (2016), Firswell and Penny (2002). Figure 3.7 shows stiffness terms $k_{FMayes(11)}$, $k_{FMayes(22)}$, and $k_{FMayes(12)}$ considering cracks of different depths present in a circular shaft cross-section. Note that the term $k_{FMayes(12)}$ is well below the direct ones.

3.6 Numerical Results

This section shows the numerical results obtained by using the proposed MSO approach. In this case, two different fault conditions are considered, namely the breathing crack and the open crack. As mentioned, the breathing behavior is modeled by following the so-called Mayes approach, Mayes and Davis (1976), in which the crack transition from fully open to fully closed is described by a cosine function. Differently, the open crack behavior considers the crack as fully open during the shaft rotation. Both crack behaviors can be observed in industrial rotating machines. For instance, breathing cracks are found in horizontal shafts, while open cracks are commonly detected in vertical shafts.

Figure 3.8 presents the time domain vibration responses of the healthy rotor FE model obtained along the X and Z directions of the nodes $\#12$ and $\#29$. The rotating machine is operating at $900\ rev/min$, and an unbalance of $6.375x10-4\ kgm/0^o$ is applied to the disc D1.

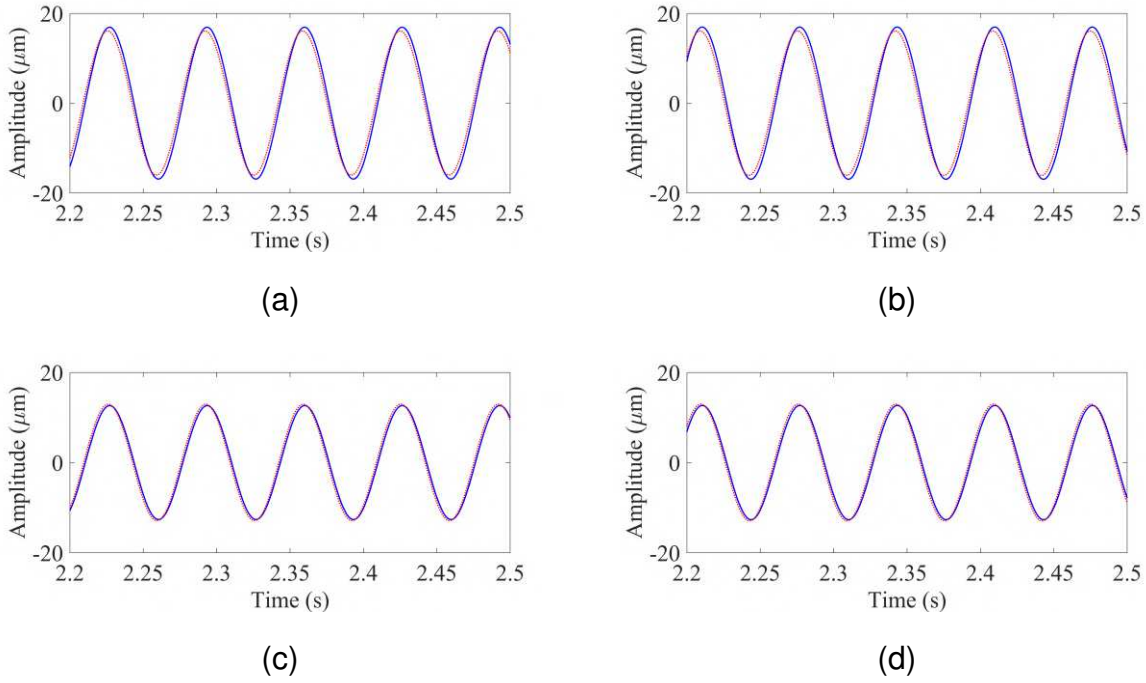

Figure 3.8: Vibration responses of the healthy rotor (—) and the associated signals estimated by using the MSO (....): (a) sensor S_{12X}; (b) sensor S_{12Z}; (c) sensor S_{29X}; (d) sensor S_{29Z}.

Figure 3.9 presents the associated time-domain vibration responses by considering

the rotor with a breathing crack with 50% depth at the element $\#22$ of the FE model (see Fig.2.1(b)). The vibration responses obtained by considering an open crack with 50% depth at the element $\#22$ are depicted in Fig.3.10. The associated vibration responses estimated by using the MSO are also presented in this figure for comparison purposes.

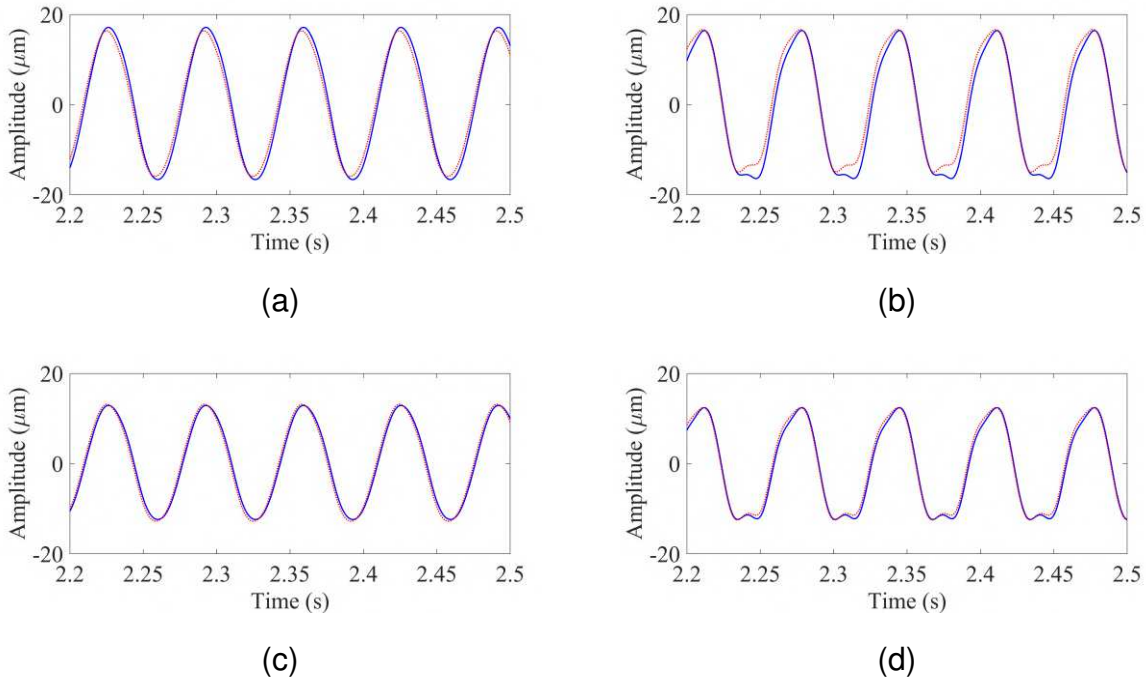

Figure 3.9: Vibration responses of the rotor with a breathing crack (—) and the associated signals estimated by using the MSO (....): (a) sensor S_{12X}; (b) sensor S_{12Z}; (c) sensor S_{29X}; (d) sensor S_{29Z}.

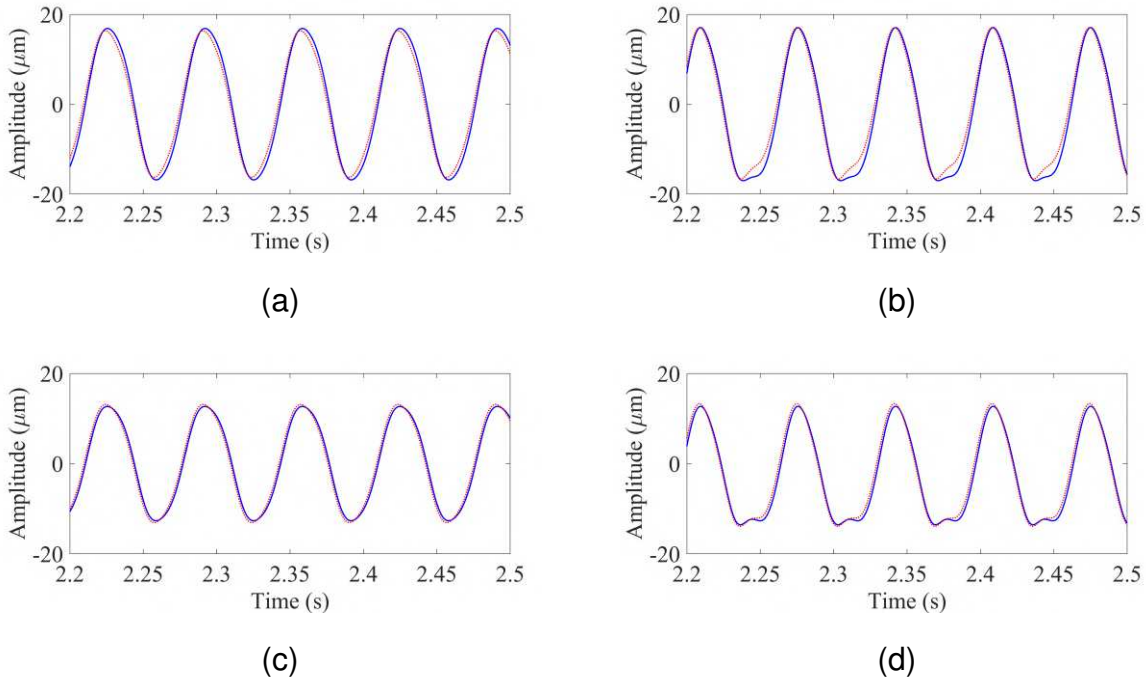

Figure 3.10: Vibration responses of the rotor with an open crack (—) and the associated signals estimated by using the MSO (....): (a) sensor S_{12X}; (b) sensor S_{12Z}; (c) sensor S_{29X}; (d) sensor S_{29Z}.

Note that the best estimation was obtained by using the vibration responses of the healthy rotor. However, all the estimated vibration responses are considered in the present work as being close enough to the reference signals.

Figure 3.11 compares the vibration responses for the healthy and faulty conditions of the rotor, in which the vibration responses determined along the Z direction (sensors S_{12Z} and S_{29Z}; see Fig.3.11(b) and Fig.3.11(d), respectively) demonstrated to be more sensitive to the fault presence. Additionally, it can be observed that the breathing and open cracks affect the dynamic behavior of the rotating machine differently.

Equation 3.22 shows the obtained observer gains (**Q** and **R**) designed to approximate the estimated vibration responses to the rotor time domain vibration responses.

$$\mathbf{Q} = \begin{bmatrix} 4x10^4 & 0 & 0 & 0 \\ 0 & 4x10^4 & 0 & 0 \\ 0 & 0 & 4x10^4 & 0 \\ 0 & 0 & 0 & 4x10^4 \end{bmatrix} \quad \mathbf{R} = \begin{bmatrix} 1x10^{-4} & 0 & 0 & 0 \\ 0 & 1x10^{-4} & 0 & 0 \\ 0 & 0 & 1x10^{-4} & 0 \\ 0 & 0 & 0 & 1x10^{-4} \end{bmatrix} \tag{3.22}$$

in which **Q** and **R** are the observer gains associated with the Kalman filter method. It

is worth mentioning that these gains were used to estimate the three shaft conditions considered in the numerical analyses of the present work.

Figure 3.12 presents the modal displacements determined by using the MSO for the healthy and faulty conditions of the rotor, which are associated with the results presented in Figs.3.8, 3.9, and 3.10. Note that the responses associated with the third vibration mode appear to be more affected by the fault existence. Additionally, the modal displacements changed according to the fault condition considered (breathing and open cracks).

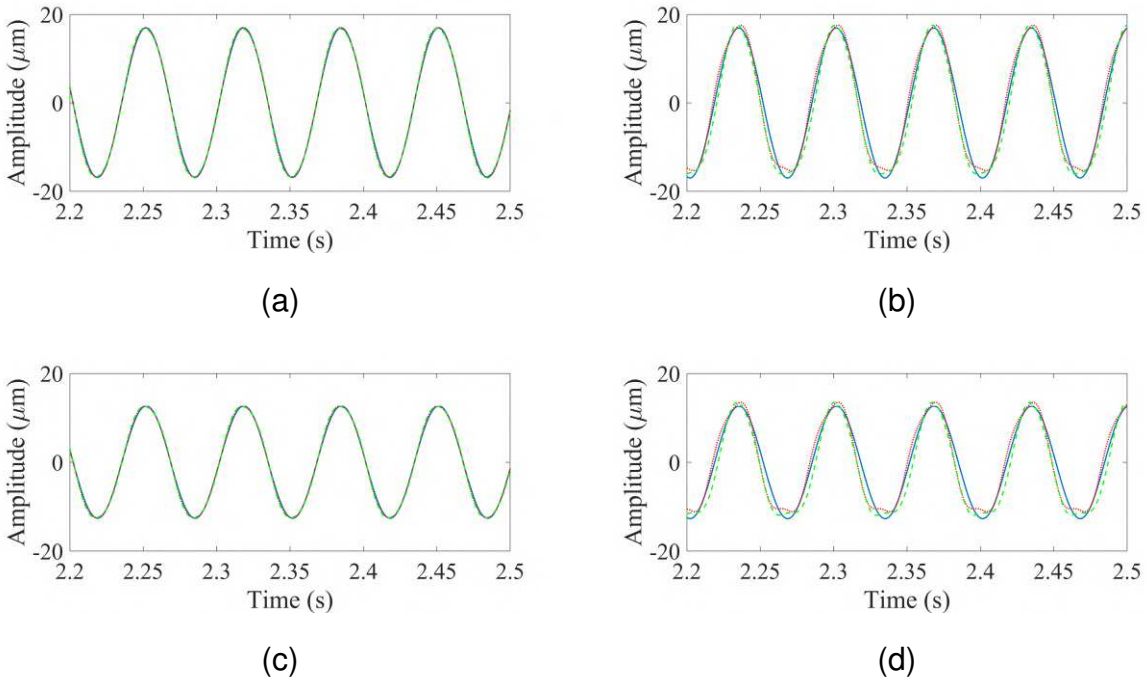

Figure 3.11: Comparison of the vibration responses of the rotor for the healthy condition (——), shaft with the breathing crack (....), and shaft with open crack (– –): (a) sensor S_{12X}; (b) sensor S_{12Z}; (c) sensor S_{29X}; (d) sensor S_{29Z}.

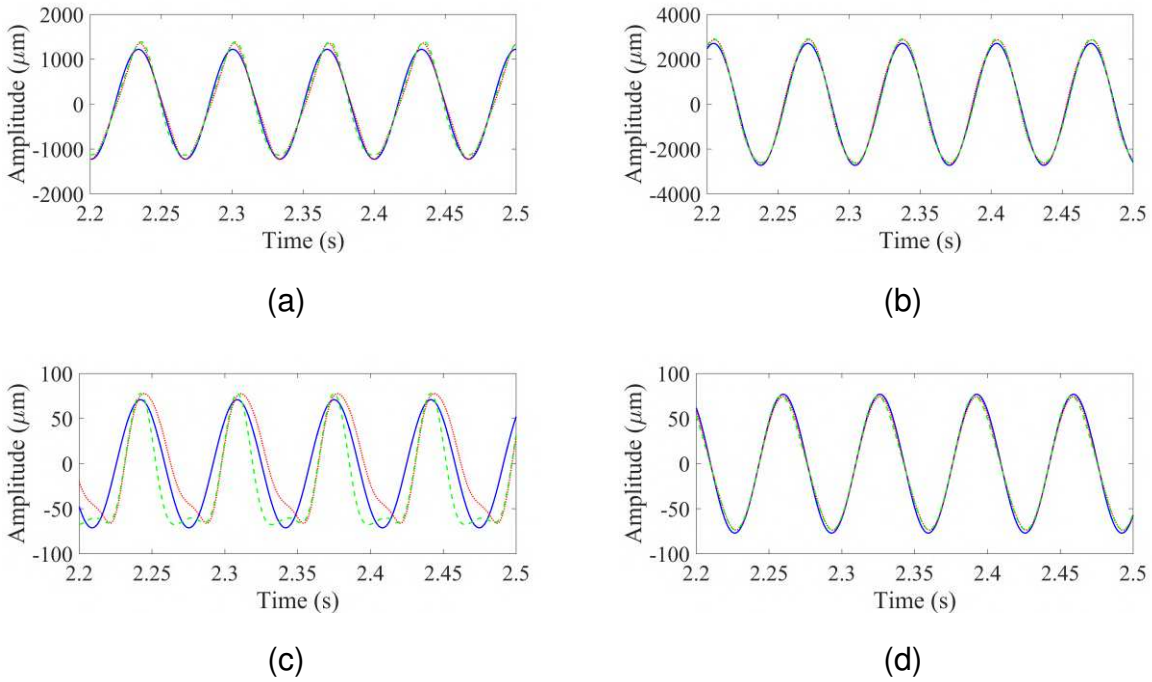

Figure 3.12: Modal displacements estimated by using the MSO for the healthy condition (——), shaft with the breathing crack (....), and shaft with open crack (– –): (a) mode $\#1$; (b) mode $\#2$; (c) mode $\#3$; (d) mode $\#4$.

Similar behavior is observed in the estimated density functions of the time domain vibration responses and modal displacements as presented in Figs.3.8 to 3.12. Figure 3.13 shows the estimated density functions of the time domain vibration responses associated with the three rotor structural conditions as presented in Figs.3.8, 3.9, and 3.10 (see the solid blue lines). Figure 3.14 presents the estimated density functions of the modal displacements shown in Fig. 3.12. The estimated modal displacements were placed intentionally around zero as presented in Fig.3.12 to determine the associated density functions of Fig.3.14.

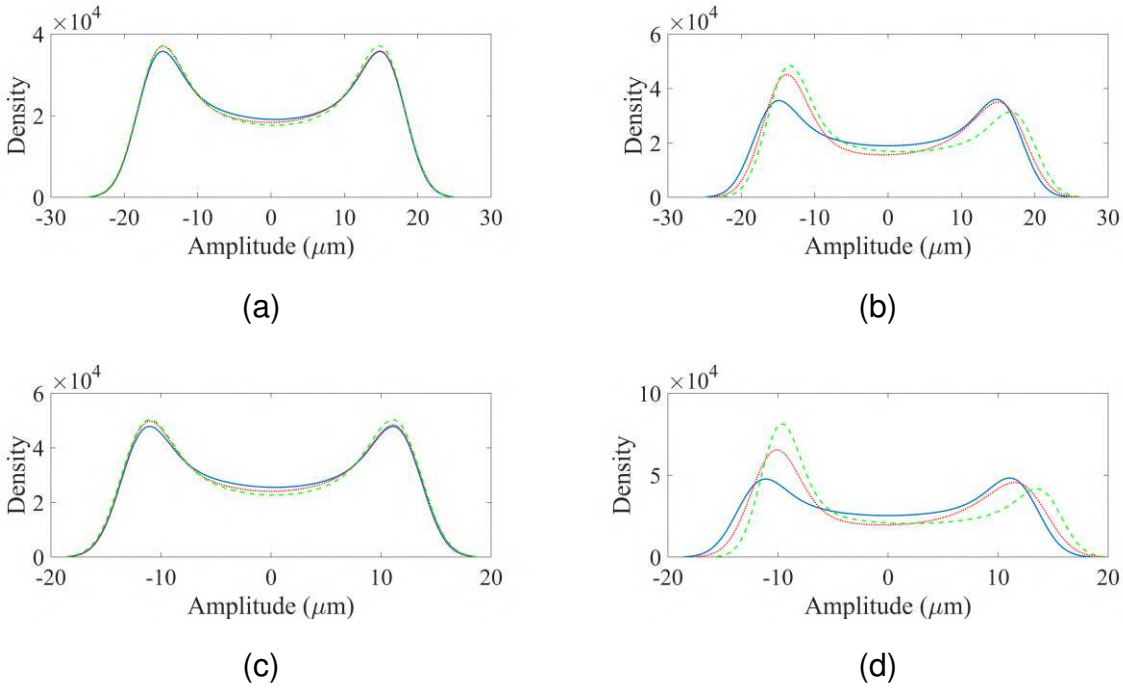

Figure 3.13: Estimated density functions of the time domain vibration responses for the healthy condition (——), shaft with the breathing crack (....), and shaft with open crack (– –): (a) sensor S_{12x}; (b) sensor S_{12z}; (c) $sensor S_{29x}$; (d) sensor S_{29z}.

Concerning the breathing and open cracks, Tabs.3.1 and 3.2, respectively, present the damage index *E* (see Eq.(3.5)) associated with the estimated density functions shown in Figs.3.13 and 3.14. The damage index obtained by considering breathing and open cracks with 10% and 30% depths in the element #22 of the rotor FE model are also presented for comparison purposes. The obtained results demonstrate that the modal displacements determined by using the MSO technique were more sensitive to the crack existence than the time domain vibration responses (see the mean values in Tabs.3.1 and 3.2). Note that the time domain vibration responses were more sensitive than the modal displacements only for the 50% crack depth case ($E = 7.63\%$ for the time domain and $E = 5.86\%$ for the modal domain).

Additionally, the biggest damage indexes were obtained from the modal displacements of the vibration mode #3 (see Fig.2.19). This behavior is associated with the changes observed in the estimated modal displacements of Fig.3.14(c). This result could also be influenced by the crack severity and position (depth and location) and the operating condition (unbalance distribution and rotation speed) of the rotating ma-

chine. However, this is a first insight only. Further investigations are necessary to correlate fault severity and operating conditions with the most affected vibration modes of the rotor aiming at proving that the modal displacements are more sensitive to fault existence than the time domain vibration responses.

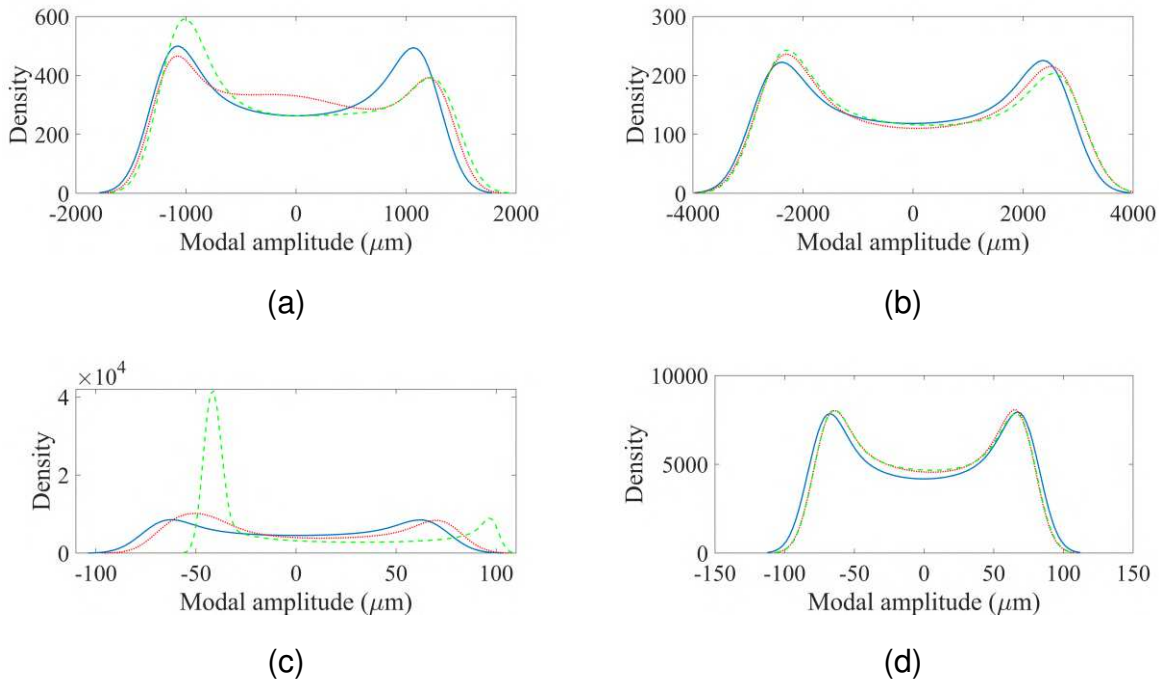

Figure 3.14: Estimated density functions of the modal displacements for the healthy condition (——), shaft with the breathing crack (....), and shaft with open crack (– –): (a) mode $\#1$; (b) mode $\#2$; (c) mode $\#3$; (d) mode $\#4$.

Table 3.1: Damage indexes obtained by considering the shaft with breathing cracks.

Time domain vibration responses					
Crack depth(%)	Sensor S_{12X}(%)	Sensor S_{12Z}(%)	Sensor S_{29X}(%)	Sensor S_{29Z}(%)	Mean value(%)
10	0.00	0.03	0.00	0.06	0.02
30	0.08	2.59	0.11	4.73	1.88
50	0.12	4.01	0.17	7.63	2.98
Modal displacements					
Crack depth(%)	Mode $\#1$(%)	Mode $\#2$(%)	Mode $\#3$(%)	Mode $\#4$(%)	Mean value(%)
10	0.01	0.01	0.11	0.01	0.04
30	1.06	0.12	8.84	0.21	2.56
50	1.77	0.21	5.86	0.58	2.11

Further results are presented in the sequence, aiming at mapping the efficiency of the MSO technique to perform crack detection for different rotor speeds and crack positions. Concerning the breathing and open cracks, Tabs. 3.3 and 3.4, respectively, present the damage index *E* (see Eq.3.5) associated with the estimated density functions obtained for the rotor operating at $2000rev/min$, $4000rev/min$, and $6000rev/min$. In this case, breathing and open cracks with 10%, 20%, and 30% depths in the element $\#22$ of the rotor FE model are being considered. Note that the MSO technique presented better results than time-domain sensors for crack detection at different rotor speeds. Tables 3.5 and 3.6 present the results obtained for breathing and open cracks, respectively, applied in the elements $\#15$, $\#19$, and $\#26$ of the rotor FE model. In this case, the rotating machine is operating at $4000rev/min$.

Table 3.2: Damage indexes obtained by considering the shaft with open cracks.

Time domain vibration responses					
Crack depth(%)	Sensor S_{12X}(%)	Sensor S_{12Z}(%)	Sensor S_{29X}(%)	Sensor S_{29Z}(%)	Mean value(%)
10	0.00	0.06	0.01	0.14	0.05
30	0.17	4.66	0.34	16.88	5.51
50	0.23	7.63	0.48	29.32	9.41
Modal displacements					
Crack depth(%)	Mode $\#1$(%)	Mode $\#2$(%)	Mode $\#3$(%)	Mode $\#4$(%)	Mean value(%)
10	0.01	0.01	0.29	0.01	0.08
30	1.03	0.27	61.08	0.35	15.68
50	1.76	0.45	180.85	1.07	46.03

Table 3.3: Damage indexes obtained by considering the shaft at different speeds with breathing cracks.

Time domain vibration responses						
Speed (rev/min)	Crack depth (%)	Sensor S_{12X} (%)	Sensor S_{12Z} (%)	Sensor S_{29X} (%)	Sensor S_{29Z} (%)	Mean value (%)
2000	10	0.00	0.00	0.00	0.00	0.00
	30	0.03	0.05	0.03	0.05	0.04
	50	0.05	0.10	0.07	0.11	0.09
4000	10	0.01	0.00	0.00	0.00	0.00
	30	0.29	0.21	0.14	0.10	0.18
	50	0.51	0.40	0.19	0.14	0.31
6000	10	0.00	0.00	0.00	0.00	0.00
	30	0.05	0.14	0.03	0.11	0.08
	50	0.14	0.35	0.04	0.21	0.18
Modal displacements						
Speed (rev/min)	Crack depth (%)	Mode #1 (%)	Mode #2 (%)	Mode #3 (%)	Mode #4 (%)	Mean value (%)
2000	10	0.00	0.00	0.00	0.00	0.00
	30	0.19	0.02	0.73	0.22	0.29
	50	0.26	0.06	1.75	0.70	0.69
4000	10	0.00	0.00	0.38	0.00	0.10
	30	0.05	0.03	9.82	0.22	2.53
	50	0.14	0.06	10.58	0.53	2.83
6000	10	0.00	0.00	0.03	0.01	0.01
	30	0.03	0.01	1.09	0.45	0.40
	50	0.04	0.02	1.38	1.38	0.71

Table 3.4: Damage indexes obtained by considering the shaft with open cracks.

Time domain vibration responses						
Speed (rev/min)	Crack depth (%)	Sensor S_{12X}SS (%)	Sensor S_{12Z} (%)	Sensor S_{29X} (%)	Sensor S_{29Z} (%)	Mean value (%)
2000	10	0.00	0.00	0.00	0.00	0.00
	30	0.09	0.17	0.10	0.14	0.12
	50	0.21	0.32	0.27	0.34	0.28
4000	10	0.02	0.01	0.02	0.01	0.02
	30	1.18	0.85	0.66	0.35	0.76
	50	2.11	1.47	0.83	0.50	1.23
6000	10	0.00	0.00	0.00	0.00	0.00
	30	0.14	0.14	0.05	0.06	0.10
	50	0.41	0.40	0.06	0.08	0.24
Modal displacements						
Speed (rev/min)	Crack depth (%)	Mode #1 (%)	Mode #2 (%)	Mode #3 (%)	Mode #4 (%)	Mean value (%)
2000	10	0.02	0.00	0.02	0.02	0.01
	30	0.75	0.07	1.47	0.67	0.74
	50	1.09	0.19	3.93	2.20	1.85
4000	10	0.00	0.00	1.30	0.01	0.33
	30	0.18	0.10	10.90	0.82	3.00
	50	0.43	0.28	11.43	1.79	3.48
6000	10	0.00	0.00	0.02	0.00	0.01
	30	0.05	0.02	0.75	0.15	0.24
	50	0.10	0.06	0.97	0.41	0.39

It can be observed that the efficiency of the MSO does not depend on the position of the crack nor the rotor speed. It is worth mentioning that the third mode was once more the most affected by the presence of the crack for all the scenarios. The results presented in Tabs.3.3, 3.4, 3.5, and 3.6 shown similar results as given by Figs.3.8 to 3.14.

3.7 Experimental Results

This section shows the experimental results obtained by using the proposed MSO approach. In this case, two different fault conditions are considered, namely a breathing crack and an open crack with 50$\%$ depth. The cracks are located between the discs D1 and D2 of the rotating machine, corresponding to the element $\#22$ of the FE model (see Fig.2.1(b)). Unlike the numerical results, only the faulty conditions are analyzed in this section. The results obtained from the breathing and open cracks are compared, aiming at highlighting the ability of the MSO approach to detect variations on the structural integrity of the rotating shaft. The open crack condition is characterized by creating a small notch on the shaft by using a wire electrical discharge machine (see Fig.3.15b). During the shaft rotation, the notch edges do not touch each other. The breathing crack condition (see Fig.3.15a) was obtained by introducing a shim in the crack area intending to simulate the breathing mechanism.

Table 3.5: Damage indexes obtained by considering the shaft with breathing cracks.

Time domain vibration responses						
Crack location	Crack depth (%)	Sensor S_{12X} (%)	Sensor S_{12Z} (%)	Sensor S_{29X} (%)	Sensor S_{29Z} (%)	Mean value (%)
Element #15	10	0.00	0.00	0.00	0.00	0.00
	30	0.10	0.06	0.12	0.06	0.09
	50	0.13	0.08	0.15	0.11	0.12
Element #19	10	0.00	0.00	0.00	0.00	0.00
	30	0.07	0.06	0.07	0.05	0.06
	50	0.11	0.11	0.17	0.13	0.13
Element #26	10	0.01	0.01	0.01	0.00	0.01
	30	0.48	0.37	0.28	0.17	0.32
	50	0.75	0.62	0.35	0.23	0.48
Modal displacements						
Crack location	Crack depth (%)	Mode #1 (%)	Mode #2 (%)	Mode #3 (%)	Mode #4 (%)	Mean value (%)
Element #15	10	0.00	0.00	0.18	0.00	0.05
	30	0.02	0.01	12.55	0.30	3.22
	50	0.05	0.02	18.82	0.06	4.88
Element #19	10	0.00	0.00	0.12	0.00	0.30
	30	0.07	0.02	7.46	0.05	1.90
	50	0.17	0.06	12.01	0.12	3.09
Element #26	10	0.00	0.00	0.76	0.02	0.19
	30	0.05	0.01	11.64	1.17	3.22
	50	0.09	0.03	12.32	2.90	3.84

It is worth mentioning that the shaft of the rotor test rig was manufactured with the notch presented in Fig.3.15b (Machinery Fault $\&$ Rotor Dynamics Simulator manufactured by Spectra Quest Inc). Thus, the experimental FRFs used in the model updating procedure were obtained with the shim placed in the shaft (see Fig.3.15a) to minimize the influence of the crack existence on the measured vibration responses, aiming at

simulating the healthy shaft condition.

Figure 3.16 presents the time domain vibration responses of the rotor with the breathing crack. The signals were measured by using the sensors S_{12X}, S_{12Z}, S_{29X}, and S_{29Z} with the rotating machine operating at $900rev/min$. Figure 3.17 presents the associated time-domain vibration responses by considering the rotor with the open crack. The associated vibration responses estimated by using the MSO are also presented for comparison purposes. Note the experimental vibration responses of the rotor were not well estimated by the MSO. There are some non-modeled dynamics, especially related to bow and misalignment present on the rotating machine. The results presented in Fig.3.16 and 3.17 show the best possible fitting for experimental vibration responses and MSO estimated signals. Additionally, a comparison among the experimental vibration responses demonstrates that the breathing and open cracks lead to the similar dynamic behavior of the rotating machine.

Table 3.6: Damage indexes obtained by considering the shaft with open cracks.

Time domain vibration responses						
Crack location	Crack depth (%)	Sensor S_{12X} (%)	Sensor S_{12Z} (%)	Sensor S_{29X} (%)	Sensor S_{29Z} (%)	Mean value (%)
Element #15	10	0.01	0.01	0.01	0.00	0.01
	30	0.43	0.22	0.43	0.24	0.33
	50	0.52	0.27	0.64	0.42	0.46
Element #19	10	0.01	0.00	0.01	0.00	0.01
	30	0.36	0.22	0.35	0.20	0.28
	50	0.61	0.44	0.73	0.52	0.57
Element #26	10	0.05	0.03	0.03	0.01	0.03
	30	1.73	1.22	1.03	0.55	1.13
	50	2.45	2.07	1.11	0.66	1.57
Modal displacements						
Crack location	Crack depth (%)	Mode #1 (%)	Mode #2 (%)	Mode #3 (%)	Mode #4 (%)	Mean value (%)
Element #15	10	0.00	0.00	0.69	0.03	0.18
	30	0.03	0.02	46.69	0.72	11.87
	50	0.08	0.05	40.51	2.26	10.72
Element #19	10	0.00	0.00	0.43	0.00	0.11
	30	0.18	0.08	37.25	0.13	9.41
	50	0.38	0.23	49.96	0.37	12.74
Element #26	10	0.00	0.00	2.63	0.07	0.68
	30	0.12	0.04	12.89	3.41	4.12
	50	0.29	0.10	16.48	7.61	6.12

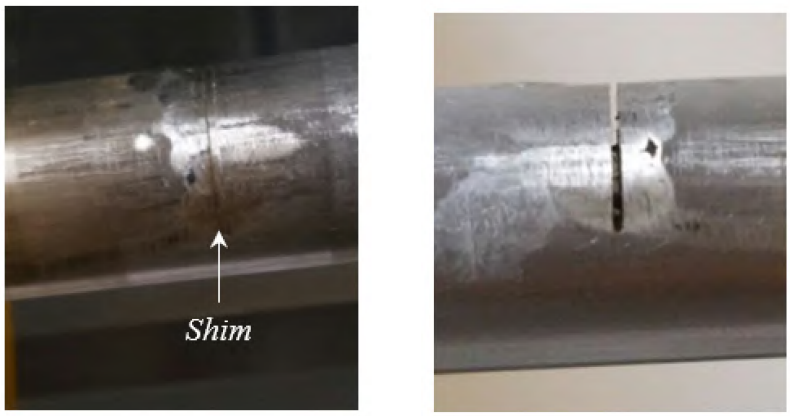

(a) (b)

Figure 3.15: Crack conditions: (a) breathing crack; (b) open crack.

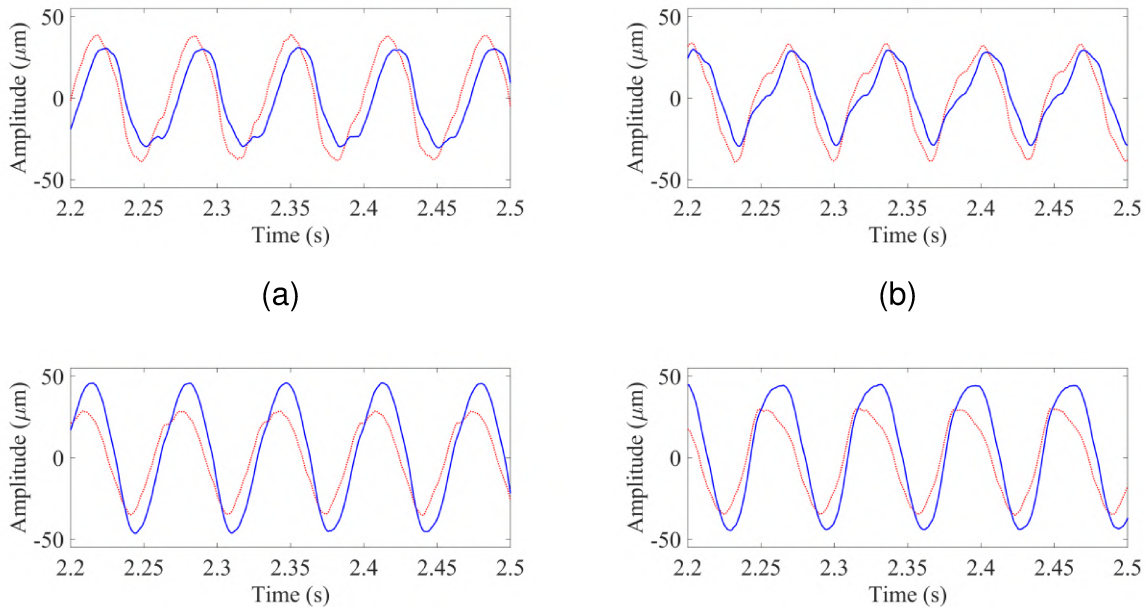

(a) (b)

(c) (d)

Figure 3.16: Experimental vibration responses of the rotor with a breathing crack (—) and the associated signals estimated by using the MSO (....): (a) sensor S_{12X}; (b) sensor S_{12Z}; (c) sensor S_{29X}; (d) sensor S_{29Z}.

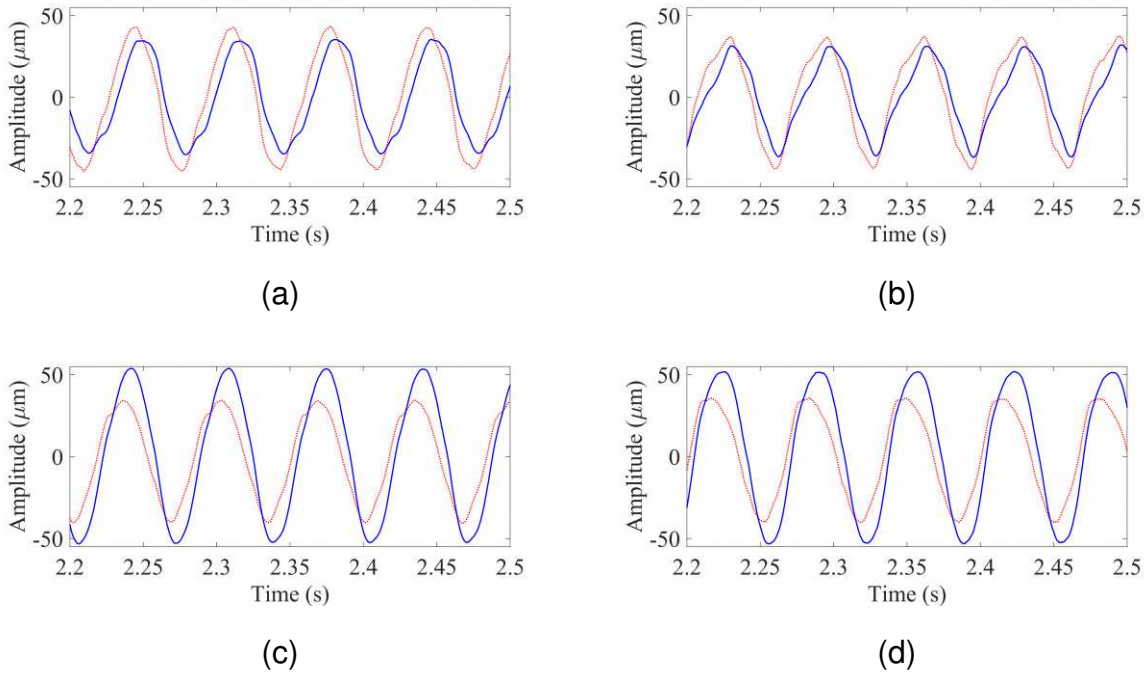

Figure 3.17: Experimental vibration responses of the rotor with a open crack (—) and the associated signals estimated by using the MSO (....): (a) sensor S_{12X}; (b) sensor S_{12Z}; (c) sensor S_{29X}; (d) sensor S_{29Z}.

Equation (3.23) shows the observer gains (**Q** and **R**) designed to approximate the estimated vibration responses to the experimental data. These gains were used to estimate the two shaft conditions considered in the experimental analyses.

$$\mathbf{Q} = \begin{bmatrix} 1x10^{3} & 0 & 0 & 0 \\ 0 & 1x10^{3} & 0 & 0 \\ 0 & 0 & 1x10^{3} & 0 \\ 0 & 0 & 0 & 1x10^{3} \end{bmatrix} \quad \mathbf{R} = \begin{bmatrix} 5x10^{-5} & 0 & 0 & 0 \\ 0 & 5x10^{-5} & 0 & 0 \\ 0 & 0 & 5x10^{-5} & 0 \\ 0 & 0 & 0 & 5x10^{-5} \end{bmatrix} \tag{3.23}$$

Figure 3.18 shows the modal displacements determined by using the MSO technique for the considered fault conditions of the rotor, which are associated with the results presented in Fig. 3.17. Note that the responses associated with the first and second vibration modes demonstrate to be more affected as the fault condition changes (breathing to open crack condition).

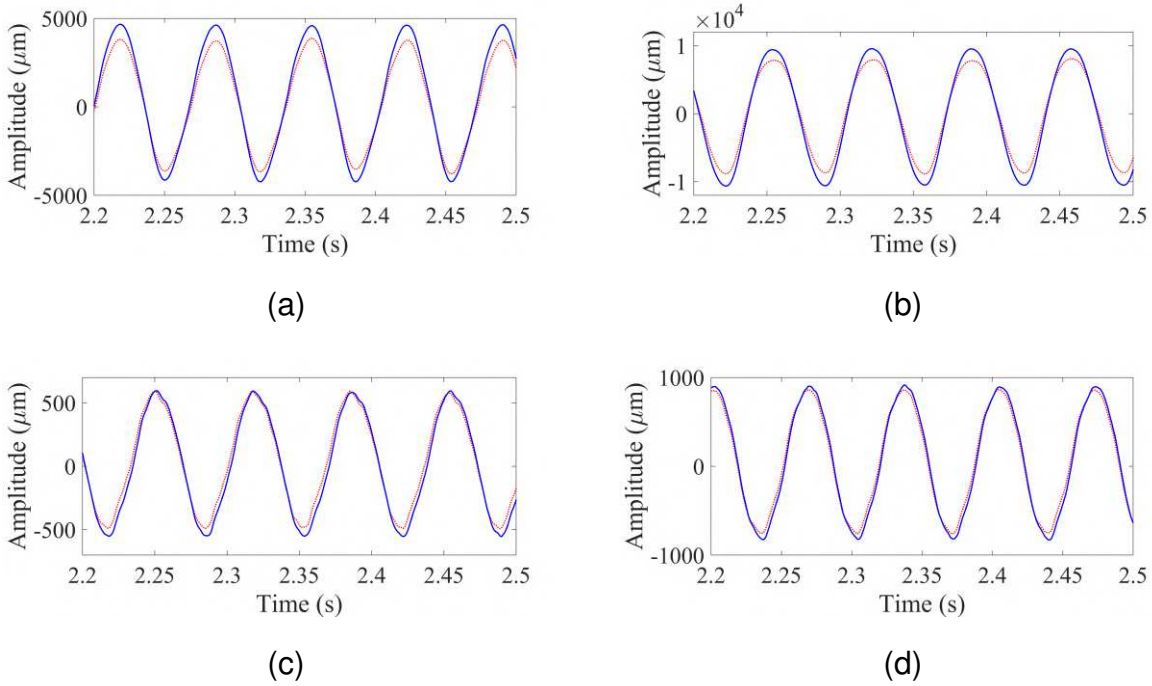

Figure 3.18: Experimental modal displacements estimated by using the MSO for the shaft with an open crack (—) and the associated signals estimated by using the MSO (....): (a) mode $\#1$; (b) mode $\#2$; (c) mode $\#3$; (d) mode $\#4$.

Similar behavior is observed in the estimated density functions of the time domain vibration responses and modal displacements presented in Figs.3.16 to 3.18. Figure 3.19 shows the estimated density functions of the time domain vibration responses associated with the two rotor structural conditions, as presented in Figs. 3.16 and 3.17 (see the solid blue lines). The estimated density functions of the modal displacements shown in Fig.3.18 are depicted in Fig.3.20.

Table 3.7 presents the damage index *E* (see Eq. (3.5)) associated with the estimated density functions presented in Figs.3.19 and 3.20. The obtained damage index demonstrates that the modal displacements estimated by using the MSO approach were more sensitive to fault variation than the time domain vibration responses (breathing to open crack behaviour).

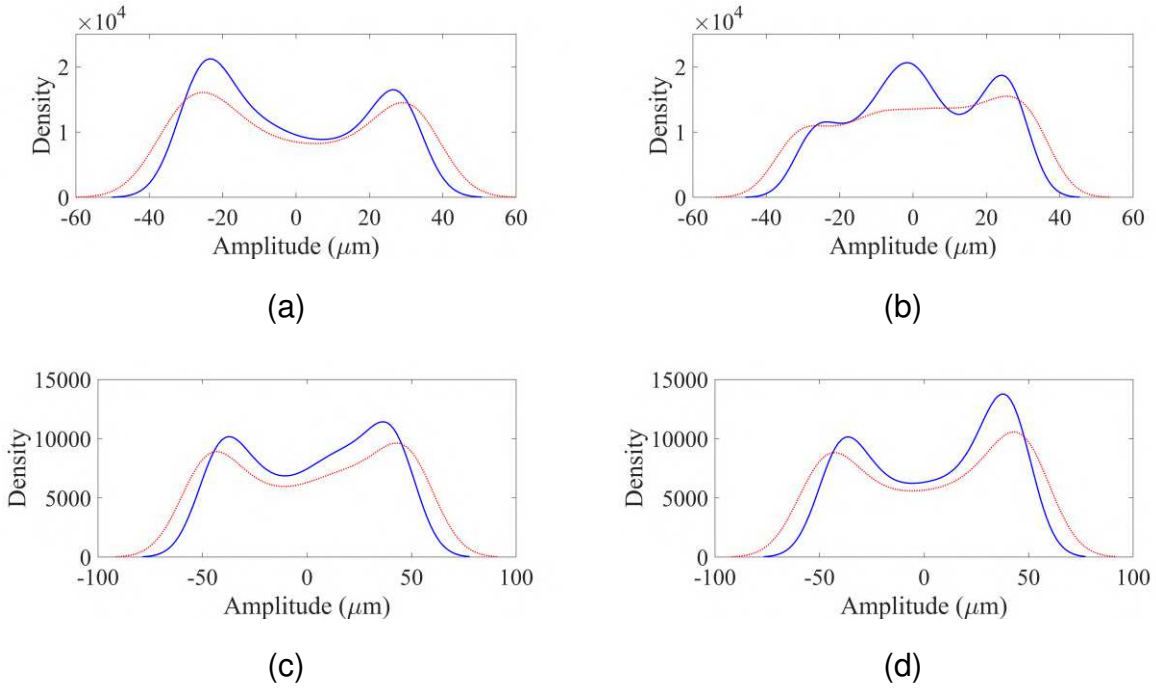

Figure 3.19: Estimated density functions of the experimental time domain vibration responses for the shaft with the breathing crack (—) and the shaft with the open crack (....): (a) sensor S_{12X}; (b) sensor S_{12Z}; (c) sensor S_{29X}; (d) sensor S_{29Z}.

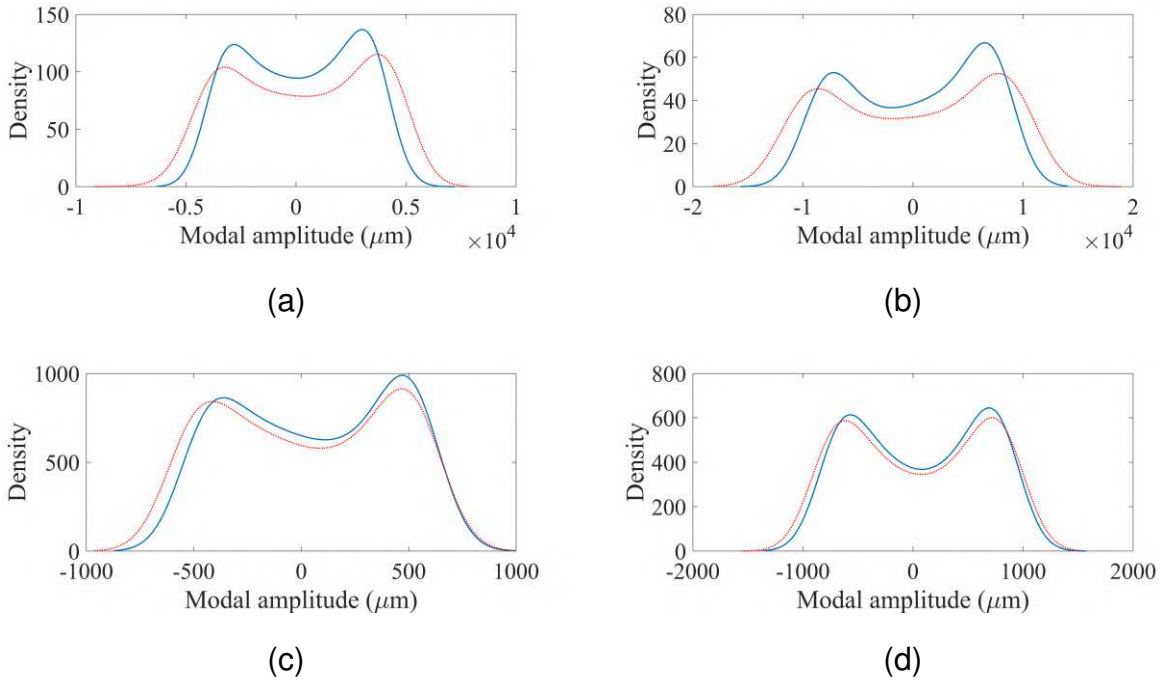

Figure 3.20: Estimated density functions of the experimental modal displacements for the shaft with the breathing crack (—) and the shaft with the open crack (....): (a) mode $\#1$; (b) mode $\#2$; (c) mode $\#3$; (d) mode $\#4$.

Table 3.7: Damage indexes obtained by considering the shaft with breathing and open cracks.

Time domain vibration responses				
Sensor S_{12X} (%)	Sensor S_{12Z} (%)	Sensor S_{29X} (%)	Sensor S_{29Z} (%)	Mean value (%)
4.07	4.63	2.18	3.26	3.54
Modal displacements				
Mode #1 (%)	Mode #2 (%)	Mode #3 (%)	Mode #4 (%)	Mean value (%)
15.89	7.71	4.14	3.42	7.79

In Tab. 3.7, note that the maximum difference determined by using the modal displacements was 15.89$\%$ (first vibration mode), while a difference of 4.63$\%$ was obtained by using the sensor S_{12Z}.

As mentioned, the biggest damage index was obtained for the first modal displacement. This result indicates that the first vibration mode was more affected by the fault variation (breathing to open crack behavior) as compared with the other modes. In the numerical results, however, even when the crack location is similar, the third mode was the most affected. The healthy rotor and the rotor corresponding to various breathing crack conditions were compared by performing numerical simulations. It was concluded that different fault conditions would affect the rotor modes differently.

It is worth mentioning that the considered rotation speed ($900 rev/min$) does not have any relation with the critical speeds of the rotating machine. It is known that multiples and submultiples of critical speeds make easier the crack detection process. Consequently, the MSO technique can be applied without the necessity of running the rotor out of its operational speed.

3.8 Partial Conclusions

In the present contribution, the MSO approach was evaluated both numerically and experimentally for crack detection purposes as applied to a rotating machine. The obtained results demonstrate that the estimated modal displacements are more sensitive to the fault existence than the time domain vibration responses of the rotor (see the mean values in Tabs. 3.1 to 3.7). The method is able to estimate modal displacements and velocities associated with the time domain vibration responses measured directly on the rotor. Thus, more sensitive modal information was obtained by using the MSO technique. Sensitive modal displacements were obtained since the MSO is fed with the model of the healthy rotating machine and its time-domain vibration responses. Consequently, the MSO behaves as a filter of states highlighting the difference between the shaft with and without a crack.

The healthy and faulty shaft conditions were considered in the numerical simulations. Breathing and open cracks with 10%, 30%, and 50% depth at the elements $\#15$, $\#19$, $\#22$, and $\#26$ of the FE model were analyzed separately. Various rotating speeds were considered, namely 900 rev/min, 2000 rev/min, 4000 rev/min, and 6000 rev/min. The time-domain vibration responses were more sensitive than the modal displacements only for the case in which a breathing crack with 50% depth was

considered. In this case, the vibration mode #3 was the most affected by the fault. This result can be associated with the crack severity (depth and location) and the operating condition (unbalance distribution and rotation speed) of the rotating machine.

The breathing crack and open crack conditions were considered in the experimental analysis. The results demonstrate that the modal displacements estimated by using the MSO approach were more sensitive to fault variation than the time domain vibration responses (breathing to open crack behavior). Differently from the numerical results, the first vibration mode was the most affected by the fault condition. However, in the numerical results, the healthy and breathing crack conditions were compared (the crack location was similar). Consequently, different faults affected the rotor modes differently.

The estimated vibration responses by using the MSO do not match perfectly the experimental measurements. There are some non-modeled dynamics, especially related to bow and misalignment that are not taken into account in the model. Thus, a difference is expected between the numerical and experimental results using the proposed approach in terms of the most affected mode shapes by the crack existence. Further investigations comparing numerical and experimental results are necessary to correlate fault severity and operating conditions to the most affected vibration modes of the rotating machine.

As mentioned, this chapter was dedicated to proving that the modal displacements can be more sensitive to fault existence than the time domain vibration responses. The MSO technique demonstrated to be a simple and efficient alternative tool for fault detection in rotordynamics. The proposed methodology can be used to detect other types of faults than cracks. However, the MSO alone is not able to recognize which type of fault is found in the system since different malfunctions affecting rotating machines can lead to similar dynamic responses (e.g., crack and misalignment).

Chapter 4

Crack Control in Rotating Machinery

4.1 Introduction

As previously stated, this Ph.D. dissertation is divided in two main parts. In the first one, which is composed of Chap. 2 and Chap. 3, the problem of crack detection was addressed.

The second part of this research work takes place from now on. After detecting the existence of a transverse crack along a rotating shaft, it is necessary to control the size of this crack, searching for decreasing its effects on the rotating machine, avoiding a complete failure of the structure.

In this chapter, the term *crack control* is explained; then, the test rig devoted to crack control is presented together with its main components; in the sequence, the equation of motion of the rotor is developed by using the FE method. Finally, a numerical updating procedure is applied, on both time and frequency domains, for guaranteeing the numerical responses to be close to the dynamic responses from the experimental test rig.

The term "crack control" is used in this dissertation aiming at controlling the amplitudes of the $2X$ and $3X$ super-harmonics, which are crack signatures. It means that when a crack is generated in a rotating shaft, its frequency spectrum presents an increase in the $2X$ and $3X$ super-harmonics, according to Bachschmid et al. (2000). In this way, by suppressing the levels of $2X$ and $3X$ super-harmonics, it is expected that the crack effects on the structure are also decreased.

4.2 Rotor Test Rig for Crack Control

In this chapter, the second test rig, which is devoted to crack control is presented. This test rig is used for generating all the numerical and experimental data concerning crack control in the present work.

This test rig is also located at the Laboratory of Mechanical Structures (LMEst), of the Federal University of Uberlândia (UFU) and was designed by Cavalini-Jr (2013) and Koroishi (2013) for their Ph.D. research works. For the present dissertation, some hardware updates were applied to this test rig, which are commented later in this chapter.

This chapter maintains the same structure of Chap.2. First the crack control test rig is presented, and its main components are detailed. Then, the equation of motion for this test rig is presented in order to build its corresponding FE numerical model. Finally, an updating procedure takes place for converging the numerical results of the FE model to the experimental results collected from the test rig.

Figure 4.1 presents the test rig for performing crack control. A new FE numerical model, considering 31 elements is built for representing the dynamic behavior of this new test rig.

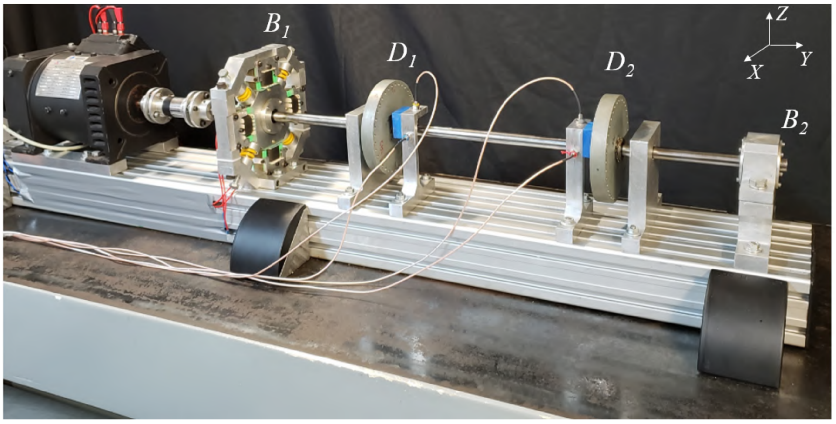

(a)

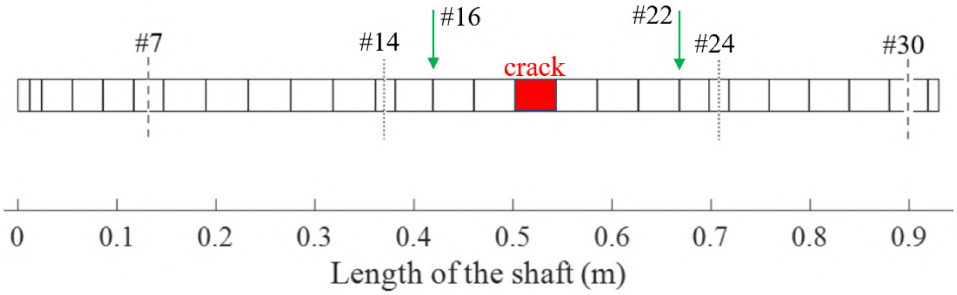

(b)

Figure 4.1: Test rig used for crack control: (a) real test rig; (b) mesh for the FE model.

This second test rig is also mounted on an isolated table, which attenuates external vibration influences. The flexible steel shaft presents a diameter of $17\ mm$ and is $930\ mm$ long. The material of the shaft the SAE 1045 steel, rectified type $h7$, whose main mechanical properties are the following $E = 182GPa$, $\rho = 7930kg/m^3$, and $\mu = 0.29$.

A transverse crack with 50% relative depth is produced on this shaft at the position of element $\#18$, as depicted by Fig.4.2.

Figure 4.2: Transverse crack on the shaft.

Two rigid discs made of steel SAE 1020 are mounted on the shaft, namely D_1 ($2.599kg$), at node $\#14$ and D_2 ($2.587kg$), at node $\#24$. The discs present $150mm$ of diameter and $20mm$ of thickness. The discs are connected to the shaft by the use of conical bushings, produced by BLG®, model $BH304$.

Figure 4.3 presents the disc and its bushing. These discs and bushings were also used by Cavalini-Jr (2013) in his Ph.D. dissertation; more details about them are provided in this reference.

Figure 4.3: Disc and bushing used on the test rig.

The same double row self-aligning ball bearings are used for supporting the shaft. However, one of the bearings is able to move for controlling shaft vibrations, while

supporting the shaft. This bearing is named hybrid bearing. As depicted by Fig.4.1, the fixed bearing (B_2) is located at node $\#30$, while the hybrid bearing (B_1) is placed at node $\#7$. Details about both fixed bearing and hybrid bearing are furnished later in this section.

Displacement sensors from (SKF®, model CMSS 65-002-00-12-10) orthogonally mounted for measuring the dynamic response of the system. They are placed on the nodes $\#16$ (S_{16_X} and S_{16_Z}) and $\#22$ (S_{22_X} and S_{22_Z}), for collecting the shaft vibration responses.

An electric motor, using alternate current, and presenting a nominal power of $1/2\ hp$ is used to drive the system. Its model is $BN90M$, and it is produced by Varimot®. This motor possesses a speed limit of $4200\ rev/min$, equivalent to $70\ Hz$, and is depicted in Fig. 4.4.

Figure 4.4: Electric motor.

An aluminum frame ($90x180L$), furnished by Bosch Rexroth Corp® is used to support the rotating machine on the isolated table. Figure 4.5 presents the aluminum frame geometry.

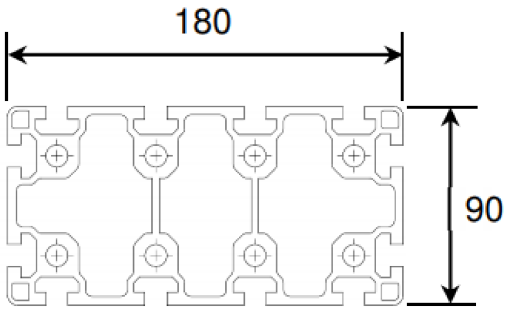

Figure 4.5: Aluminum profile 90x180L.

Rotor speed control is performed by a PID controller with an accuracy of 1 rev/min. The controller was developed at the LMEst and disposes of a manual speed control, according to Fig.4.6. For this reason, the results of this study are presented only for constant speeds.

Figure 4.6: Manual rotor speed controller.

For transmitting power from the electric motor to the shaft, a mechanical coupling is required. In this work, a Lami-Torq®, model $GTG402100$ is used, as shown in Fig.4.7. This coupling is made in aluminium and is dedicated to absorbing the misalignment between the electric motor and the shaft.

Figure 4.7: Mechanical coupling.

Concerning the bearings, both hybrid and fixed bearings are now detailed. The fixed bearing (B_2 on Fig.4.1) was produced at LMEst and machined in aluminum. It contains a double row self-aligning ball bearing furnished by FAG®, model $1204 - K - TVH - C3$. This ball bearing possesses a conical inner ring, which allows the same conical bushings used on the discs to attach them to the shaft. In fig. 4.8 the details of this bearing are shown.

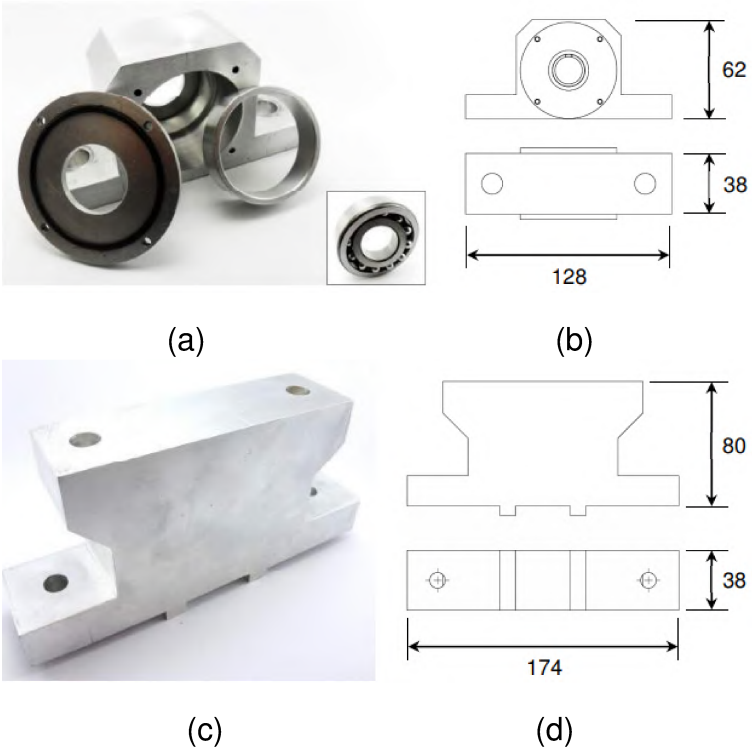

Figure 4.8: Self aligning bearing: a) details of its components; b) main dimensions (mm); c) base to connect the bearing to the aluminum frame; d) geometry of the base.

The hybrid bearing, B_1, is presented in Fig.4.1. Besides supporting the shaft, it is also able to apply external forces through the electromagnetic actuators (EMAs). According to Cavalini-Jr (2013), other hybrid bearings similar to this one exist in other research laboratories around the world, such as the LaMCoS (Laboratoire de Mécanique des Structures), at INSA-Lyon, and the Rotating Machines Laboratory (Laboratório de Máquinas Rotativas), at UNICAMP. However, the design of this specific bearing which is presented in fig. 4.9 was developed at LMEst, by Cavalini-Jr (2013) and Koroishi (2013).

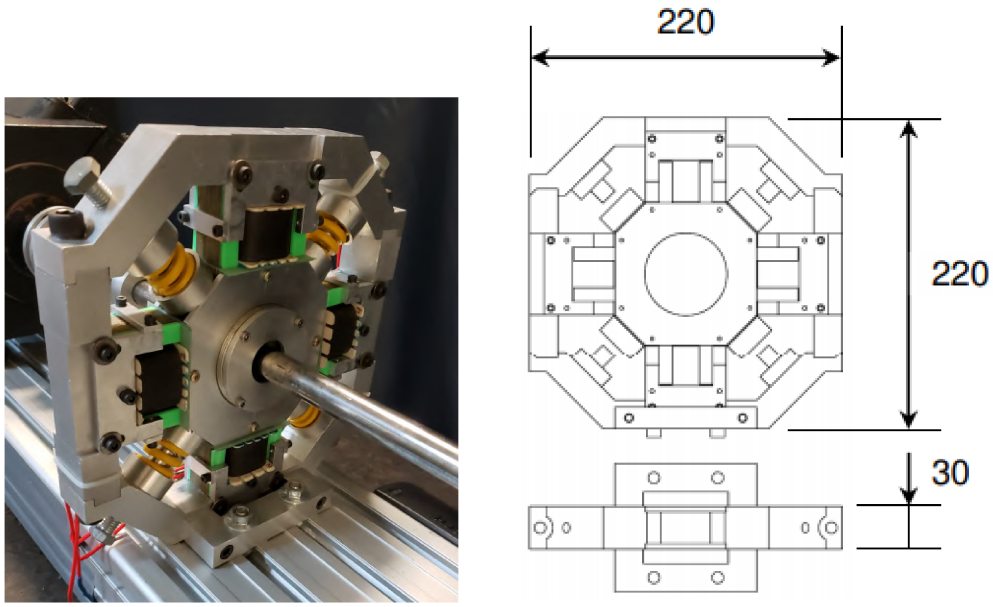

(a) (b)

Figure 4.9: (a) Hybrid bearing; (b) main dimensions.

The hybrid bearing is composed of four EMAs on its external fixed part. At its central moving part, there is a double row self-aligning ball bearing, having the same model and manufacturer as the one of the fixed bearing. Besides, there are four fixed springs, $1.5mm$ compressed, allowing for the lateral movements of the shaft. These springs aim at filtering the non-linearities produced by the electromagnetic forces.

The EMAs used to compose the hybrid bearing are shown in figure 4.10. Each of them is composed of two parts, being an E shaped part, called *core*, and an I shaped part, called *target*. These actuators have 250 winding and are able to apply forces up to $150N$ (each one) when a current of $2.5A$ is applied to it, according to Koroishi (2013). More characteristics of these EMAs and a brief electromagnetism background is presented in Chap.5.

Figure 4.10: EMA used to compose the hybrid bearing.

In order to apply the required electrical currents to each EMA, four current amplifiers are used. They are manufactured by Maxon®, model $ADS50/10201583$, being able to furnish up to 10A. The four sets of EMAs and current amplifiers impose some phase delays to the system. In this way, it is important to know these delays and to comensate them in the FE code, so that the numerical control responses fit to the experimental test rig, satisfactorily. A dynamic characterization of the full control system, the current amplifiers and the EMAs are also presented in Chap.5.

More details about this test rig components can be found in Cavalini-Jr (2013) and Koroishi (2013).

Next section presents the FE numerical model as well as its updating procedure, based on the time and frequency domain signals, as collected from the experimental crack control test rig.

4.3 Rotor Equation of Motion for Crack Control

The same equation of motion considered for the crack detection numerical model is used for this new test rig. The only difference is that a new force $\mathbf{F}_{EMA}$ has to be taken into account. It represents the control forces, fixed in space, applied by the EMAs, which are calculated according to the procedure presented in Chap.5.

All the other matrices that appear in Eq.4.1 were previously described in Chap.2. Note that a gain k multiplies the electromagnetic force vector. This gain is responsible for changing the position of poles and zeros of the system, as explained in Chap.6.

$$\mathbf{M}\ddot{\mathbf{q}} + [\mathbf{D} + \Omega\mathbf{D}_g]\,\dot{\mathbf{q}} + \mathbf{K}\mathbf{q} = \mathbf{W} + \mathbf{F}_u + k\mathbf{F}_{EMA} + \Delta\mathbf{K}\mathbf{q} \tag{4.1}$$

The full procedure for generating each system matrix is detailed in Lallane and Ferraris (1997). The same finite element, with 2 nodes and 4 degrees of freedom per node used again in the formulation of this new model.

Moreover, the same system reduction, namely the pseudo-modal approach, is used again for modeling the crack control test rig. The Pseudo-Modal method reduces the order of the numerical model from $124x124$ to $12x12$ since it considers only the influence of the first 12 natural modes. The Hankel singular values distribution presented in Chap. 2 is applied once more in the present chapter.

4.4 FE Model Updating

The updating procedure described in Chap. 2 takes place again in the present chapter in order to validate and update the numerical model. The same optimization routine is applied, considering the particular features of the crack control test rig.

A new speed range is considered for adjusting the crack control numerical model. In this way, the numerical model behaves dinamically in a similar manner of the experimental test rig, in the considered speed range.

4.4.1 Frequency Domain Updating

The same heuristic code, based on Differential Evolution Storn and Price (1995) is applied to determine the optimal parameters that solve an inverse problem regarding the model updating of the numerical model with respect to the experimental responses.

The same optimization parameters are considered for this new updating procedure (initial population counting with 90 individuals, difference amplification among the individuals of $F_{DE} = 0.8$, mutation ratio of $CR_{DE} = 0.5$, as recommended by Viana et al. (2007)). Moreover, the experimental modal analysis is also similar to the one presented in Chap.2.

Eight FRFs are measured from the experimental test rig at rest, and used to feed the above mentioned heuristic code. The new frequency range was chosen to be from 0 to $100Hz$, with constant steps of $0.25Hz$. This range is chosen because crack control tests are performed below the first critical speed ($24.56Hz$) and harmonics up to $3X$ are evaluated.

Table 4.1 summarizes the directions of all the collected FRFs.

Table 4.1: Direction and definition of each FRF collected.

Direction of Excitation	Direction of Response	FRF Name
D_1 vertical	S_{16} vertical	FRF #1
D_2 vertical	S_{16} vertical	FRF #2
D_1 horizontal	S_{16} horizontal	FRF #3
D_2 horizontal	S_{16} horizontal	FRF #4
D_1 vertical	S_{22} vertical	FRF #5
D_2 vertical	S_{22} vertical	FRF #6
D_1 horizontal	S_{22} horizontal	FRF #7
D_2 horizontal	S_{22} horizontal	FRF #8

As in Chap.2, 9 parameters were optimized, namely the stiffness along the vertical and horizontal directions of the first and second bearing $K_{xx_{b1}}, K_{zz_{b1}}, K_{xx_{b2}}$ and $K_{zz_{b2}}$; the modal damping factors of the first four natural modes ξ_1, ξ_2, ξ_3 and ξ_4 and the torsional stiffness, as caused by the existence of the coupling between the shaft and the electric motor $K_{t_{coup}}$.

Table 4.2 presents all the parameters to be optimized as well as their new expected ranges.

Table 4.2: Design space of the optimization problem. k [N/m], ξ [dimensionless] and $k_{t_{coup}}$ [Nm/rad]

	Variables	Design Space	
		Upper Bound	Lower Bound
Bearing 1	$k_{xx_{b1}}$	$5x10^5$	$5x10^6$
	$k_{zz_{b1}}$	$5x10^5$	$1x10^7$
Bearing 2	$k_{xx_{b2}}$	$5x10^7$	$1x10^9$
	$k_{zz_{b2}}$	$5x10^7$	$1x10^9$
Modal Damping	ξ_1	$1x10^{-2}$	$1x10^{-5}$
	ξ_2	$1x10^{-2}$	$1x10^{-5}$
	ξ_3	$1x10^{-2}$	$1x10^{-5}$
	ξ_4	$1x10^{-2}$	$1x10^{-5}$
Torsional Stiffness	$k_{t_{coup}}$	0	$1x10^3$

Again, the optimization is performed 10 times, and each time the optimization process is restarted, a different population is generated. In this way, the solution presenting the smallest fitness function value is expected to reach the global minimum. Table 4.3 presents the result of the 10 optimization processes and their corresponding values of fitness functions.

Table 4.3: Outputs of all the optimization processes: k [N/m], ξ [dimensionless] and $k_{t_{coup}}$ [Nm/rad].

Process	1	2	3	4	5	6	7	**8**	9	10
Fitness	1.5971	1.6102	1.6001	1.6024	1.6002	1.6147	1.6186	**1.5953**	1.5959	1.6017
$k_{xx_{b1}}$	$7.551x10^5$	$8.274x10^5$	$6.848x10^5$	$8.554x10^5$	$5.551x10^5$	$8.237x10^5$	$7.536x10^5$	$\mathbf{8.551x10^5}$	$8.552x10^5$	$7.747x10^5$
$k_{zz_{b1}}$	$3.198x10^7$	$6.197x10^7$	$4.199x10^7$	$5.197x10^7$	$6.248x10^7$	$4.199x10^7$	$6.198x10^7$	$\mathbf{5.203x10^7}$	$5.199x10^6$	$6.209x10^6$
$k_{xx_{b2}}$	$1.559x10^6$	$2.006x10^6$	$3.459x10^6$	$1.896x10^6$	$2.226x10^6$	$9.322x10^5$	$3.392x10^6$	$\mathbf{1.198x10^6}$	1.296^6	$3.271x10^6$
$k_{zz_{b2}}$	$7.697x10^8$	$7.411x10^8$	$4.429x10^8$	$8.521x10^8$	$5.915x10^8$	$6.594x10^8$	$5.451x10^8$	$\mathbf{7.023x10^8}$	$7.157x10^8$	$5.715x10^8$
ξ_1	0.018	0.020	0.005	0.008	0.016	0.028	0.005	**0.009**	0.008	0.014
ξ_2	0.058	0.028	0.157	0.059	0.025	0.164	0.068	**0.099**	0.102	0.247
ξ_3	0.011	0.005	0.024	0.014	0.008	0.003	0.036	**0.009**	0.008	0.004
ξ_4	0.024	0.017	0.055	0.012	0.022	0.087	0.055	**0.030**	0.027	0.014
$k_{t_{coup}}$	738.1	658.9	532.0	895.2	589.4	638.9	501.6	**554.4**	557.5	438.4

The global minimum is the one presented in column 8 of table 4.3. This is the best solution encountered by the optimizer.

In the sequence, the frequency curve adjustment results are presented. These results compare the experimental test rig FRFs and the ones obtained by the numerical optimization code, which considers the optimized parameters.

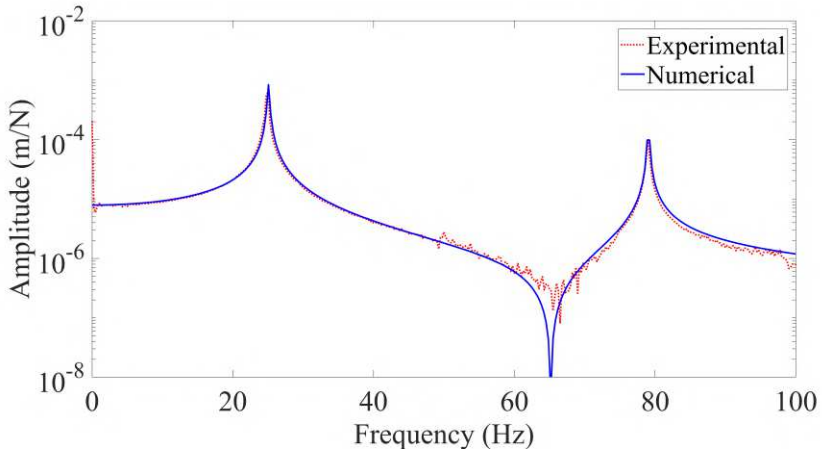

Figure 4.11: FRF$\#1$.

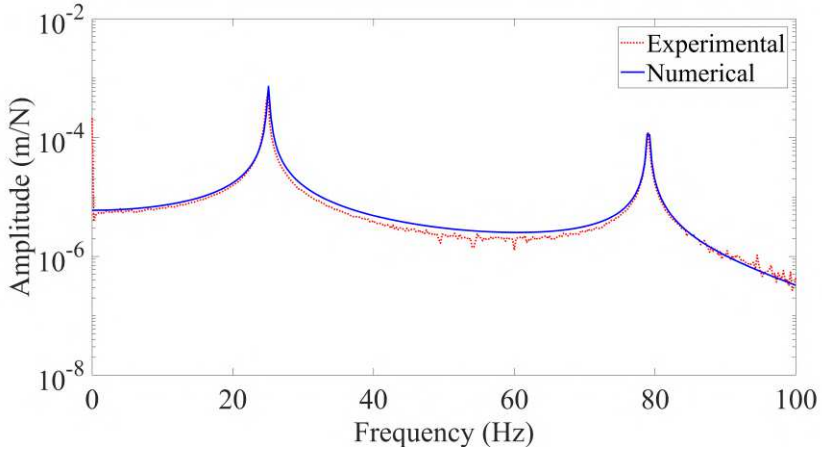

Figure 4.12: FRF$\#2$.

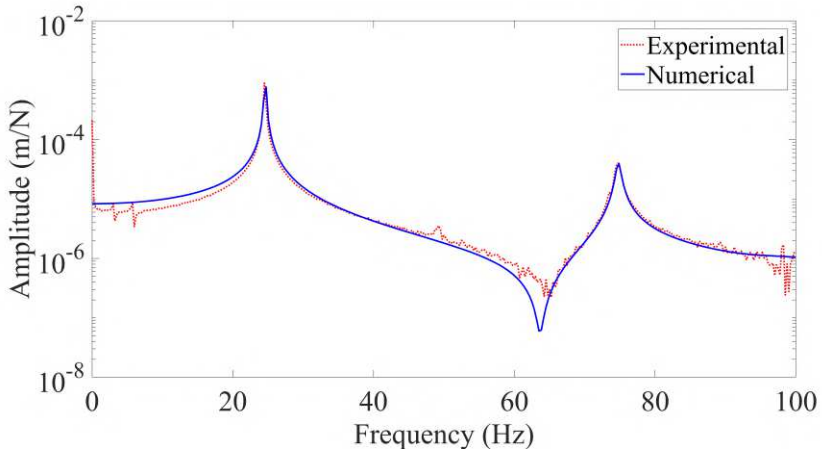

Figure 4.13: FRF$\#3$.

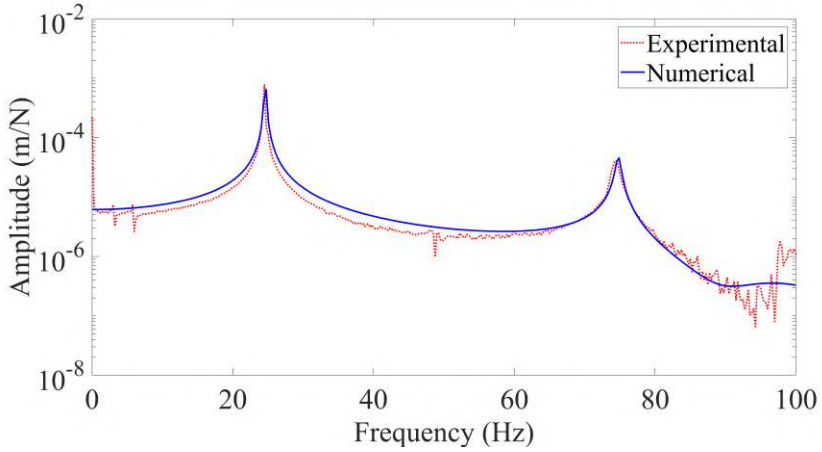

Figure 4.14: FRF$\#4$.

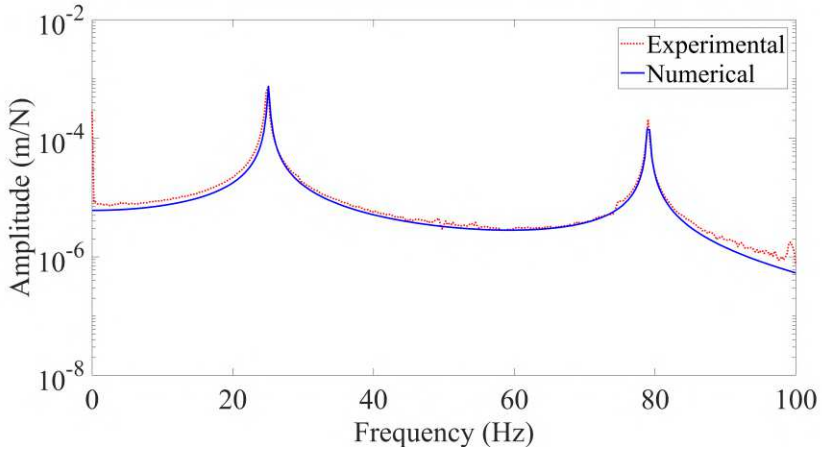

Figure 4.15: FRF$\#5$.

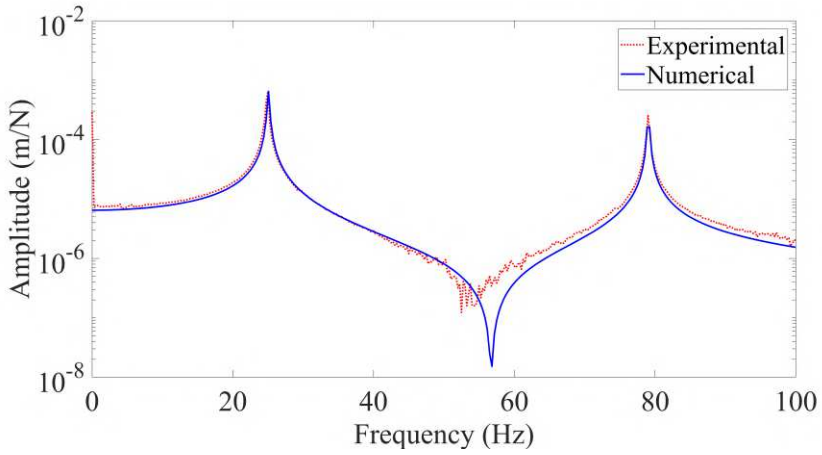

Figure 4.16: FRF#6.

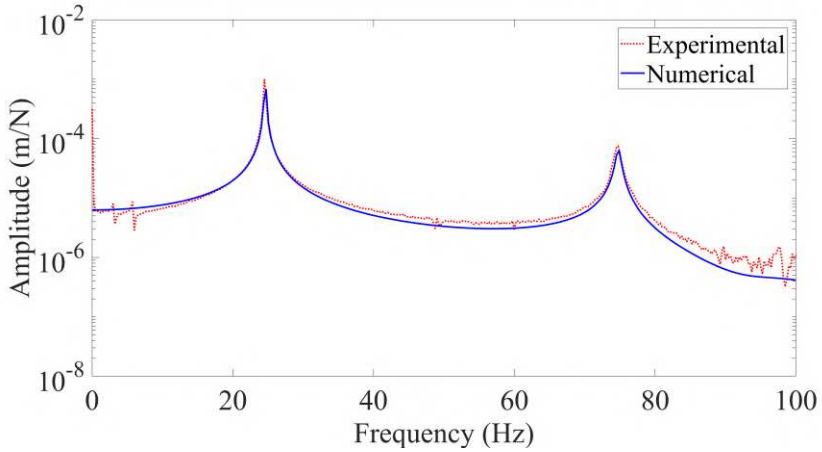

Figure 4.17: FRF#7.

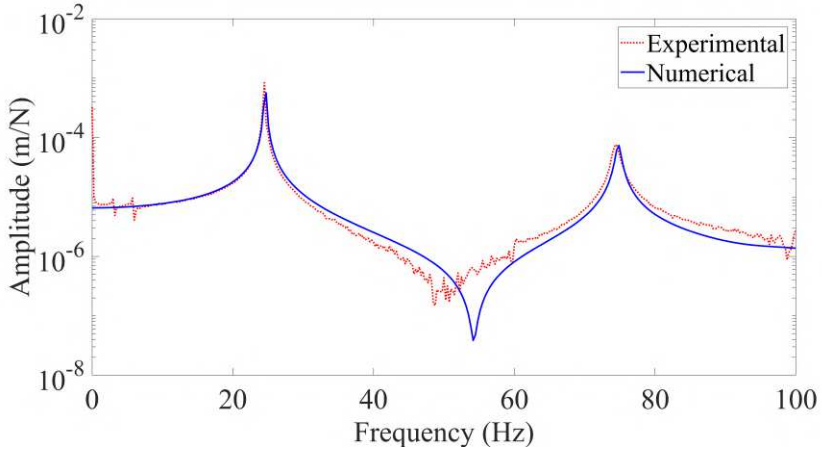

Figure 4.18: FRF#8.

The experimental and numerical curves are well fitted, which validates the numeri-

cal model in the frequency domain, in the range from 0 - $100Hz$, which represents 6000 rev/min (more than the maximum speed of the rotor).

Again, the FRFs of both numerical model and experimental test rig were measured with the shaft at rest. This is acceptable because the gyroscopic effect for the first two natural modes of the rotor is small in the speed range of the motor used in the test rig (4200 rev/min, or 70 Hz).

For understanding the gyroscopic effect influence and how it changes the natural frequencies as the rotor speed increases, Fig. 4.19 presents the Campbell Diagram, collected from the numerical crack control model, which is now validated. The Campbell Diagram is presented from 0 until 5000 rev/min.

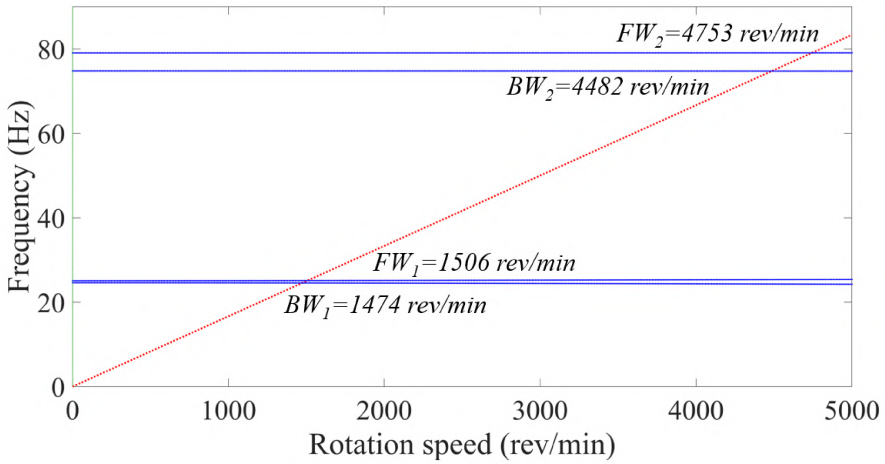

Figure 4.19: Campbell Diagram.

The first 4 critical speeds of the considered rotor are found to be $1,474$ rev/min (24.56 Hz); $1,506$ rev/min (25.10 Hz); $4,482$ rev/min (74.70 Hz) and $4,753$ rev/min (79.22 Hz).

The mode shapes of the test rig are presented in Chap. 6, where a controllability and observability discussion takes place.

4.4.2 Time Domain Updating

Again, the time-domain responses are compared for the numerical model and the experimental test rig. Since this shaft is made of the same material as the one in the first test rig, in Chap.2, the same values of Young modulus and volumetric density were used.

Figure 4.20 presents the lateral vibrations caused by an unbalance of $5.11x10^{-4}$ Kgm, for the rotor operating at $1200\ rev/min$.

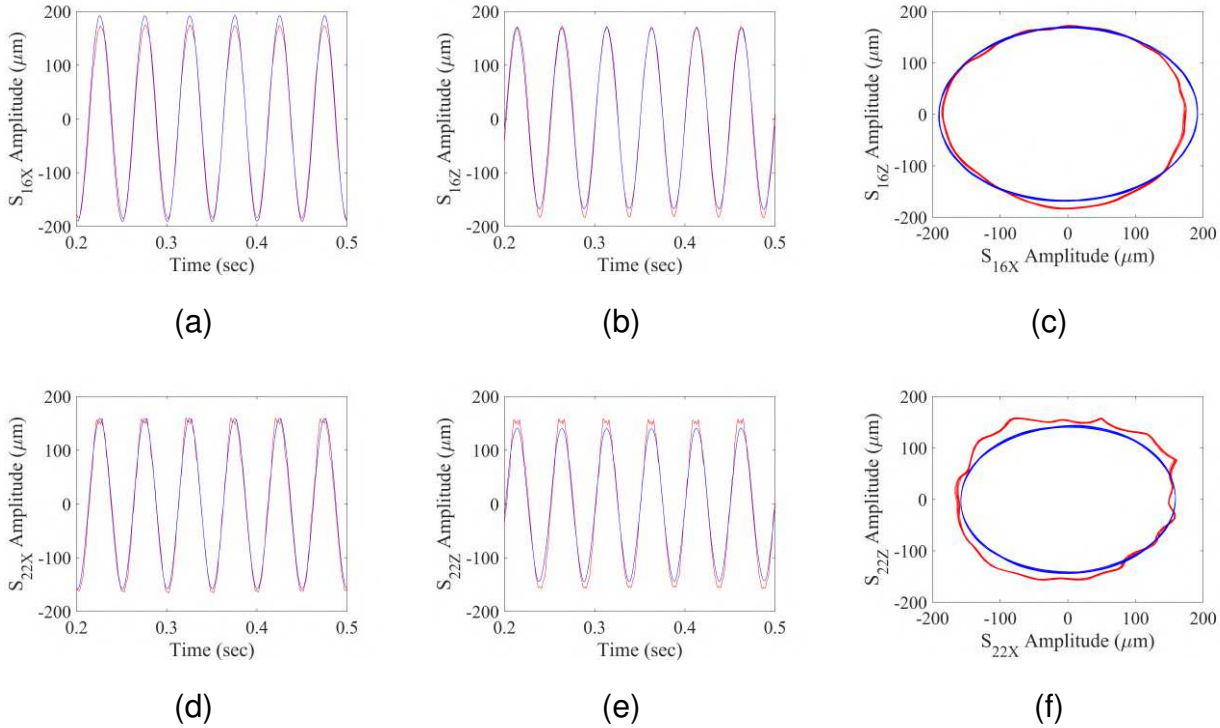

Figure 4.20: Results of model updating for the lateral vibrations in the time domain: (—) Experimental; (—) Numerical: (a) S_{16_x}; (b) S_{16_z}; (c) orbit S_{16_x} Vs. S_{16_z}; (d) S_{22_x}; (e) S_{22_z}; (f) orbit S_{22_x} Vs. S_{22_z};

The time-domain comparison for the numerical FE model and the experimental test rig presents good results.

Moreover, the accuracy of this FE model is crucial for the good quality of the crack control techniques to be tested in the next chapter. Any test is performed first for the numerical model and then on the test rig.

Chapter 5

Electromagnetic Actuators (EMAs)

5.1 Introduction

In the present chapter, a brief background on electromagnetism is exposed, concerning the control action of the EMAs. Each EMA is able to apply only attraction forces, which are modeled in this chapter. These electromagnetic force values depend on the coil geometry, air gap between the coil parts, winding number, and rotor lateral vibrations, which continuously alter air the gap values.

Current amplifiers are necessary to produce the good control currents to act on the EMAs. However, these amplifiers generate important phase delays between control command and control action. For this purpose, a dynamic characterization of the full control system, which includes EMAs, current amplifiers, signal conditioners, and data acquisition system is presented.

This dynamic characterization is performed by including the same behavior of the phase delay in the numerical code. In this way, the same control responses for both the numerical code and the test rig are expected.

5.2 EMA Details

Each EMA is composed basically by a ferromagnetic body, which can be divided in two parts, according to Morais et al. (2013). The first one is the core, which is an (E) shaped body and receives the induction coil. The second one is the so-called target, which is an (I) shaped body, fixed to a roller bearing supporting the shaft, enabling the

active control effort to be applied.

The EMA geometry is summarized in Fig 5.1.

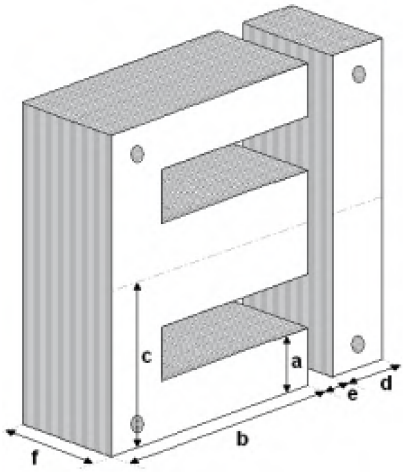

Figure 5.1: EMA geometry.

Table 5.1 presents the physical parameters related to the EMAs used on the hybrid bearing of the rotating machine.

Table 5.1: Values of EMA geometrical parameters.

μ_o	$4\pi 10^{-7}(H/m)$
N	250 windings
a	$9.5mm$
b	$38mm$
c	$28.5mm$
d	$9.5mm$
e	$0.5mm$
f	$20.5mm$

The distance adjustment between the (E) and (I) parts is guaranteed by an insulanting paper sheet. The distance between both parts is called *air gap*, or simply *gap*. In this work, the gap is set to be $500\ \mu m$ for all EMAs, which results in EMA attraction forces up to $150\ N$, making it possible to control the shaft lateral vibrations, according to Koroishi (2013).

Both (E) and (I) parts are composed of sets of insulated ferromagnetic sheets, for

avoiding current losses (Foucault currents). According to Morais et al. (2013), the quality of the ferromagnetic circuit alloy is considered as being high, and the nominal air gap between the stator and the beam is small enough so that the magnetic loss is considered negligible.

The wire used to compose the induction coil of each EMA is a standard cooper wire $AWG24$, such as the one used by Koroishi (2013). This wire characteristics are presented in Tab. 5.2.

Table 5.2: $AWG24$ copper wire features.

Diameter	$0.511\ mm$
Area	$0.205\ mm^2$
Electrical resistance (at $20^o\ C$)	$0.0842\ Ohm/m$
Admissible current	$3.5\ A$

5.3 Brief background on Electromagnetism

According to Serqay and Jewett-Jr. (2008), a coil is a set of electric wire winding, which is capable of producing a fairly uniform magnetic field around its volume, in the presence of an electric current. The electric field uniformity increases as the wire length increases. The ideal coil would present a perfectly uniform magnetic field on its interior while presenting zero values on its outside. The actuation lines of an electromagnetic field present a similar behavior, compared to the actuation lines of a magnetic bar, as depicted in Fig.5.2.

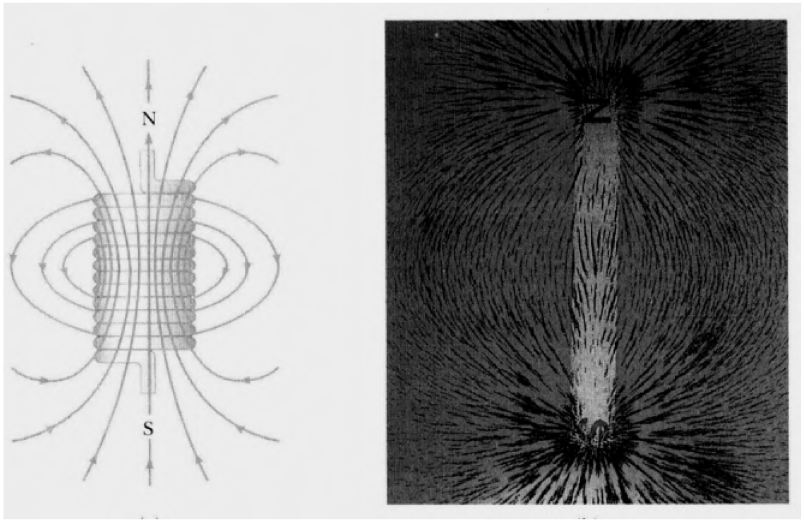

Figure 5.2: Comparison between electromagnetic and magnetic field actuation lines.

Since crack control is performed with the resulting EMA forces, it is important to understand how they are calculated. The magneto-motive force is the first step to be explained, which is obtained by:

$$\Im = NI = \psi\Re \tag{5.1}$$

where N is the number of windings; I is the electrical current in the coil; ψ is the magnetic flux, and $\Re$ is the reluctance of the magnetic circuit.

A parallel between an electric and a magnetic circuit is shown below for illustration purposes. Furtado (2008) presents a comparison between an electric and a magnetic circuit, shown in Fig.5.3.

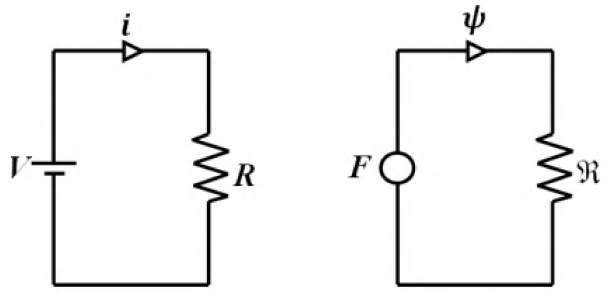

Figure 5.3: (a) Electric circuit; (b) Magnetic circuit.

Table 5.3 presents the concepts necessary for the good understanding of both circuits presented in the figure above.

Table 5.3: Electric and magnetic circuit parameters.

Action	Electric circuit	Magnetic circuit
Motive Force	Electro-motive force F_{em}	Magneto-motive force F_{mm}
Produces	Electric Current $i = \frac{V}{R}$	Magnetic flux $\Psi = \frac{F}{\Re}$
Limited by	Electric resistance R	Magneto reluctance $\Re$

The reluctance in magnetic circuits is analogous to electrical resistance in electrical circuits. It represents an opposition to the magnetic flux and depends on the geometry and on the material composing the magnetic object. An excellent option to reduce the magneto reluctance in a magnetic circuit is to use ferromagnetic materials in the interior of the EMA. Ferromagnetic materials present a high attraction level when submitted to an external magnetic field because they are able to align the magnetic field flux, reducing dispersion losses, Halliday et al. (2007).

There is a different magnetic reluctance, according to the different parts of the ferromagnetic core, as shown in Fig. 5.4.

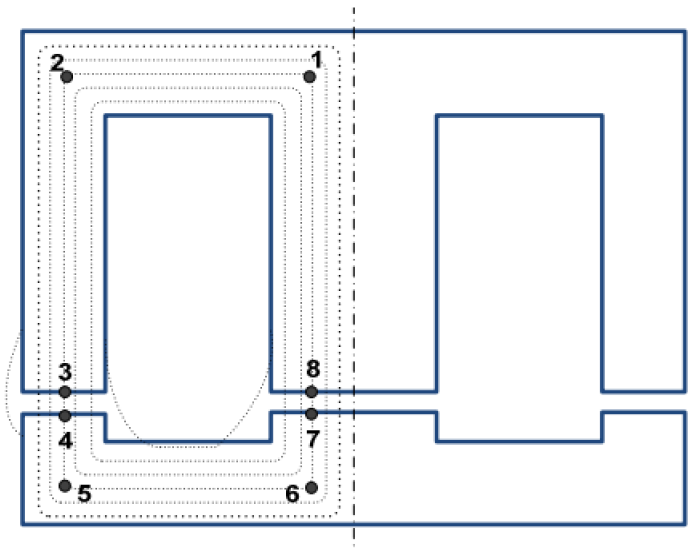

Figure 5.4: Magnetic reluctance, according to each EMA part.

Due to core symmetry, only its left side is presented. The central branch magnetic flux equals to double of each lateral branch flux. This way, the magnetic reluctance on

each part of the core needs to be calculated, as follows.

$$\begin{aligned}
\Re_{8-1} = \Re_{2-3} &= \frac{b-\frac{a}{2}}{\mu_r \mu_o a f} \\
\Re_{1-2} = \Re_{5-6} &= \frac{c-a}{\mu_r \mu_o a f} \\
\Re_{3-4} = \Re_{7-8} &= \frac{e}{\mu_o a f} \\
\Re_{4-5} = \Re_{6-7} &= \frac{d-\frac{a}{2}}{\mu_r \mu_o a f}
\end{aligned} \tag{5.2}$$

where a, b, c, d, e, f are geometric parameters, as presented in Fig.5.1; μ_o is the vacuum magnetic permeability (constant, as shown in Tab. 5.1); μ_r is the relative magnetic permeability of each EMA. It can be obtained by an optimization process, as done by Koroishi (2013). Since the EMAs used in this Ph.D. dissertation are the same as those used in the above cited reference, the same values of relative magnetic permeability are considered. For the interested reader, details about the optimization problem are described in the reference.

The magnetic flux present on each lateral branch can now be obtained as:

$$\frac{\psi}{2} = \frac{NI}{\sum_{i=1}^{8} \Re_i} = \frac{NI\mu_o \alpha f}{2e + \frac{2b+2c+2d-4a}{\mu_r}} \tag{5.3}$$

The total magnetic flux, induced in the N windings is written as:

$$\Psi = N\psi = LI \tag{5.4}$$

where L is the magnetic inductance.

Substituting Eq. 5.3 into Eq. 5.4, the EMA magnetic inductance is obtained:

$$L = \frac{N^2 \mu_o \alpha f}{e + \frac{b+c+d-2\alpha}{\mu_r}} \tag{5.5}$$

where $\alpha = 2a$ represents the width of the central branch.

Then, the electromagnetic attraction force, produced among two ferromagnetic materials is derived as follows:

$$F_{ema} = \frac{\partial W_{mag}}{\partial x_m} \tag{5.6}$$

where W_{mag} is the magnetic energy, which is calculated as:

$$W_{mag} = \int_{0,0,...,0}^{i_i,i_2,...,i_n} \sum_{k=1}^{n} \psi_k(i_1, i_2, ..., i_n, x_m) di_k \tag{5.7}$$

The magnetic energy can also be calculated in terms of the total magnetic flux:

$$W_{mag} = \int_0^I \Psi di_k = \frac{1}{2} L I^2 \tag{5.8}$$

Finally, the magnetic attraction force is calculated as:

$$F_{ema} = \int_0^I \Psi di_k = \frac{N^2 I^2 \mu_o a f}{2((e \pm \delta) + \frac{b+c+d-2a}{\mu_r})^2} \tag{5.9}$$

where δ stands for the shaft vibration, which continuously alters the gap value.

Equation (5.9) is applied to the Eq. (4.1) for performing crack control, by using the control forces provided by the EMAs.

The EMAs control currents are applied in a sinusoidal form but presenting no negative part. Each sinus wave half part is applied by a certain EMA in a synchronous way, according to Fig.5.5(b). Other types of control currents can be applied to the EMAs, however this procedure was chosen since there is no need to use bias currents, which would make the temperature of the actuators to increase significantly.

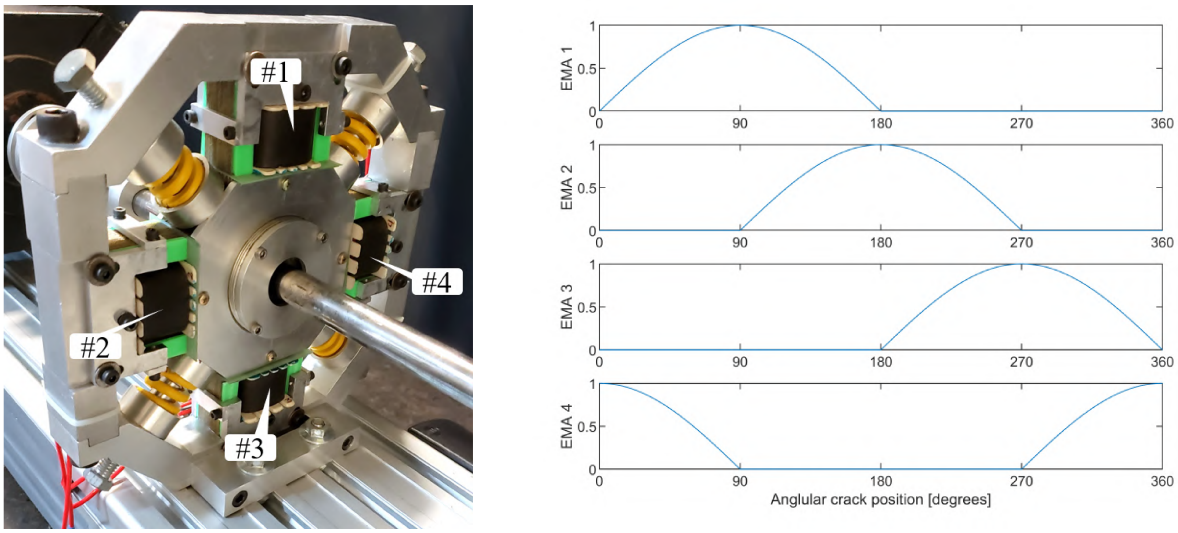

(a) (b)

Figure 5.5: (a) Hybrid bearing, showing the number of each EMA; (b) Synchronized hybrid bearing actuation ($Ampres$), among its four EMAs, with no bias current.

5.4 Dynamic Characterization of the EMAs

Once the electromagnetic force is known, it is important to understand experimentally how the EMA, as well as its full control system behaves along the frequency. For this reason, an experiment was conducted, to determine the dynamic behavior of the system, as presented by Fig.5.6.

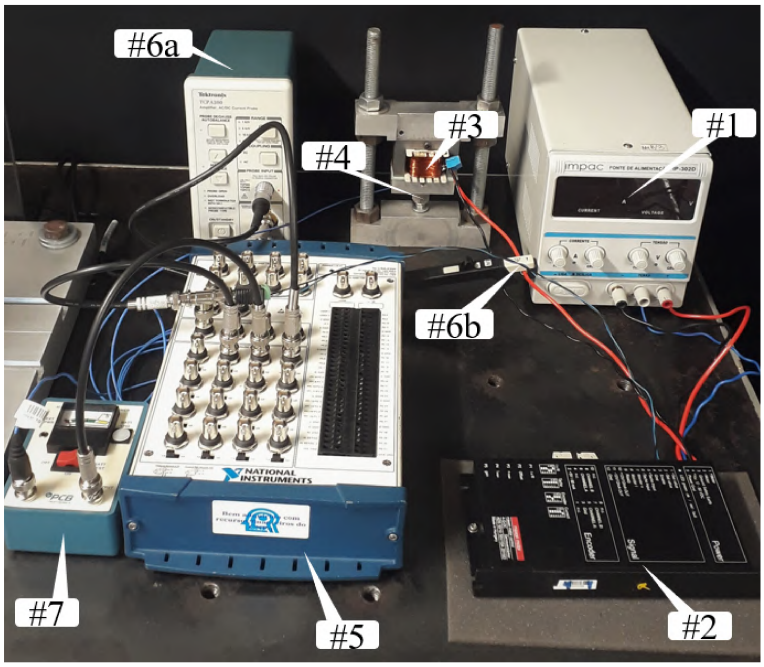

Figure 5.6: Experiment layout for the EMA dynamic characterization.

The following equipments were used in this experiment:

1. External source, (impac®, model $IP-302D$);
2. Servo amplifier (Maxon®, $ADS50/10201583$);
3. Electro-magnetic actuator (EMA);
4. Force transducer (PCB Piezotronics®, model $208C03$);
5. Acquisition board (National Instruments®, model $NIUSB-6259$);
6. Current measurement system (Tektronix®, model $TCPA300$);
7. Signal conditioner (PCB Piezotronics®, model $480C02$).

The external source is used to feed the current amplifier, which receives a sinusoidal voltage signal from the acquisition board; then, this signal is converted to a sinusoidal current signal that passes through the EMA.

The attraction force produced by the EMA is measured by the force transducer. The objective is to verify phase delays between the voltage command (applied by the acquisition board) and the actuation force (measured by the force transducer). This is important for two reasons: 1) for modeling the behavior of the full control system so that the numerical code generates results similar to the experimental crack control test rig (phase correction); 2) for guaranteeing similar force amplitudes along the used frequency range (force amplitude correction).

Figure 5.8 presents the Bode Diagram of the full control system, for a sine wave generated with $1.5\ volt$ of amplitude and $3.0\ volts$ of bias. Other values of amplitude and bias were tested, but similar behavior was observed. Also, it is worth mentioning that this same characterization was performed for each of the four EMAs used in the test rig. However, since the results are quite similar, only the results corresponding to one of the EMAs is presented.

For Fig.5.8, the voltage signal produced by the acquisition board is considered as input; as output, the mechanical force signal read by the force transducer is considered. Both signals are converted to the frequency domain by using the so-called Discrete Fast Fourier Transform (DFFT). Then, the Bode Diagram is built considering the corresponding Frequency Response Function (FRF).

A block diagram scheme is presented in Fig. 5.7 to give a better understanding of the Bode diagrams to be shown in Fig. 5.8, 5.9 and 5.10.

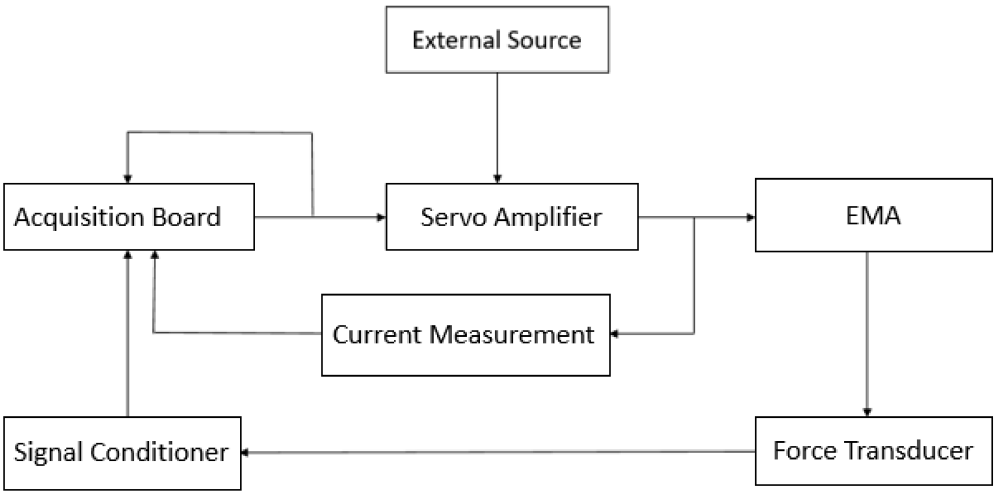

Figure 5.7: Bode diagram: acquisition board and force transducer.

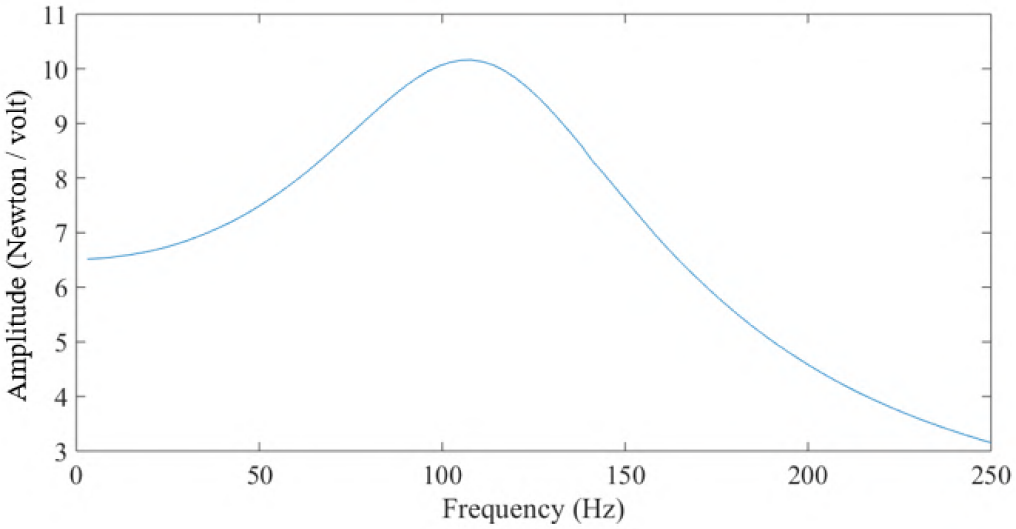

(a)

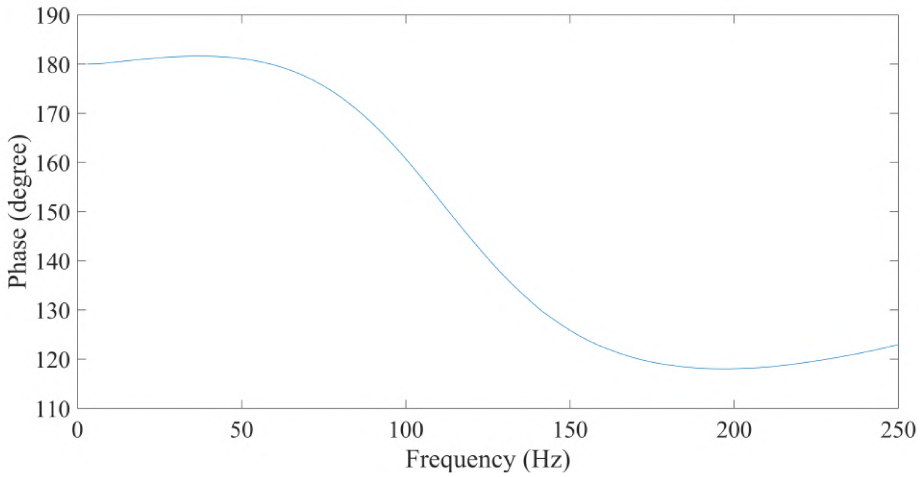

(b)

Figure 5.8: Bode diagram: acquisition board and force transducer.

According to Fig.5.8, a phase delay of $62\ degrees$ is noticed until $200\ Hz$. Also, there is an important force amplitude variation as the frequency increases.

Other Bode diagrams are built until the critical component responsible for the major delay values is determined. Figure 5.9 presents the Bode diagram for the EMA input and output. Through this figure, it becomes clear that that EMA is responsible for only $4\ degrees$ of phase delay.

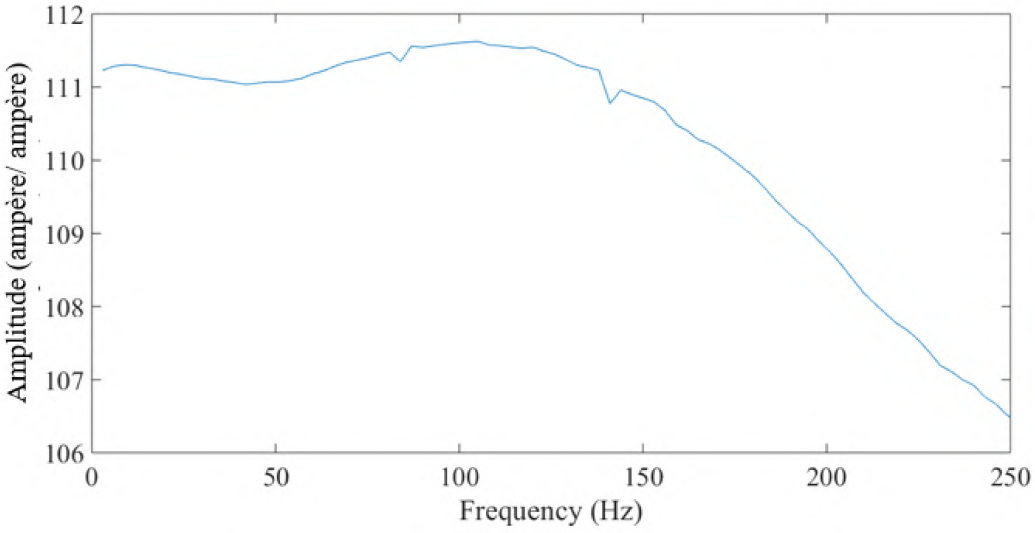

(a)

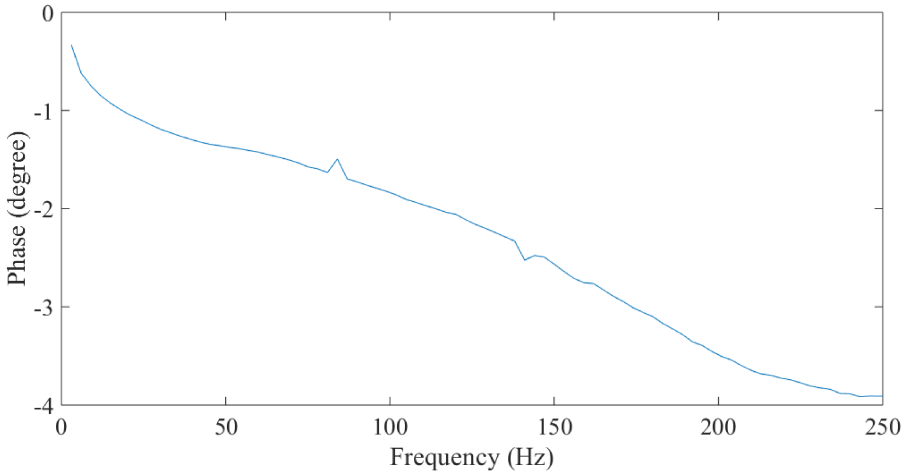

(b)

Figure 5.9: Bode diagram: the EMA input and output.

Finally, a Bode diagram is determined for the acquisition board output and the EMA input (which isolates the current amplifier), as shown by Fig.5.10.

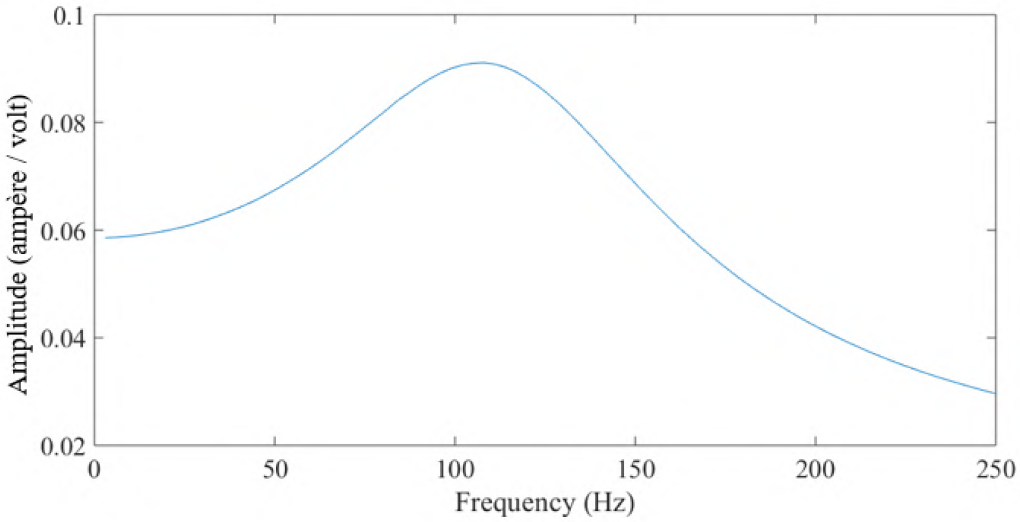

(a)

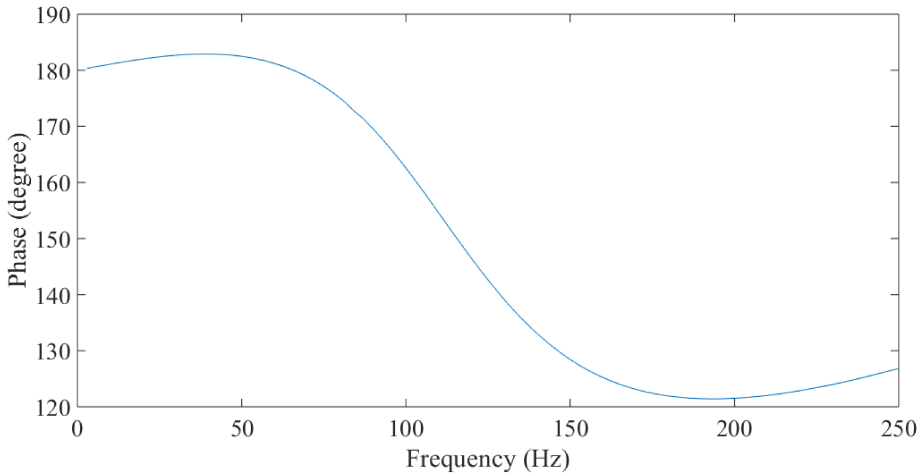

(b)

Figure 5.10: Bode diagram: current amplifier input and output.

It can be concluded that the current amplifier is responsible for $58\ degrees$ of phase delay, until $200Hz$. The behavior of both force amplitude and phase delay have to be taken into account on the numerical code; consequently, the control responses of both the numerical model and experimental test rig are expected to be similar.

This can be done by adding a Transfer Function (TF) on the numerical code, that presents the same behavior of the control system. The corresponding procedure is presented in the following chapter.

Chapter 6

Crack Control in Rotating Machinery by the use of the PID technique

6.1 Introduction

In this chapter, some background on control theory, applied to this Ph.D. dissertation is presented. Also, a discussion about controllability and observability is addressed. Moreover, the open-loop and the closed-loop plants are presented.

The Proportional-Integrative-Derivative (PID) controller is also presented. Besides, details are given regarding the determination of the control currents as based on the lateral vibrations of the rotor.

After that, some details about the PID design are furnished, and two control laws are proposed and compared, concerning crack control efficiency.

The first control law considers the control currents based on the shaft vibration signal. The second control law is derived by applying a bandpass filter in the $2X$ and $3X$ super-harmonics frequency range. This is done for concentrating the control action over the crack signatures.

Finally, the results of both control laws are compared in the last section of this chapter, and some comments are made.

6.2 Controllability and Observability

According to Gajic and Lelic (1996), the concepts of controllability and observability were introduced by Kalman (1960) and represent two major concepts of modern control system theory. Concerning these concepts, a given dynamic system can be classified as follows: only observable, both controllable and observable, only controllable or none, according to Fig. 6.1.

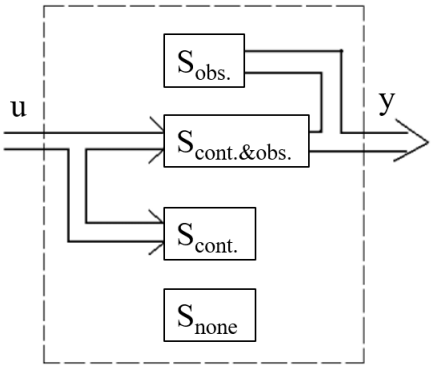

Figure 6.1: System classification; extracted from Koroishi (2013).

6.2.1 Mathematical framework for controllability and observability

For understanding these concepts, the system represented by the space state representation is now considered (as presented in section 3.2). A solvable system of linear algebraic equations has a solution if and only if the system matrix rank is full. In this case, the observability and controllability tests are performed over the numerical model of the test rig, as based on rank tests on both controllability and observability matrices.

Mathematically, according to Meirovitch (1990), a linear time-invariant (LTI) discrete system can be called *completely observable* if every initial state $\mathbf{x}(t_o)$ is determined from the output measurements $\mathbf{y}(t)$, during a finite time interval $t_o \leq t \leq t_f$. According to Koroishi (2013), this definition indicates that all state variables $\mathbf{x}(t)$ have influence on the responses $\mathbf{y}(t)$.

The observability matrix of a given dynamic system is composed by:

$$\mathbf{M}_o = \begin{bmatrix} \mathbf{C} \\ \mathbf{CA} \\ \vdots \\ \mathbf{CA}^{2n-1} \end{bmatrix} \tag{6.1}$$

where n is the number of state variables of the system.

In this way, in order to the system to be called observable, Eq.(6.2) needs to hold.

$$rank(\mathbf{M}_o) = 2n \tag{6.2}$$

Regarding the numerical model of the rotating machine considered in this research work, Eq.(6.2) holds, consequently this system is called observable.

Analogously, a LTI discrete system is called *completely controllable* if it is possible to modify the initial state $\mathbf{x}(t_o)$ to any final state $\mathbf{x}(t)$, during any time period in a finite time interval $t_o \leq t \leq t_f$, according to Meirovitch (1990).

The controllability of a system is determined by the rank analysis of the controllability matrix:

$$\mathbf{M}_c = \begin{bmatrix} \mathbf{B} & \mathbf{AB} & \cdots & \mathbf{A}^{2n-1}\mathbf{B} \end{bmatrix} \tag{6.3}$$

Analogously, in order to the system to be called controllable, Eq.(6.4) needs to hold.

$$rank(\mathbf{M}_c) = 2n \tag{6.4}$$

Again, for the rotating machine considered in the present dissertation, Eq.(6.4) holds, consequently this system is also called controllable.

6.2.2 Physical representation of controllability and observability

Another way to check system controllability and observability is by plotting the mode shapes of the rotating machine. Therefore, by the sensors and actuators position, relative to the nodes of the system mode shapes, the controllability, and observability of the system are verified.

For this purpose, Fig. 6.2 is presented.

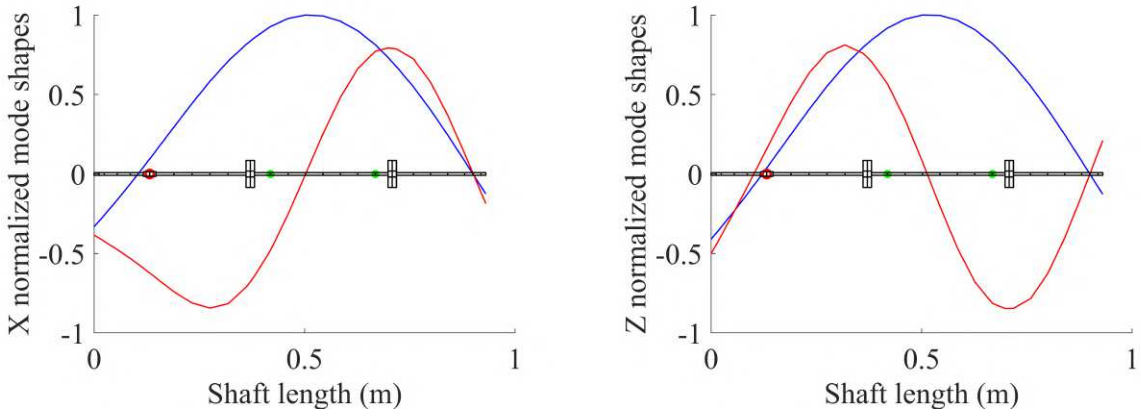

(a) (b)

Figure 6.2: Normalized mode shapes along the X and Z direction: (a) (—) first; (—) third; (b) (—) second; (—) fourth. Sensor positions are marked as * and the electromagnetic actuator position is marked as o.

Physically, the dynamic system is called observable if there is an offset between the nodes of the mode shapes and the position of the sensors. In this way, by Fig. 6.2, it is noticed that this system is observable.

Moreover, the dynamic system is called controllable if there is an offset between the nodes of the mode shapes and the position of the system actuators. So, by the analysis of Fig. 6.2, it is observed that the system is also controllable.

6.3 The Open-loop System

The rotating machine used to obtain the results presented in this chapter was previously described in Chap.4. Figure 6.3 depicts the scheme of the open-loop system for this rotating machine. It is worth mentioning that the open-loop system contains not only the rotor but also its current amplifier, which imposes an important phase delay, the EMAs, and the sensors. In this way, the transfer function of each component is considered and combined with the others. The command *series* in Matlab® was used for this purpose.

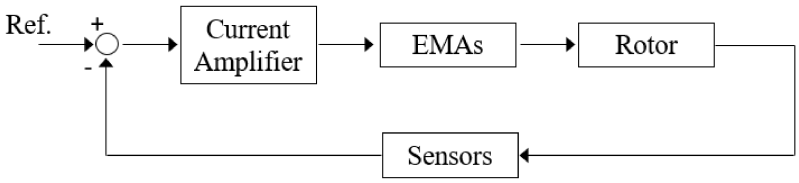

Figure 6.3: Open-loop plant.

6.4 The Closed-loop System

The closed-loop system is obtained by adding the controller before the open-loop plant, as depicted by Fig. 6.4. The controller is capable of altering the position of poles and zeros in the complex plane, thus modifying the behavior of the dynamic system. In this dissertation, the controller used is a PID, which is detailed in the next section. The closed-loop plant root locus representation is presented in the sequence.

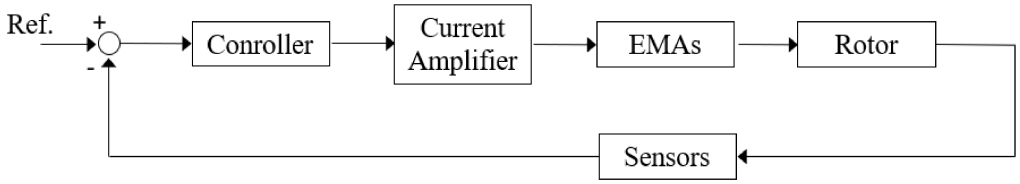

Figure 6.4: Closed-loop plant.

6.5 The PID Controller

According to Borges (2016), the PID technique is the most used for control application in the industry due to its efficiency and simplicity. For this reason, this was the type of controller chosen for this research work. Equation (6.5) presents the parallel continuous PID control expression:

$$PID = \frac{K_D s^2 + K_P s + K_I}{s} \tag{6.5}$$

where K_D represents the derivative gain, K_P is the proportional gain, and K_I is the integral gain.

Generally, the proportional gain affects mainly the system stiffness, since it multiplies the shaft displacements. Besides, the derivative gain affects mainly the system

damping, since it multiplies the shaft velocities. Finally, the integral gain is devoted to suppressing the steady-state error, making the output to reach exactly the desired set point.

Concerning the PID proportional gain, K_P, it was noticed that it assumes negative values. This is due to the fact that the rotating machine considered presents an inverse proportional gain relation. It means that the sense of the actuators force (input) on the shaft is contrary to the sense of the shaft displacement measurement (output).

Concerning the PID integral gain, K_I, it is was observed that this gain has no influence on the system behavior, consequently it is set to zero.

Finally, the derivative gain, K_D, representing the additional damping that the controller adds to the system was found to be necessary, following the tests performed previously.

In this way, a PD controller is applied to the rotating machine devoted to crack control. This machine was previously presented in Chap. 4. The controller is applied to the hybrid bearing, as shown by Fig. 6.5. The inputs of the PD controller are the lateral vibrations measured at node $\#16$ by the probes S_{16_X} and S_{16_Z}. Moreover, the PD outputs are the control currents feeding each EMA. Probe S_{16_X} is considered as a reference for deriving the control currents applied to $EMA\#2$ and $EMA\#4$, while S_{16_Z} is used to generate $EMA\#1$ and $EMA\#3$ control currents.

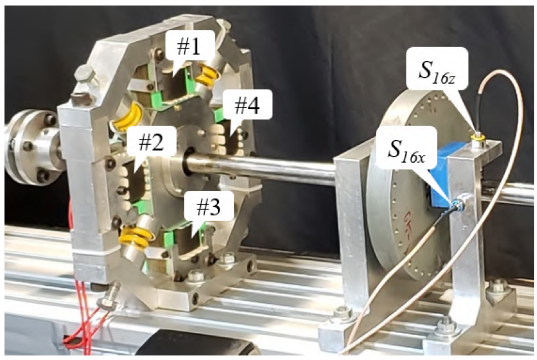

Figure 6.5: Hybrid bearing with its four EMAs.

In this application, the control currents present a sinusoidal behavior. Along the horizontal direction, a half-sine wave is sent to $EMA\#2$, and the other half-sine is sent to $EMA\#4$, with a phase delay of 180 degrees. Since they are opposite signals, the sine wave is complete. The same procedure is applied to the vertical direction, concerning $EMA\#1$ and $EMA\#3$.

This is done by using the logic represented by the scheme of Fig. 6.6.

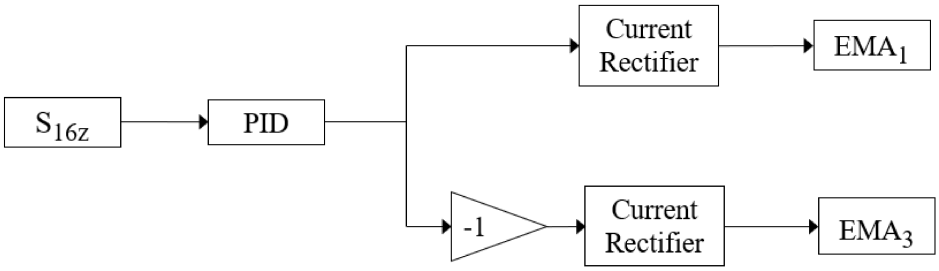

Figure 6.6: Logic for producing the control currents, based on the shaft lateral vibrations.

By deriving the control currents in the way presented by Fig. 6.6, the control currents show the behavior depicted by Fig. 6.7, corresponding to numerical simulation. Control currents in the form of half sinusoidal waves are applied to $EMA\#1$ and $EMA\#3$, as based on the S_{16_Z} signal.

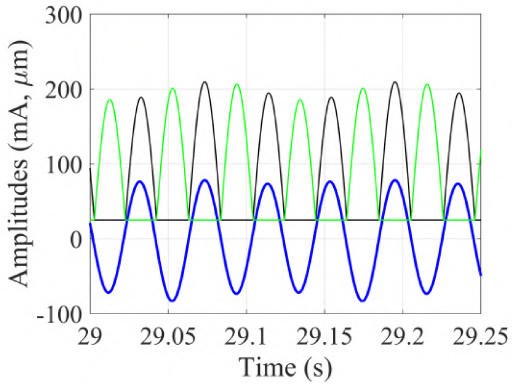

Figure 6.7: Control currents (mA) and shaft lateral vibrations (μm). (—) Controlled S_{16_Z}, (—) EMA$\#1$, and (—) EMA$\#3$.

Figure 6.7 serves as an example for showing how the control currents are derived, based on the shaft displacement signals. This figure shows only the vertical currents; the horizontal ones follow the same principle, having S_{16_X} signals commanding EMA$\#2$ and EMA$\#4$.

The control currents were designed so that bias currents are avoided, which could cause the actuators to overheat. Even though, a small amount of bias current was considered ($50\ mA$) for keeping the EMA core energized, providing a faster actuation. This bias value was obtained experimentally in the laboratory, and it was considered for

all numerical and experimental tests. This value was found to be small enough for not increasing the EMAs temperature and high enough for keeping them energized during operation.

6.6 Design of the PD Control Laws

Two different control laws are applied, aiming at obtaining the best PD control action, namely:

1. PD without filter;
2. PD with a bandpass filter for $2X$ and $3X$ frequencies (crack signatures).

The first control law, based on the PID without filter produces currents with the same harmonic information of the displacement sensors. On the other hand, the second control law, based on the PID with a bandpass filter produces currents containing only the $2X$ and $3X$ information from the displacement signal.

A bandpass filter, producing control currents with only $2X$ and $3X$ information was designed to focus on the control action regarding the crack signatures. This procedure decreases the breathing mechanism, which is responsible for accelerating crack propagation.

Both control laws are compared for three different operation speeds:

1. $\Omega = \Omega_{crit}/3 = 493\ rev/min$;
2. $\Omega = \Omega_{crit}/2 = 737\ rev/min$;
3. $\Omega = \Omega_{oper} = 900\ rev/min$.

The first and second speeds were chosen for highlighting $3X$ and $2X$ super-harmonics, respectively. The third speed was considered for making the control action more difficult since the super-harmonic levels for this speed are much lower as compared with the two other rotation speeds considered, i.e., it is not related to the critical speeds..

Finally, it is important to describe how the PD proportional and derivative gains are obtained. The PD used in this dissertation is not robust. It is applied only for the three mentioned speeds (for the steady-state condition). For each speed, the gain and

phase margins are observed for calculating the possible values of K_P and K_D, so that the system does not become unstable.

For this purpose, a white noise signal was applied to each EMA separately, while the machine was operating at each of the mentioned constant speeds (493 rev/min, 737 rev/min, and 900 rev/min). Moreover, the displacement signals at node $\#16$ were measured (S_{16_X}, and S_{16_Z}).

In this way, the open-loop transfer function representing the real rotating machine to be controlled is defined. After that, a PID controller was numerically applied to the corresponding open-loop transfer function, and different K_P and K_D gains were tentatively applied for checking gain and phase margins of the system.

Figure 6.8(a) presents the Root Locus of the open-loop transfer function for the rotor operating at 900 rev/min (remember it is an inverse gain plant). Then, a numerical PID controller without filter is applied to this transfer function, generating a closed-loop plant, which is depicted by Fig. 6.8(b).

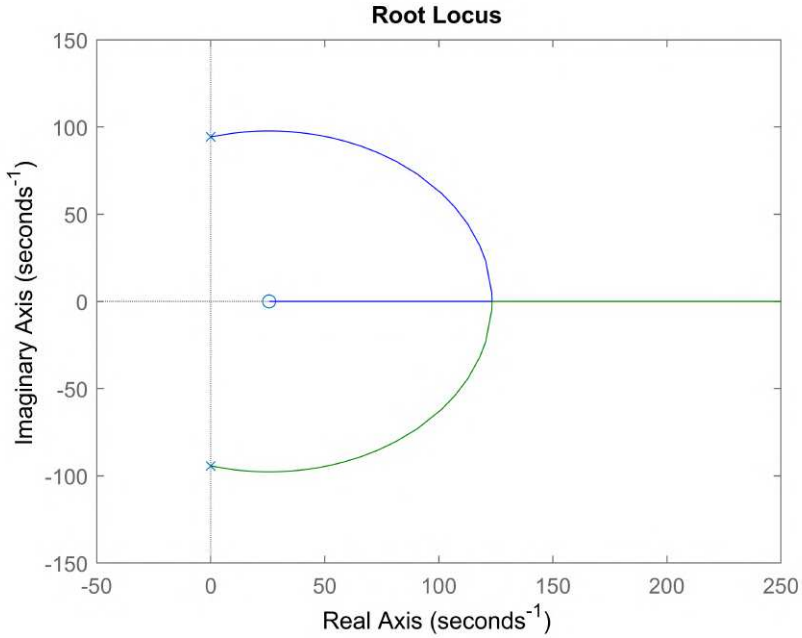

(a)

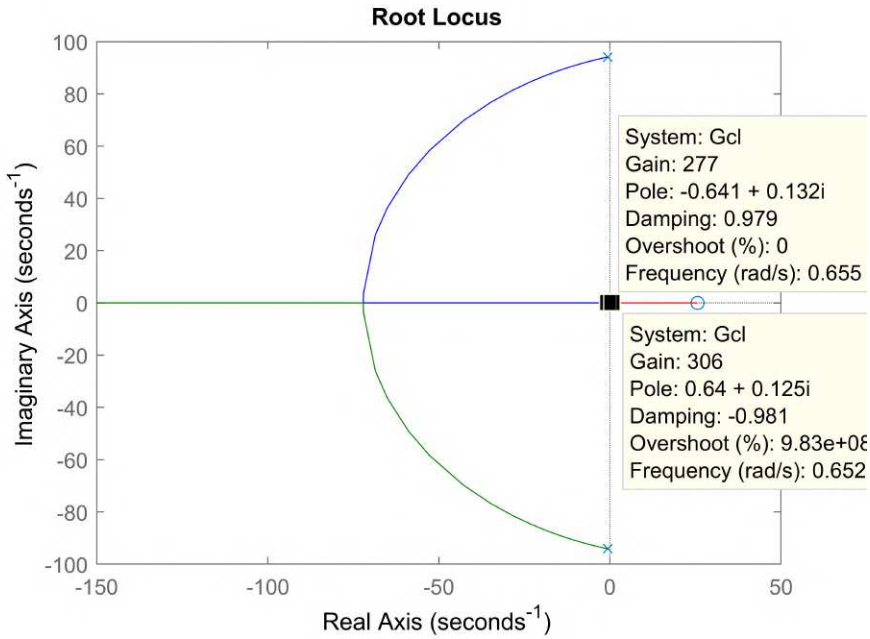

(b)

Figure 6.8: Root Locus: (a) Open-loop plant, and (b) Closed-loop plant.

The transition stable-unstable occurs around a gain of 300. In this way, one expects to be able to increase the PID proportional gain K_P to about 200, before the system becomes unstable.

This procedure was applied for having an initial idea of the values to be assigned

to the PID gains. Fig. 6.8 depicts only the case of 900 rev/min for a PID without filter. The same Root Locus study was performed for the three rotating speeds, for both PID control laws.

6.7 PID Control: Numerical and Experimental Results

The results of the PID active controller are presented in this section for both numerical and experimental applications. The numerical results are derived from the model presented in Chap. 4. Moreover, the experimental results stem from the test rig also presented in Chap. 4. Both responses are compared and discussed.

All the results presented consider an unbalance value of $4.26 \times 10^{-}4\ Kgm/-90^{o}$ applied to the disc D_1.

6.7.1 Results of the PID without Filter

a) Speed: $\boldsymbol{\Omega = \Omega_{crit}/3}$

In this case, the best PID gains are presented in Tab. 6.1.

Table 6.1: PID gains for 493 rev/min, PID without filter.

	K_P	K_I	K_D
Numerical PID	-100	0	40
Experimental PID	-180	0	0.8

Regarding the numerical FE model, the only fault considered was the transverse crack. For this reason, at the speed $\Omega = \Omega_{crit}/3$, it is expected from numerical simulation that the numerical orbit presents three loops, as depicted by Fig. 6.9(c). The numerical control action was able to decrease the shaft lateral vibrations, as expected.

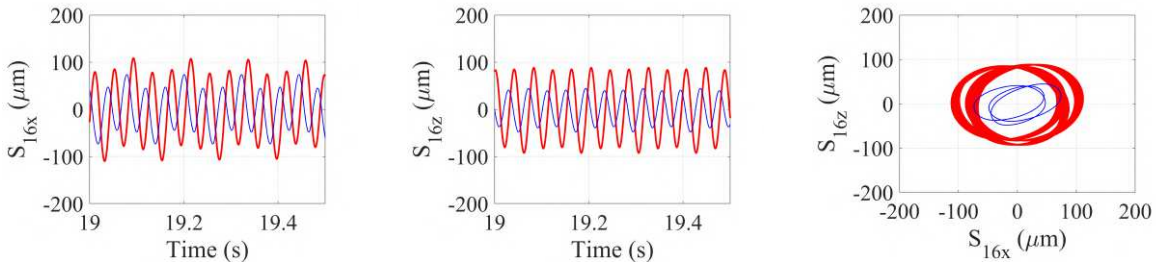

(a) (b) (c)

Figure 6.9: $493\ rev/min$, PID without Filter. Numerical time domain shaft lateral vibrations, in μm: (—) Control OFF, and (—) Control ON. (a) S_{16_X}; (b) S_{16_Z}; (c) orbit S_{16_X} x S_{16_Z}.

Concerning the numerical frequency response function, Fig. 6.10 indicates that the controller was able to decrease the rotor amplitudes of vibration, especially in the vertical direction. Notice that the $3X$ frequency is the most damped one since the PID presents no filter and generates control currents similar to the displacement signal (which has a significant $3X$ amplitude at one-third of the rotor first critical speed).

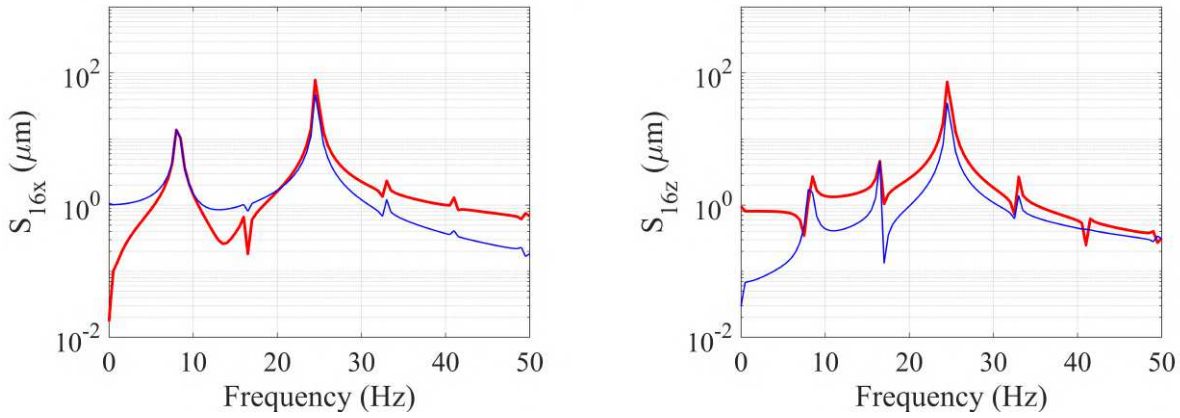

(a) (b)

Figure 6.10: $493\ rev/min$, PID without Filter. Numerical frequency domain shaft lateral vibrations, in μm: (—) Control OFF, and (—) Control ON. (a) S_{16_X}; (b) S_{16_Z}.

Figure 6.11 presents the numerical simulations for the control currents, based on the shaft displacements. The control currents required are quite small, being around $200\ mA$ along the horizontal direction and $500\ mA$ along the vertical direction.

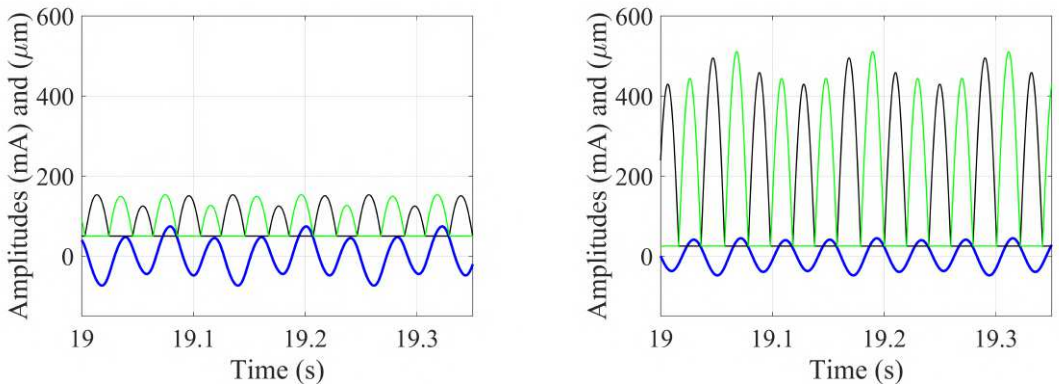

Figure 6.11: $493\ rev/min$, PID without filter. Numerical simulation for control currents, in mA and shaft lateral vibrations, in μm. (a) (—) Controlled S_{16_X}, (—) EMA$\#2$, and (—) EMA$\#4$; (b) (—) Controlled S_{16_Z}, (—) EMA$\#1$, and (—) EMA$\#3$.

Figure 6.12 presents the experimental time responses. The uncontrolled orbits (red curve) present magnitudes, that are close to the numerical ones. However, the orbits do not present three inner loops, as the numerical ones, since its $3X$ super-harmonics present much less energy than in the numerical case. It is possible that the crack found in the test rig was not produced in the most interesting angular position for favouring the super-harmonics.

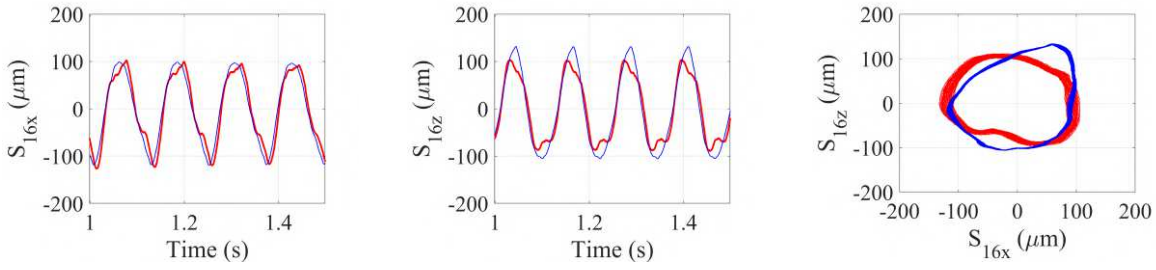

Figure 6.12: $493\ rev/min$, PID without Filter. Time domain shaft lateral vibrations, in μm: (—) Control OFF, and (—) Control ON. (a) S_{16_X}; (b) S_{16_Z}; (c) orbit $S_{16_X}\ x\ S_{16_Z}$.

Figure 6.13) presents the experimental frequency response function. Notice that, although the $3X$ super-harmonics are less energetic than the numerical ones, they are quite significant. Concerning the control efficiency, the frequency response function

presented the same tendency as compared with the numerically simulated one, being more efficient in the vertical direction.

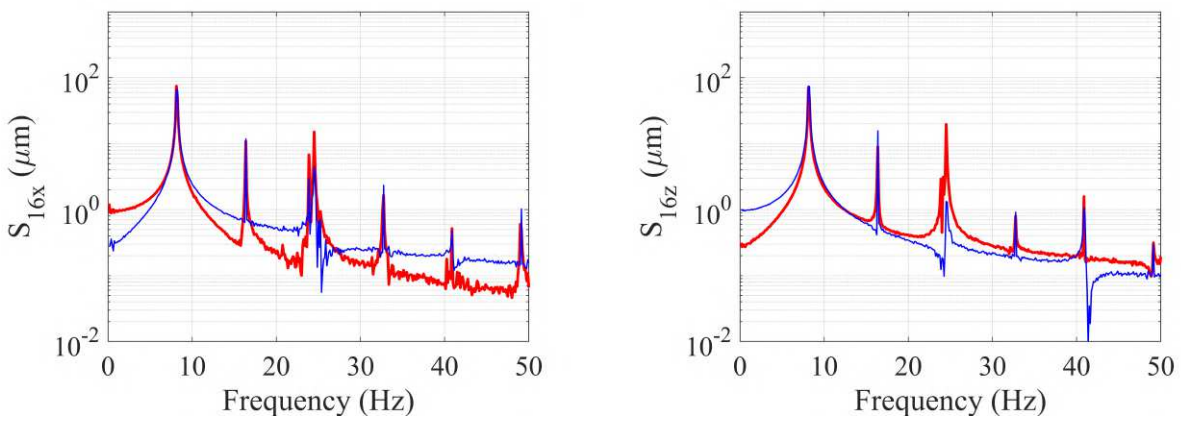

(a) (b)

Figure 6.13: $493\ rev/min$, PID without Filter. Frequency domain shaft lateral vibrations, in μm: (—) Control OFF, and (—) Control ON. (a) S_{16_X}; (b) S_{16_Z}.

Figure 6.14 depicts the control currents measured directly from the test rig. They are higher than the estimated numerical currents, but still not so different.

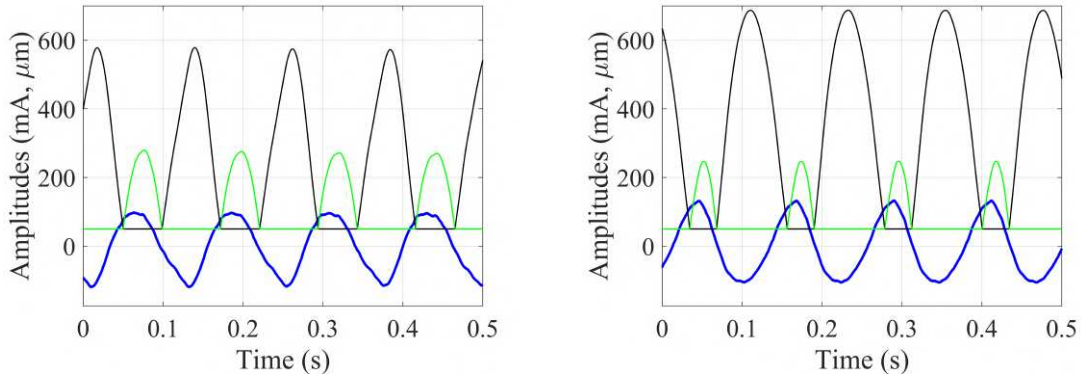

(a) (b)

Figure 6.14: $493\ rev/min$, PID without filter. Control currents, in mA and shaft lateral vibrations, in μm. (a) (—) Controlled S_{16_X}, (—) EMA$\#2$, and (—) EMA$\#4$; (b) (—) Controlled S_{16_Z}, (—) EMA$\#1$, and (—) EMA$\#3$.

b) Speed: $\boldsymbol{\Omega = \Omega_{crit}/2}$

In this case, the PID gains are presented in Tab. 6.2.

Table 6.2: PID gains for $737\ rev/min$ and PID without filter.

	K_P	K_I	K_D
Numerical PID	-200	0	80
Experimental PID	-200	0	1

The cracked numerical model is expected to exhibit, around one half of the first critical speed in its orbit two loops, as depicted by Fig. 6.15(c). It is also observed a good efficiency of the controller on reducing the rotor orbit of vibration.

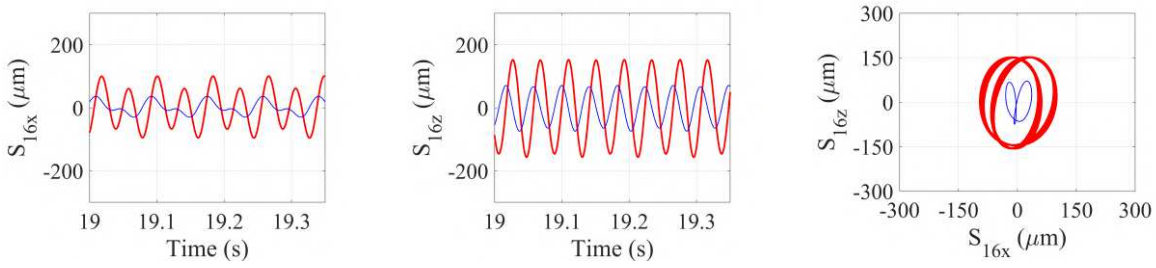

(a) (b) (c)

Figure 6.15: $737\ rev/min$, PID without Filter. Numerical simulation of time domain shaft lateral vibrations, in μm: (—) Control OFF, and (—) Control ON. (a) S_{16_X}; (b) S_{16_Z}; (c) orbit $S_{16_X}\ x\ S_{16_Z}$.

Concerning the numerical simulation of the frequency response, a good amplitude reduction was observed for the $2X$ super-harmonics, especially in the horizontal direction.

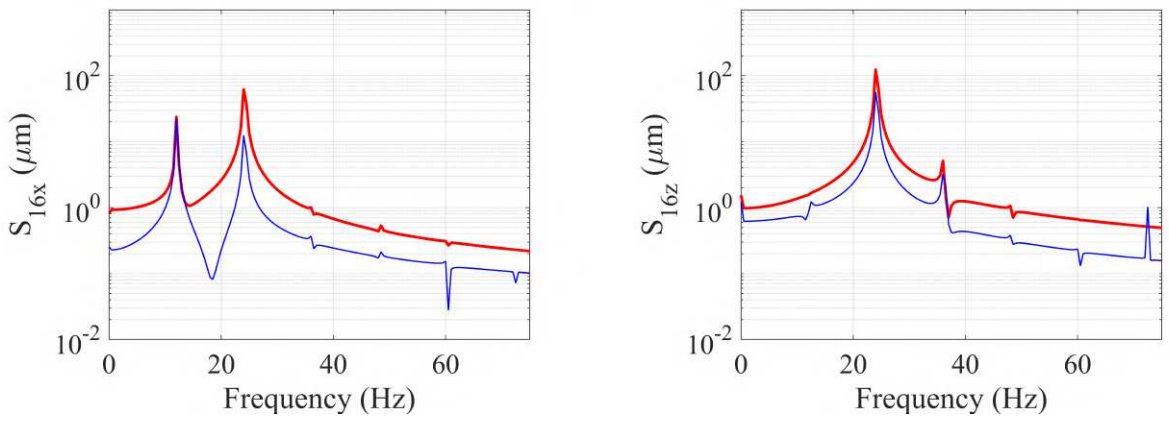

(a) (b)

Figure 6.16: $737\ rev/min$, PID without Filter. Numerical simulatoin of the frequency domain shaft lateral vibrations, in μm: (—) Control OFF, and (—) Control ON. (a) S_{16_X}; (b) S_{16_Z}.

Figure 6.17 presents the numerical simulation results for the control currents, which are found to be around $300\ mA$ and $600\ mA$ at the horizontal and vertical directions, respectively.

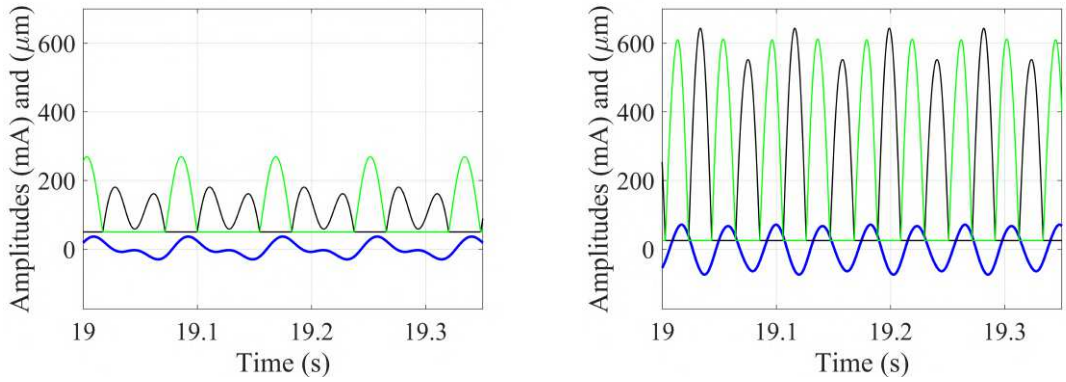

(a) (b)

Figure 6.17: $737\ rev/min$, PID without filter. Numerical simulation for the control currents, in mA and shaft lateral vibrations, in μm. (a) (—) Controlled S_{16_X}, (—) EMA$\#2$, and (—) EMA$\#4$; (b) (—) Controlled S_{16_Z}, (—) EMA$\#1$, and (—) EMA$\#3$.

Figure 6.18 indicates the experimental time responses of the test rig. An uncontrolled orbit possessing two loops is observed for this speed. The control action is

effective, decreasing the rotor orbit and also its harmonics characteristics, which are better seen for the response in the frequency domain in Fig. 6.19.

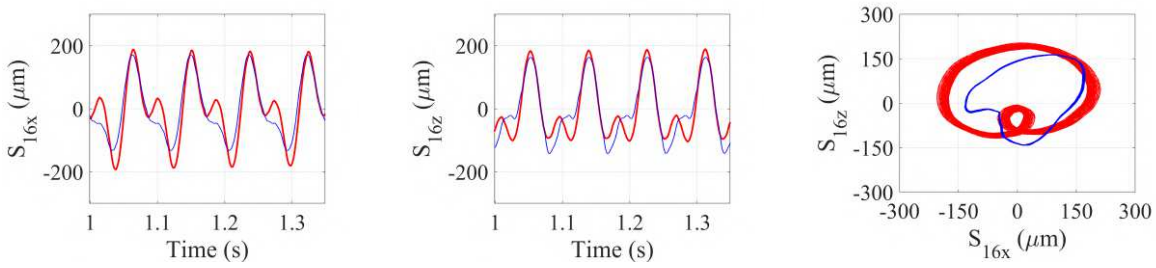

(a) (b) (c)

Figure 6.18: $737\ rev/min$, PID without Filter. Experimental results for the time domain shaft lateral vibrations, in μm: (—) Control OFF, and (—) Control ON. (a) S_{16_X}; (b) S_{16_Z}; (c) orbit $S_{16_X}\ x\ S_{16_Z}$.

As mentioned, Fig. 6.19 represents the experimental responses in the frequency domain of the test rig. An important $2X$ amplitude reduction is observed. Notice that a small increase of $1X$ is seen as a side-effect of the control action. However, it does not represent a problem for the purpose of the present controller, which is simply to reduce the crack effect on the rotating machine.

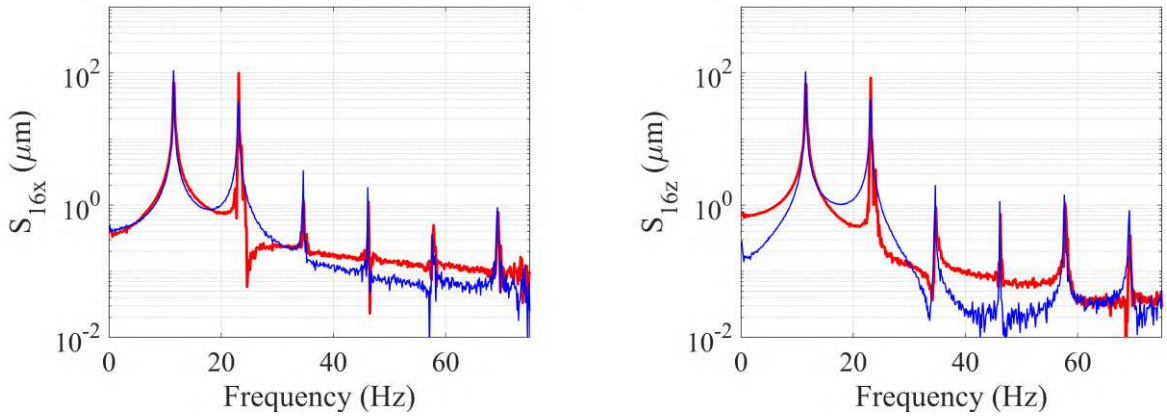

(a) (b)

Figure 6.19: $737\ rev/min$, PID without Filter. Experimental results in the frequency domain shaft lateral vibrations, in μm: (—) Control OFF, and (—) Control ON. (a) S_{16_X}; (b) S_{16_Z}.

Figure 6.20 presents control currents around $600mA$ and $1A$, along the horizontal and vertical directions, respectively. These values are not sufficient to overheat none of the EMAs.

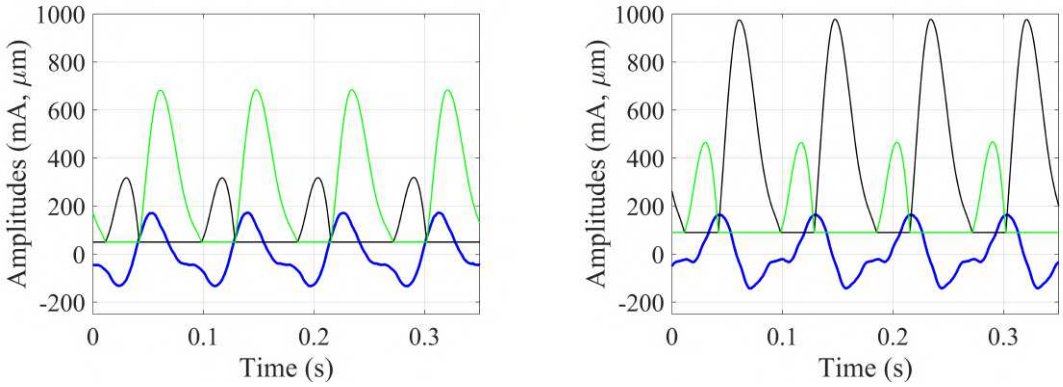

(a) (b)

Figure 6.20: $737\ rev/min$, PID without filter. Experimental control currents, in mA and shaft lateral vibrations, in μm. (a) (—) Controlled S_{16_X}, (—) EMA$\#2$, and (—) EMA$\#4$; (b) (—) Controlled S_{16_Z}, (—) EMA$\#1$, and (—) EMA$\#3$.

c) Speed: $\boldsymbol{\Omega = 900\mathbf{rev/min}}$

For this case, the PID gains used are observed in Tab. 6.3.

Table 6.3: PID gains for $900\ rev/min$ and PID without filter.

	K_P	K_I	K_D
Numerical PID	-250	0	60
Experimental PID	-200	0	1

For the present speed, the numerical model was able to reduce the lateral vibrations of the shaft, as depicted by Fig. 6.21. As the numerical gains are increased, a stronger control effect is observed.

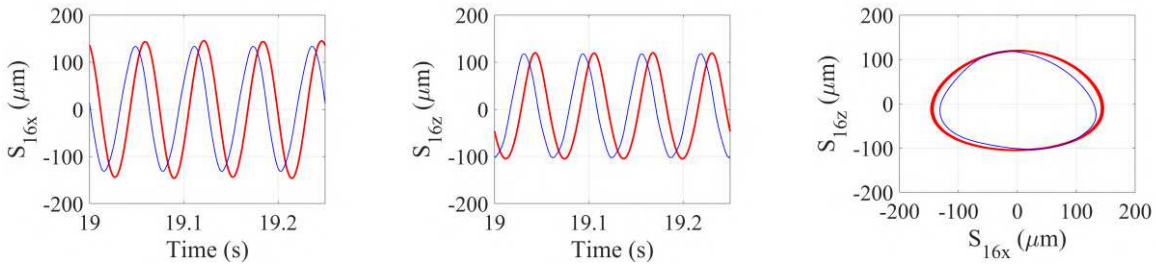

(a) (b) (c)

Figure 6.21: $900\ rev/min$, PID without Filter. Numerical time domain shaft lateral vibrations, in μm: (—) Control OFF, and (—) Control ON. (a) S_{16_X}; (b)S_{16_Z}; (c) orbit S_{16_X} x S_{16_Z}.

Figure 6.22 present the numerical frequency responses. An undesirable increase of the $2X$ super-harmonic is observed in the horizontal direction by the action of the controller. It does not represent a big problem since its amplitude is much smaller than the $1X$ frequency, which suffered a small reduction in its amplitude.

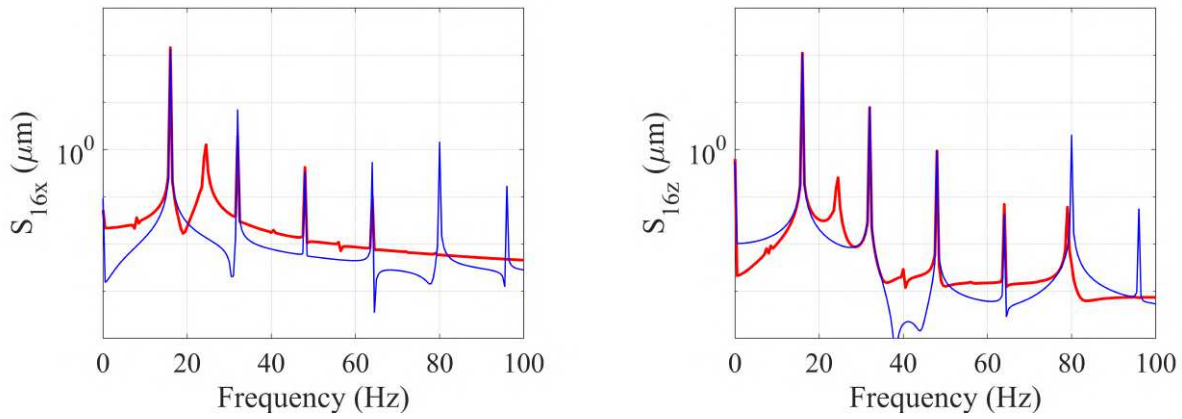

(a) (b)

Figure 6.22: $900\ rev/min$, PID without Filter. Numerical frequency domain shaft lateral vibrations, in μm: (—) Control OFF, and (—) Control ON. (a) S_{16_X}; (b) S_{16_Z}.

Figure 6.23 presents the numerical control currents, which are around 650 and 550 mA for the horizontal and vertical directions, respectively.

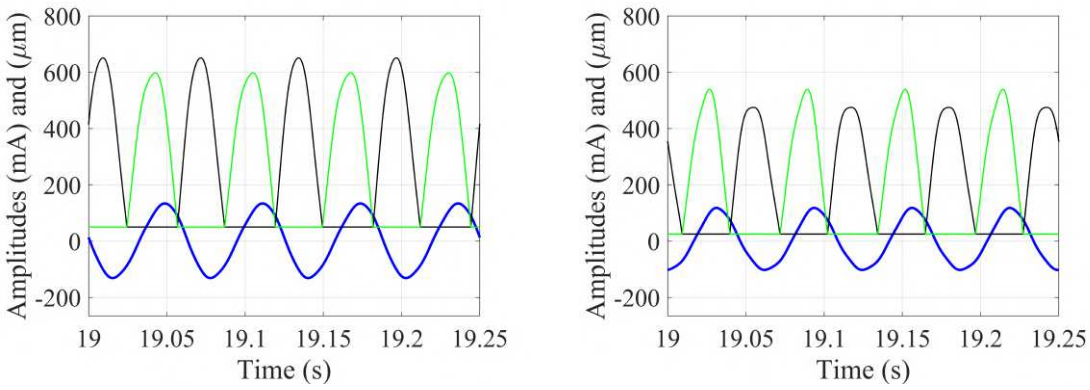

(a) (b)

Figure 6.23: $900\ rev/min$, PID without filter. Numerical control currents, in mA and shaft lateral vibrations, in μm. (a) (—) Controlled S_{16_X}, (—) EMA$\#2$, and (—) EMA$\#4$; (b) (—) Controlled S_{16_Z}, (—) EMA$\#1$, and (—) EMA$\#3$.

The experimental test rig time response is observed in Fig. 6.24. No important time response variation is observed in this case. In the experimental scenario, if the controller gains are increased, the rotor vibrations diverge.

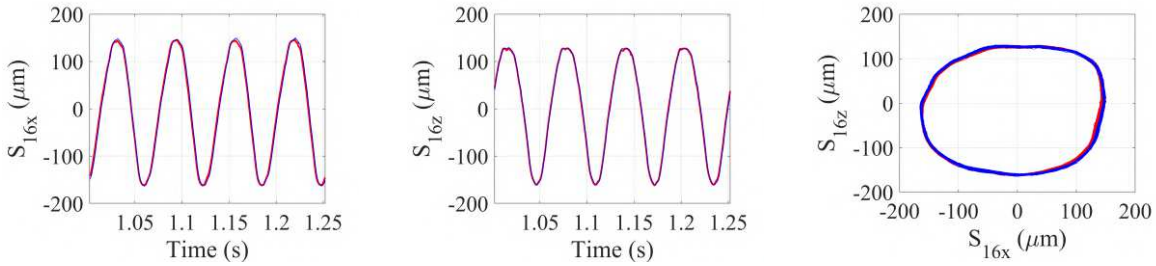

(a) (b) (c)

Figure 6.24: $900\ rev/min$, PID without Filter. Experimental time domain shaft lateral vibrations, in μm: (—) Control OFF, and (—) Control ON. (a) S_{16_X}; (b) S_{16_Z}; (c) orbit $S_{16_X}\ x\ S_{16_Z}$.

Figure 6.25 presents the frequency responses of the experimental test rig. No significant variation is observed, as well.

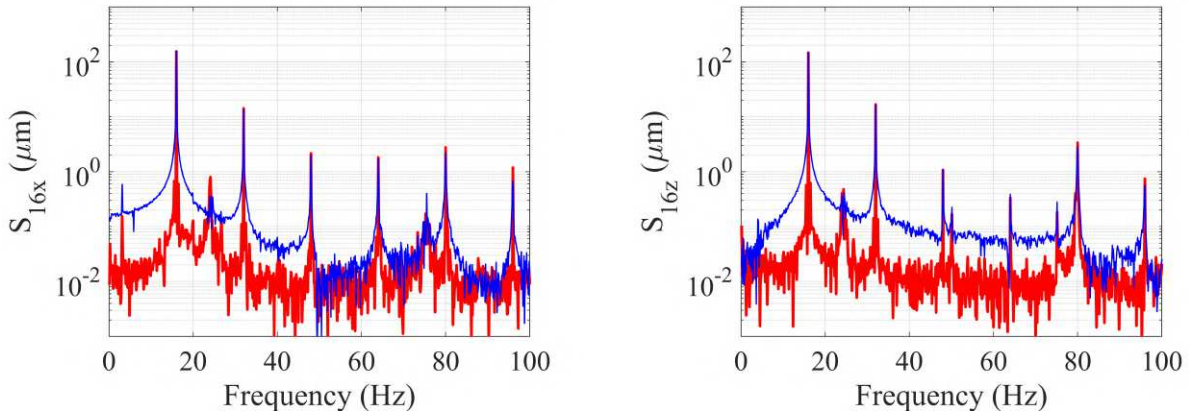

(a) (b)

Figure 6.25: $900\ rev/min$, PID without Filter. Experimental frequency domain shaft lateral vibrations, in μm: (—) Control OFF, and (—) Control ON. (a) S_{16_X}; (b) S_{16_Z}.

Figure 6.26 indicates the control currents used at this case. They are around 500 mA for both horizontal and vertical directions. If they are increased, the rotor response diverges.

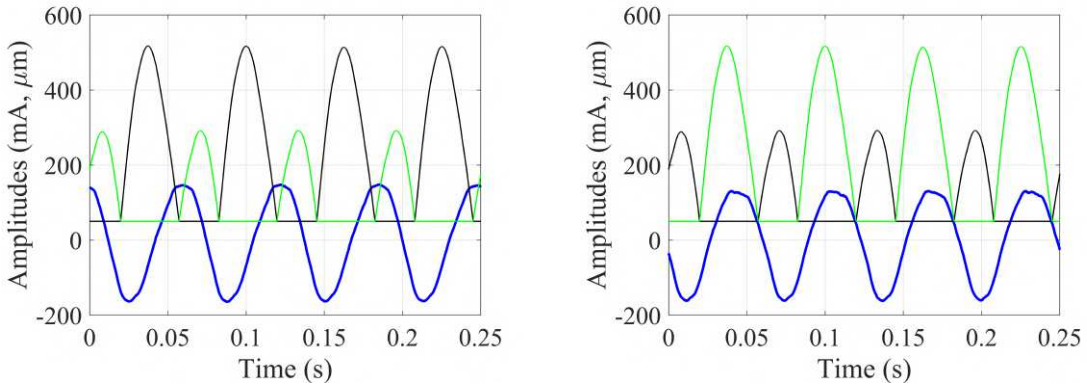

(a) (b)

Figure 6.26: $900\ rev/min$, PID without filter. Experimental control currents, in mA and shaft lateral vibrations, in μm. (a) (—) Controlled S_{16_X}, (—) EMA$\#2$, and (—) EMA$\#4$; (b) (—) Controlled S_{16_Z}, (—) EMA$\#1$, and (—) EMA$\#3$.

6.7.2 Results of the PID with a Bandpass Filter at $2\mathrm{X}$ and $3\mathrm{X}$ super-harmonics

a) Speed: $\boldsymbol{\Omega = \Omega_{crit}/3 = 493 rev/min}$

This section presents the results of the second control law used in the present work. It is an interesting solution to concentrate the control action on the crack signatures $2X$, and $3X$, which are intended to be suppressed. The efficiency of this control law is compared with the previous one, without the filter.

The best PID gains for the present case are presented in Tab. 6.4.

Table 6.4: PID gains for $493\ rev/min$, and PID with a bandpass filter on $2X$ and $3X$.

	K_P	K_I	K_D
Numerical PID	-100	0	8
Experimental PID	-180	0	1

Figure 6.27 presents the time responses of the shaft lateral vibrations for the numerical model. A small reduction of the amplitudes of the time domain response is observed for both the horizontal and the vertical directions.

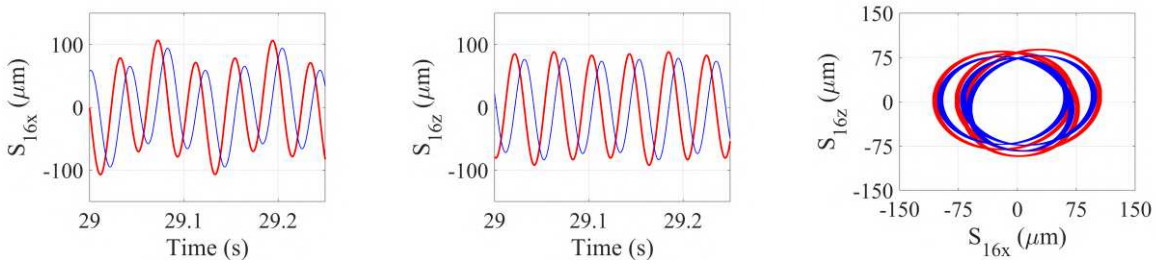

(a) (b) (c)

Figure 6.27: $493\ rev/min$, PID with a bandpass filter for $2X$ and $3X$. Numerical time domain shaft lateral vibrations, in μm: (—) Control OFF, and (—) Control ON. (a) S_{16_X}; (b) S_{16_Z}; (c) orbit $S_{16_X}\ x\ S_{16_Z}$.

In the same way, Fig. 6.28 indicates a small $2X$ and $3X$ super-harmonic reduction for the filtered PID controller of the numerical model.

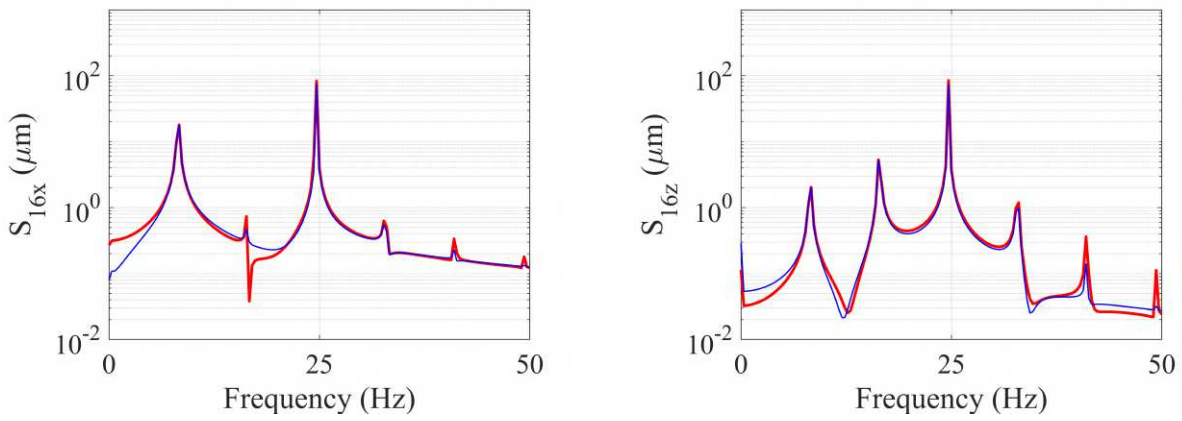

(a) (b)

Figure 6.28: $493\ rev/min$, PID with a bandpass filter for $2X$ and $3X$. Numerical frequency domain shaft lateral vibrations, in μm: (—) Control OFF, and (—) Control ON. (a) S_{16_X}; (b) S_{16_Z}.

Figure 6.29 indicates control currents approximately of 50 and $200\ mA$ for the horizontal and vertical directions, respectively. As these are small, they do not overheat the actuators.

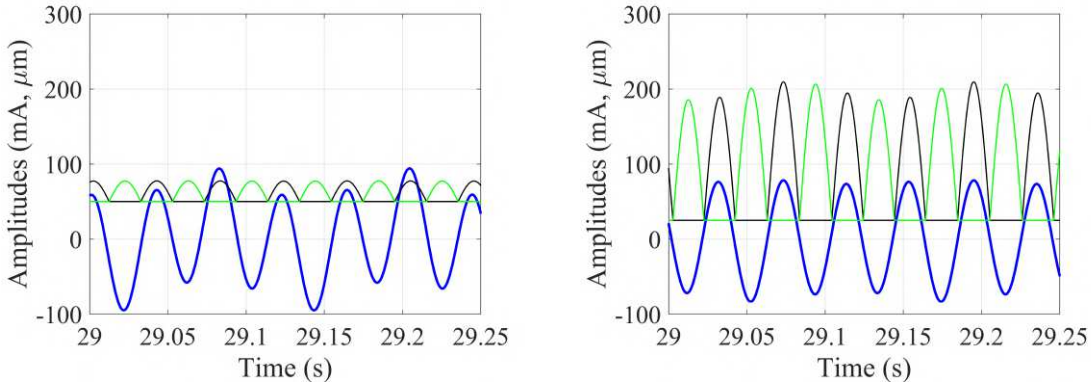

(a) (b)

Figure 6.29: $493\ rev/min$, PID with a bandpass filter for $2X$ and $3X$. Numerical control currents, in mA and shaft lateral vibrations, in μm. (a) (—) Controlled S_{16_X}, (—) EMA$\#2$, and (—) EMA$\#4$; (b) (—) Controlled S_{16_Z}, (—) EMA$\#1$, and (—) EMA$\#3$.

Figure 6.30 presents the time domain responses of the experimental test rig. The time domain lateral vibrations of the controlled case did not change much, compared

with the non-controlled one. However, Fig. 6.30(b) indicates a decrease in the system harmonics, which is well observed in Fig. 6.31.

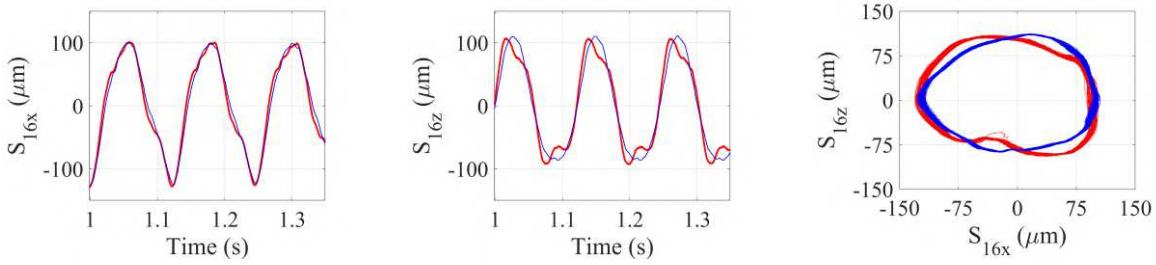

(a) (b) (c)

Figure 6.30: $493\ rev/min$, PID with a bandpass filter for $2X$ and $3X$. Experimental time domain shaft lateral vibrations, in μm: (—) Control OFF, and (—) Control ON. (a) S_{16_X}; (b) S_{16_Z}; (c) orbit $S_{16_X}\ x\ S_{16_Z}$.

As stated, Fig. 6.31 indicates the frequency response functions of the experimental test rig. An important $3X$ amplitude reduction was observed, especially in the vertical direction.

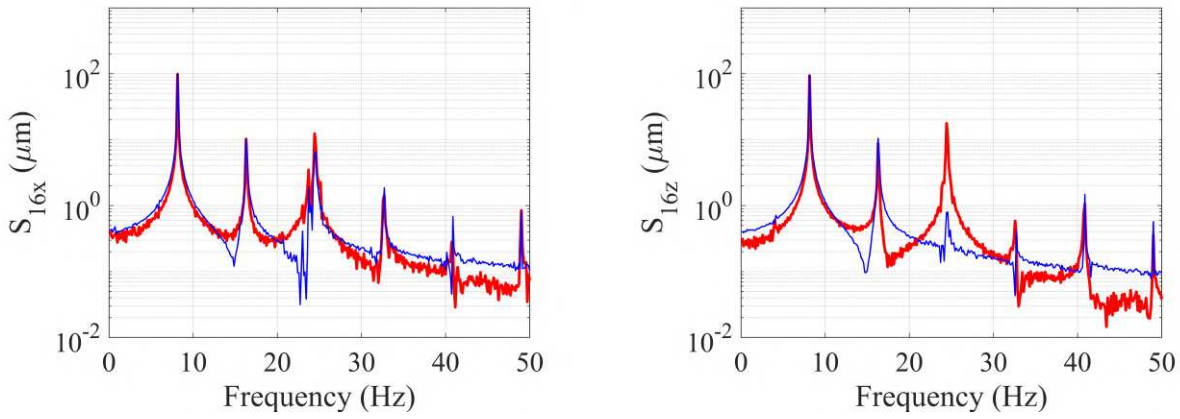

(a) (b)

Figure 6.31: $493\ rev/min$, PID with a bandpass filter for $2X$ and $3X$. Experimental frequency domain shaft lateral vibrations, in μm: (—) Control OFF, and (—) Control ON. (a) S_{16_X}; (b) S_{16_Z}.

Figure 6.32 presents the control currents required for generating the experimental results for this case. These currents are approximately 280 and $220\ mA$ for the horizontal and vertical directions, respectively.

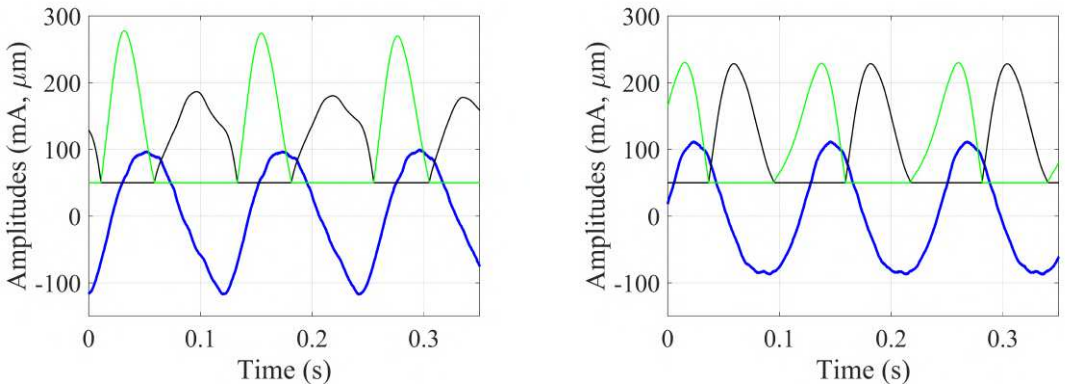

Figure 6.32: $493\ rev/min$, PID with a bandpass filter for $2X$ and $3X$. Experimental control currents, in mA and shaft lateral vibrations, in μm. (a) (—) Controlled S_{16_X}, (—) EMA$\#2$, and (—) EMA$\#4$; (b) (—) Controlled S_{16_Z}, (—) EMA$\#1$, and (—) EMA$\#3$.

b) Speed: $\boldsymbol{\Omega = \Omega_{crit}/2 = 737 rev/min}$

The corresponding PID gains are given in Tab. 6.5.

Table 6.5: PID gains for $737\ rev/min$, and PID with a bandpass filter for $2X$ and $3X$.

	K_P	K_I	K_D
Numerical PID	-200	0	40
Experimental PID	-200	0	1.5

Around one half of the first critical speed, Fig. 6.33 presents the numerical time-domain responses for the shaft. The control action was able to reduce the lateral vibrations, especially in the horizontal direction.

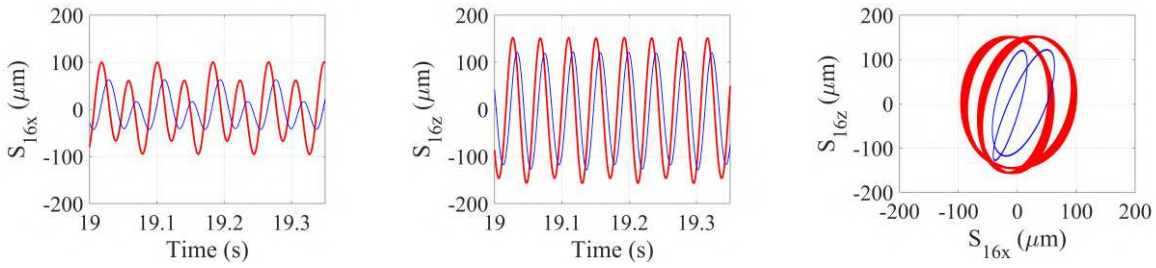

(a) (b) (c)

Figure 6.33: $737\ rev/min$, PID with a bandpass filter for $2X$ and $3X$. Numerical time domain shaft lateral vibrations, in μm: (—) Control OFF, and (—) Control ON. (a) S_{16_X}; (b) S_{16_Z}; (c) orbit $S_{16_X}\ x\ S_{16_Z}$.

Figure 6.34 indicates the same tendency as above, attenuating the $2X$ amplitudes, especially along the horizontal direction.

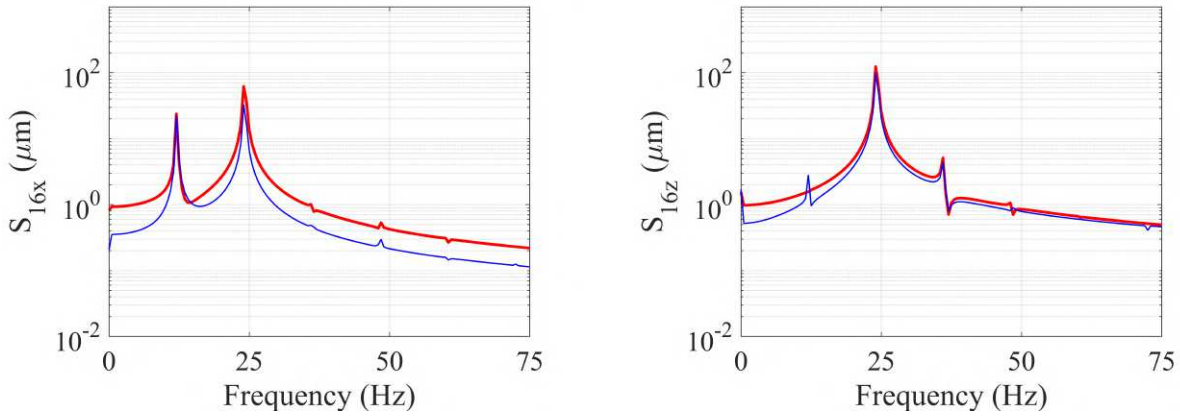

(a) (b)

Figure 6.34: $737\ rev/min$, PID with a bandpass filter for $2X$ and $3X$. Numerical frequency domain shaft lateral vibrations, in μm: (—) Control OFF, and (—) Control ON. (a) S_{16_X}; (b) S_{16_Z}.

The numerical control currents are approximately 200 and $450\ mA$ for the horizontal and vertical directions, respectively.

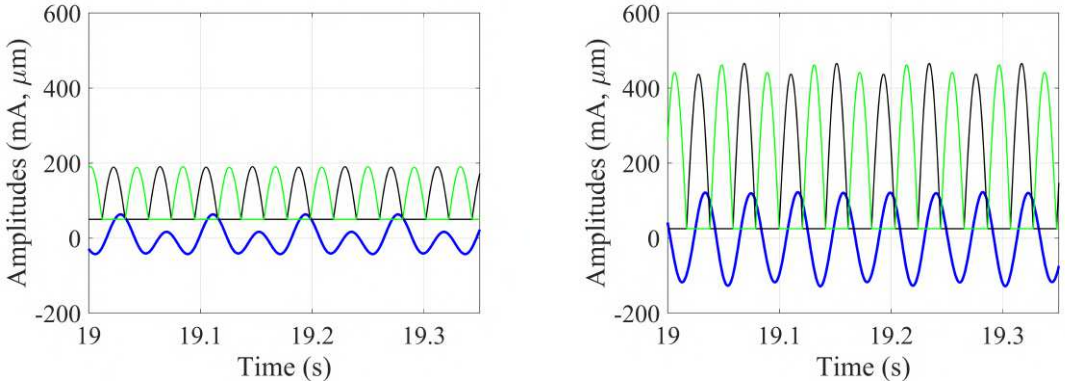

Figure 6.35: $737\ rev/min$, PID with a bandpass filter for $2X$ and $3X$. Numerical control currents, in mA and shaft lateral vibrations, in μm. (a) (—) Controlled S_{16_X}, (—) EMA$\#2$, and (—) EMA$\#4$; (b) (—) Controlled S_{16_Z}, (—) EMA$\#1$, and (—) EMA$\#3$.

Figure 6.36 presents the experimental time domain responses for the present case. Notice that the control action attenuates the vibration amplitudes along the horizontal direction and increases the amplitudes along the vertical direction.

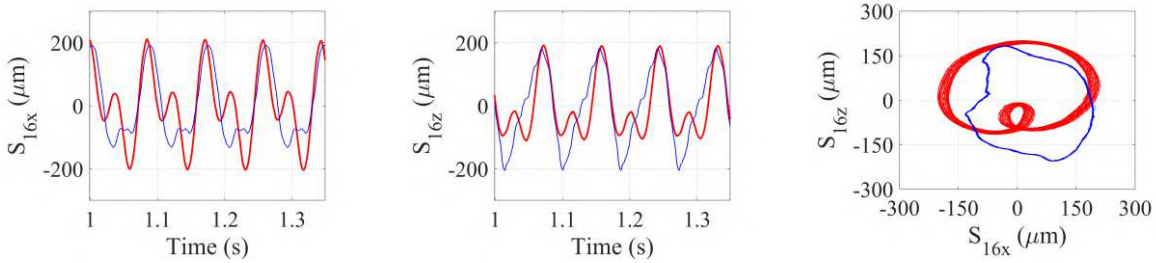

Figure 6.36: $737\ rev/min$, PID with a bandpass filter for $2X$ and $3X$. Experimental time domain shaft lateral vibrations, in μm: (—) Control OFF, and (—) Control ON. (a) S_{16_X}; (b) S_{16_Z}; (c) orbit $S_{16_X}\ x\ S_{16_Z}$.

The experimental frequency responses are depicted in Fig. 6.37. A $2X$ amplitude reduction and a $1X$ amplitude increase are observed, especially in the vertical direction. As mentioned, the increase in the $1X$ frequency is not a problem for this control purpose, which is dedicated to the attenuation of the breathing effect of a transverse crack found in the rotating machine.

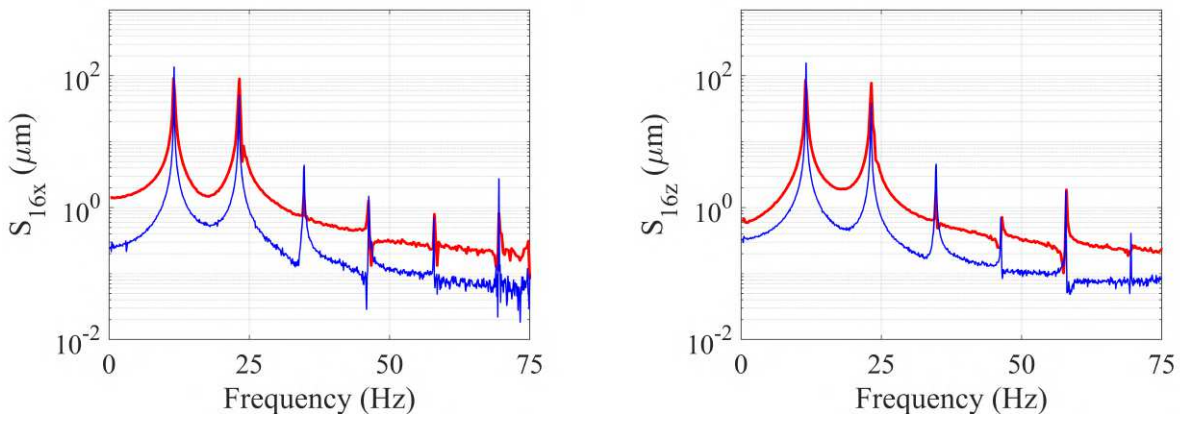

(a) (b)

Figure 6.37: $737\ rev/min$, PID with a bandpass filter for $2X$ and $3X$. Experimental frequency domain shaft lateral vibrations, in μm: (—) Control OFF, and (—) Control ON. (a) S_{16_X}; (b) S_{16_Z}.

Figure 6.38 presents the experimental control current values, which are $1.7\ A$ for both horizontal and vertical directions. This is the highest current value so far, but it still is not capable of overheating the actuators.

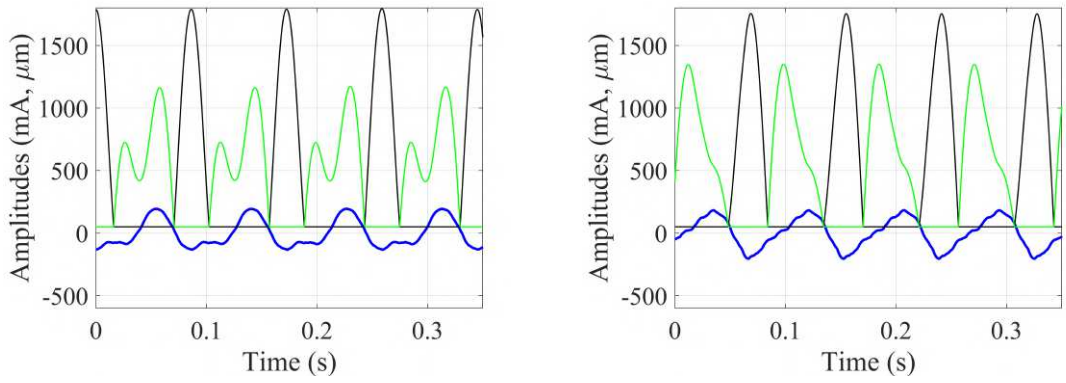

(a) (b)

Figure 6.38: $737\ rev/min$, PID with a bandpass filter for $2X$ and $3X$. Experimental control currents, in mA and shaft lateral vibrations, in μm. (a) (—) Controlled S_{16_X}, (—) EMA$\#2$, and (—) EMA$\#4$; (b) (—) Controlled S_{16_Z}, (—) EMA$\#1$, and (—) EMA$\#3$.

c) Speed: $\boldsymbol{\Omega = 900\mathrm{rev/min}}$

The present speed of rotation is asynchronous (with respect to the critical speeds).

Consequently, the harmonic levels are expected to be low, impairing the control action.

The corresponding PID gains are given in Tab. 6.6.

Table 6.6: PID gains for $900\ rev/min$, and PID with a bandpass filter for $2X$ and $3X$.

	K_P	K_I	K_D
Numerical PID	-1000	0	90
Experimental PID	-400	0	0.4

Figure 6.39 presents the numerical time-domain responses of the FE model. No variation on the time-domain responses was observed when the controller was applied. If the PID gains are increased, no variation is observed.

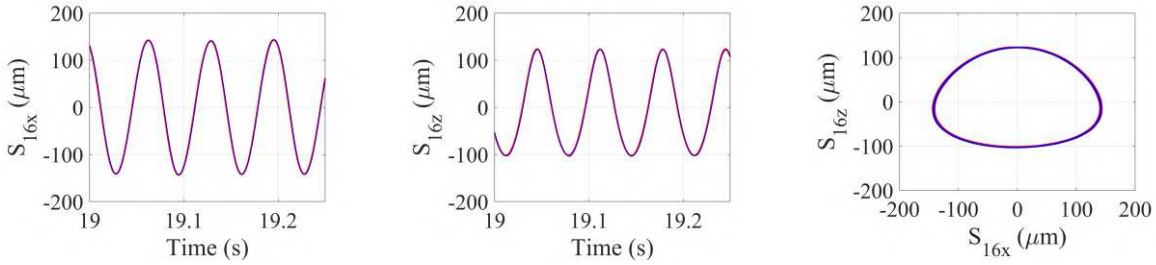

(a) (b) (c)

Figure 6.39: $900\ rev/min$, PID with a bandpass filter for $2X$ and $3X$. Numerical time domain shaft lateral vibrations, in μm: (—) Control OFF, and (—) Control ON. (a) S_{16_X}; (b) S_{16_Z}; (c) orbit $S_{16_X}\ x\ S_{16_Z}$.

The same tendency is observed for the numerical frequency response function of the model.

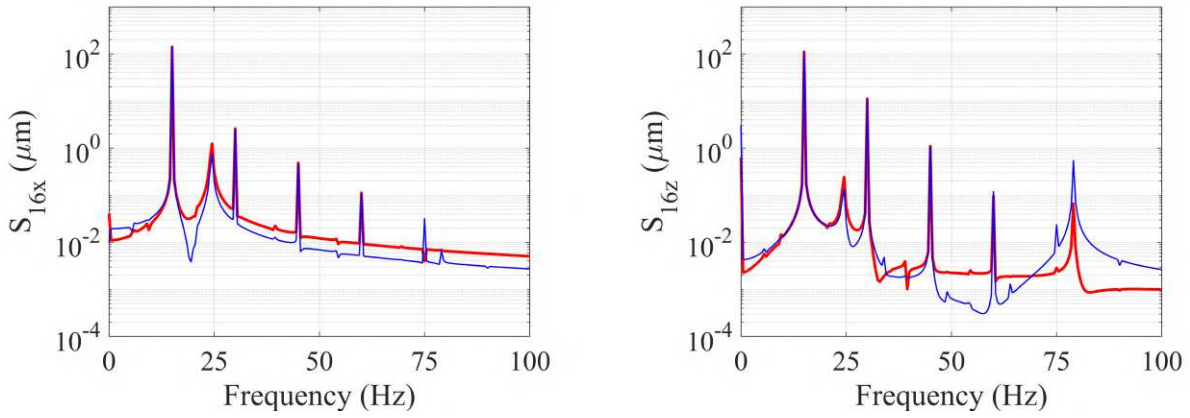

(a) (b)

Figure 6.40: $900\ rev/min$, PID with a bandpass filter for $2X$ and $3X$. Numerical frequency domain shaft lateral vibrations, in μm: (—) Control OFF, and (—) Control ON. (a) S_{16_X}; (b) S_{16_Z}.

Figure 6.41 presents the numerical control currents responses, which are estimated to be approximately 50 and $130\ mA$ along the horizontal and vertical directions, respectively.

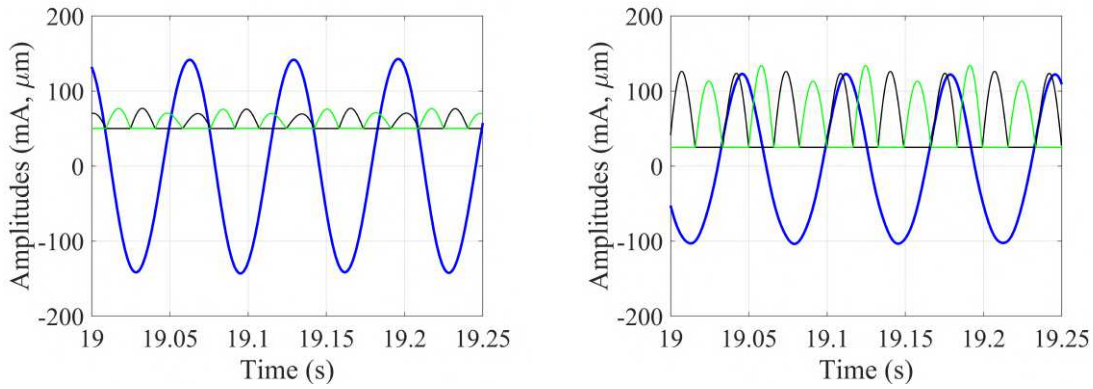

(a) (b)

Figure 6.41: $900\ rev/min$, PID with a bandpass filter for $2X$ and $3X$. Numerical control currents, in mA and shaft lateral vibrations, in μm. (a) (—) Controlled S_{16_X}, (—) EMA$\#2$, and (—) EMA$\#4$; (b) (—) Controlled S_{16_Z}, (—) EMA$\#1$, and (—) EMA$\#3$.

On the other hand, Fig. 6.42 presents the experimental time-domain responses of the test rig. A small increase of the vibration amplitudes is observed, especially in the

horizontal direction.

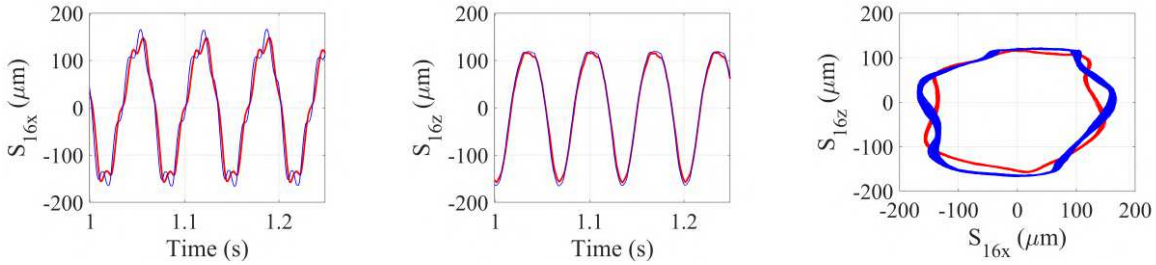

(a) (b) (c)

Figure 6.42: $900\ rev/min$, PID with a bandpass filter for $2X$ and $3X$. Experimental time domain shaft lateral vibrations, in μm: (—) Control OFF, and (—) Control ON. (a) S_{16_X}; (b) S_{16_Z}; (c) orbit $S_{16_X}\ x\ S_{16_Z}$.

Figure 6.43, which represents the experimental frequency responses, indicates an increase in $1X$ and an attenuation in $2X$ amplitudes. As mentioned, an increase in the $1X$ does not represent a problem for the controller to be applied to the present rotating machine.

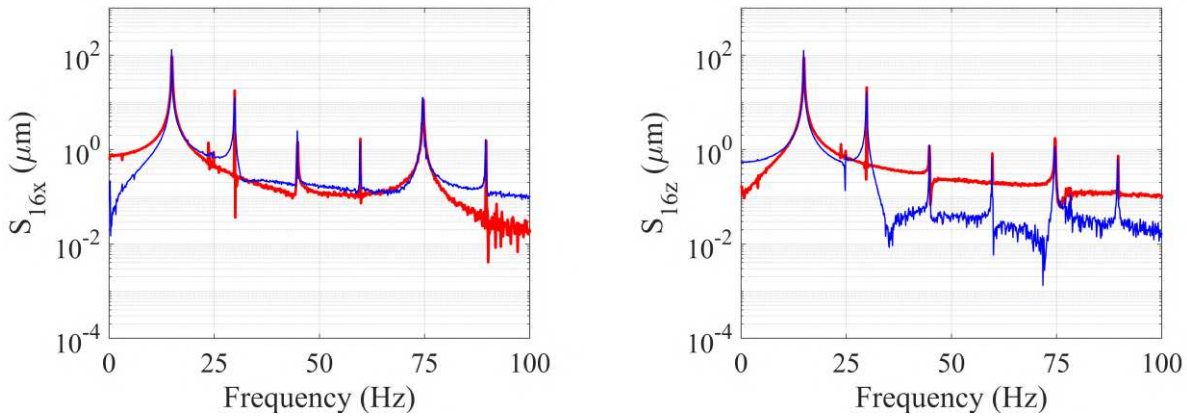

(a) (b)

Figure 6.43: $900\ rev/min$, PID with a bandpass filter for $2X$ and $3X$. Experimental frequency domain shaft lateral vibrations, in μm: (—) Control OFF, and (—) Control ON. (a) S_{16_X}; (b) S_{16_Z}.

Figure 6.44 presents the experimental control currents, which are measured directly on the experimental test rig.They are approximately 450 and $270\ mA$, along the horizontal and vertical directions, respectively.

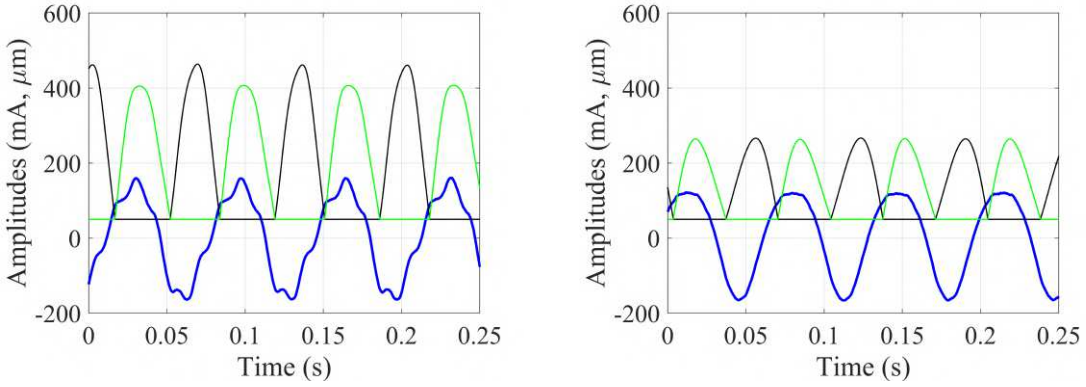

Figure 6.44: $900\ rev/min$, PID with a bandpass filter for $2X$ and $3X$. Experimental control currents, in mA and shaft lateral vibrations, in μm. (a) (—) Controlled S_{16_X}, (—) EMA$\#2$, and (—) EMA$\#4$; (b) (—) Controlled S_{16_Z}, (—) EMA$\#1$, and (—) EMA$\#3$.

6.7.3 Summary of the Results

In this section, all the control results obtained above are compared. On Tab. 6.7, the results of the first PID control law (no filter) are presented. On Tab. 6.8, the results of the second PID control law, which presents a bandpass filter, allowing only for $2X$ and $3X$ super-harmonics are presented.

For one third of the first critical speed, the $3X$ super-harmonic was compared; on the other hand, for the one half of the first critical speed and for the assynchronous speed, the $2X$ super-harmonic was compared.

Table 6.7: Results for the first PID control law.

PID without filter				
Rotor	Horizontal Harmonics Reduction (%)		Vertical Harmonics Reduction (%)	
Speed	Numerical	Experimental	Numerical	Experimental
493	39.1	70.6	51.6	93.3
737	79.9	62.4	54.9	53.3
900	-270	4.3	-4.9	3.1

Table 6.8: Results for the second PID control law.

	PID with bandpass filter for $2X$ and $3X$			
Rotor	Horizontal Harmonics Reduction (%)		Vertical Harmonics Reduction (%)	
Speed	Numerical	Experimental	Numerical	Experimental
493	9.1	46.7	10.8	95.5
737	47.0	43.4	19.6	50.7
900	0.2	26.5	0.1	18.4

By the analysis of both Tab. 6.7 and Tab. 6.8 one can notice that both PID controllers work properly for $493\ rev/min$ and $737\ rev/min$. Moreover, the first PID control law presents better results for these speeds with high values of $2X$ and $3X$ super-harmonics.

However, for $900\ rev/min$, which represents an asynchronous operational rotating speed, the PID with the bandpass filter presented better results. At this speed, the use of the first PID control law is not able to reduce the amplitudes of vibration of the rotor.

In general, the results obtained show that the presence of a filter tends to lead to better efficiency for crack suppression for small levels of $2X$ and $3X$. However, for the cases in which the level of the super-harmonics are higher, the efficiency of the controller is reduced.

In the most part of real rotating machinery applications, including the second control law (with the bandpass filter) is preferable since it is not common to set a rotating machine to operate around its $1/2$ or $1/3$ of its first critical speed.

Chapter 7

Conclusions and Perspectives

This Ph.D. dissertation addressed both crack detection and active crack control as applied to rotating machinery. The existence of a transverse crack along a rotating shaft was simulated by the Mayes model. The linear fracture mechanics theory was applied for relating the crack depth with the corresponding additional shaft flexibility. The crack detection method applied was the so-called modal state observer (MSO). Moreover, the active crack control was performed by a continuous PD controller.

In the first step, a literature review regarding the main vibration-based crack detection methods was presented. The advantage of vibration-based methods, as compared to traditional techniques was highlighted. A brief state-of-the-art, considering the main contributions along the time, as well as some of the main techniques currently applied in the context of the present research work.

Besides, a literature review of the main control techniques was briefly exposed. The passive, semi-active, and active approaches were discussed. The PID technique was finally chosen due to its popularity, efficiency, and simplicity.

The test rig used for crack detection tests was presented, with its main components. In the sequence, a numerical FE model was build and updated with results from the experimental test rig for both time and frequency domains.

In the sequence, a crack detection technique was applied, namely MSO over the updated numerical model. The modal Luenberger observer was presented, and the advantages of this technique were discussed. The Mayes model was applied for simulating the breathing behavior of a transverse crack, existing in a rotating machine. It was explained how to incorporate the crack behavior to the updated numerical model.

The linear fracture mechanics theory was applied for relating the crack depth with the shaft additional flexibility. Both numerical and experimental results were furnished in the form of the kernel density function estimate, which is able to deal with the probability density estimation of a given data sample. The obtained results demonstrated that the estimated modal displacements are more sensitive to the fault existence than the time domain vibration responses of the rotor.

Numerical simulations compared the healthy and faulty shaft conditions. Several crack depths and positions were analyzed for different rotating speeds. The MSO presented better results than the time domain approach for all conditions of incipient cracks, which is the main interest for crack detection. It also proved itself to be less dependent on the crack position, which is another desired characteristic. In the experimental analysis, the breathing crack and open crack conditions were considered. The results followed the same tendency, being the MSO approach more sensitive to fault variation than the time domain vibration responses. The estimated vibration responses by using the MSO do not match perfectly the experimental measurements. Since numerical and experimental conditions of fault detection were different, the most affected vibration modes were found to be different, being mode $\#3$ the most affected in the numerical simulations and mode $\#1$ was the most affected in the experimental simulations. It is worth mentioning that the fault conditions were different and there are some non-modeled dynamics, especially related to bow and misalignment that are not taken into account in the model.

In a general way, the MSO technique demonstrated to be a simple and efficient alternative tool for fault detection in rotordynamics. This technique derived good results for both numerical and experimental tests, which presented a similar tendency, except for the most affected vibration mode, as previously discussed.

Later in the present dissertation, the second test rig, which is devoted to crack control, was presented together with its main components. Similar to the first test rig, a numerical FE model was built, considering the controller that would be applied through electromagnetic actuators (EMAs). Once more, this numerical model was updated with respect to the experimental behavior of the machine, both on time and frequency domains.

The control forces are applied by EMA devices. These actuators are mounted on

a hybrid bearing, which was described accordingly. In the sequence, electromagnetic background theory was revisited. It was presented how the EMA forces were modeled and incorporated into the FE updated numerical model. Also, the nature of the currents to be applied to each EMA was described.

Next, the crack control application regarding both the numerical model and test rig was presented. At this stage, control theory was briefly exposed. Controllability and observability of dynamic systems were discussed, and these concepts were applied to the experimental test rig. Open-loop and closed-loop plants of the second test rig were presented. System stability discussion was performed, and the gain margin and phase margin of the crack control test rig were calculated. This is important for defining a safe range of PD gains to be tested, for avoiding instability behavior during the rotor machine operation.

Finally, the PD controller was discussed, concerning its design for the purpose of crack control. Moreover, both the numerical and experimental results were shown for different rotating speeds and different control laws. For each case considered, the gains used for tuning the PD controller were presented. One reminds that the purpose of the PD controller in the present research work is not to be necessarily robust, nor optimal, but to be able to suppress crack signatures from the rotating machine frequency spectrum. In this way, the controller was presented for various tuning characteristics for different rotor conditions. Moreover, the PD controller does not deal with transient phenomena, being applied only for steady-state conditions. In this sense, the results were derived from two control laws, meaning one control law applying control currents similar to the displacement signals as collected by S_{16_X} and S_{16_Z}, and another control law that used a bandpass filter in the $2X$ and $3X$ frequency range, aiming at concentrating the control action on the crack signatures which are to be suppressed.

The results demonstrated to be satisfactory, being the first control law capable of suppressing crack signatures on $1/2$ and $1/3$ of the first critical speed and not capable of suppressing them on asynchronous operation speeds.

On the other hand, the second control law, through the use of the bandpass filter, was able to deal with asynchronous rotating speeds, reducing significantly crack signatures and reducing the effect of a transverse crack on the dynamic behavior of the rotating machine. This second control law could also suppress crack signatures on $1/2$

and $1/3$ of the first critical speed, but with a smaller efficiency as compared with the first control law. In general, the results showed that the presence of a filter tends to lead to better efficiency for small levels of $2X$ and $3X$ and worse efficiency for high levels of these super-harmonics. Moreover, an interesting point is that the maximum admissible gain values did not present the best results, for crack control purposes, in the vicinity of $1/2$ and $1/3$ of the first critical speed.

This PhD dissertation presents three main contributions: i) proving numerically and experimentally that the use of a Modal State Observer (MSO) increases the efficiency of detecting the existence of a transverse crack along a rotating machine; ii) proving numerically and experimentally that it is possible to reduce the effects of a transverse crack on the frequency response function of a rotating machine, by the use of a hybrid bearing, composed by four electromagnetic actuators (EMAs); iii) start the international collaboration between the laboratories LMEst, at the Federal University of Uberlândia (UFU) and RoMaDyC, at the Cleveland State University (CSU).

As minor contributions, it may be cited: iv) formulation of the numerical codes, using the finite elements method (FEM) for deriving the numerical results for both crack detection and crack control tests; v) building two experimental test rigs, the first being designed for performing procedures of crack detection and the second designed for performing procedures of crack control; vi) the application of an heuristic code for fitting the experimental results with the numerical code; vii) dynamic characterization of the EMAs for understanding their beahvior along the frequency; viii) building and applying Transfer Functions (TFs) to the numerical code which were able to simulate the behavior of the EMAs along the frequency.

Concluding, one may suggest the following perspective issues:

1. Change the hybrid bearing position and /or use two fixed bearings and an electromagnetic actuator at the midspan of the rotor;

2. Implement an optimal controller for the conditions tested in this dissertation, for checking if the efficiency of the control results increases as compared with the results presented in the present research work;

3. Test other asynchronous operation speeds, for checking if the filtered PD controller keeps on deriving good results for crack suppression;

4. Implement a robust controller, aiming at suppressing crack signatures along all the speed range of the rotating machine;

5. Further investigations comparing numerical and experimental results for the MSO approach should be performed, trying to correlate fault severity and operating conditions to the most affected vibration modes of the rotating machine.

References

T. L. Anderson. *Fracture Mechanics: Fundamentals and Applications*. 3rd edition edition, 2005. URL https://doi.org/10.1201/9781420058215.

N. Bachschmid, P. Pennacchi, and E. Tanzi. Identification of transverse crack position and depth in rotor systems. *Meccanica*, 35(6):563–582, 2000. URL https://doi.org/10.1023/A:1010562205385.

A. S. Borges. Controle modal de rotores com mancais magneticos - projeto robusto, 2016.

E. P. Carden and P. Fanning. Vibration based condition monitoring: A review. *Structural Health Monitoring*, 3:355–377, 2004. URL https://doi.org/10.1177/1475921704047500.

A. A. Cavalini-Jr. Monitoramento da integridade estrutural de sistemas mecanicos via observador de estado modal, 2009.

A. A. Cavalini-Jr. *Deteccao e Identificacao de Trincas Transversais Incipientes em Eixos Horizontais Flexíveis de Maquinas Rotativas*. PhD thesis, Universidade Federal de Uberlandia, 2013.

A. A. Cavalini-Jr, V. R. Franco, C. G. Gonsalez, V. Lopes, and G. P. Melo. Noise influence on damage detection through modal state observers methodology. *Trends in Applied and Computational Mathematics*, 2008. URL https://doi.org/10.5540/tema.2008.09.02.0195.

A. A. Cavalini-Jr., F. A. Lara-Molina, T. P. Sales, and V. Steffen-Jr. Uncertainty analysis of a flexible rotor supported by fluid film bearings. *Latin American Journal*

of Solids and Structures, 12:1487–1504, 2015. URL https://doi.org/10.1590/1679-78251582.

A. A. Cavalini-Jr., L. Sanches, N. Bachschmid, and V. Steffen-Jr. Crack identification for rotating machines based on a nonlinear approach. *Mechanical Systems and Signal Processing*, 1:1–14, 2016. URL https://doi.org/10.1016/j.ymssp.2016.02.041.

A. K. Darpe, K. Gupta, and A. Chawla. Coupled bending, longitudinal and torsional vibrations of a cracked rotor. *Journal of Sound and Vibration*, 269:33–60, 2004. URL https://doi.org/10.1016/S0022-460X(03)00003-8.

A. D. Dimarogonas. Vibration of cracked structures: A state of the aart review. *Engineering Fracture Mechanics*, 55(5):831–857, 1996. URL https://doi.org/10.1016/0013-7944(94)00175-8.

A. D. Dimarogonas, S. A. Paipetis, and T. G. Chondros. *Analytical Methods in Rotor Dynamics*. Dordrecht, Netherlands, 2nd edition edition, 2013. URL https://doi.org/10.1007/978-94-007-5905-3.

S. W. Doebling, C. R. Farrar, and M. B. Prime. A summary review of vibration-based damage identification methods. *Shock and Vibration Digest*, 30:91–105, 1998. URL https://doi.org/10.1177/058310249803000201.

M. I. Firswell and J. Penny. Crack modeling for structure health monitoring. *Structural Health Monitoring*, 1(2):139–148, 2002. URL https://doi.org/10.1177/1475921702001002002.

G. Franklin, J. Powell, and A. Emami-Naeini. *Feedback control of dynamic systems*. 7th edition, 880p. edition, 2014.

M. I. Friswell, J. E. T. Penny, S. D. Garvey, and A. W. Lees. *Dynamics of Rotating Machines*. 2010. URL https://doi.org/10.1017/CBO9780511780509.

R. M. Furtado. Desenvolvimento de um atuador magnetico para excitacao sem contato de sistemas rotativos, 2008.

Z. Gajic and M. Lelic. *Modern control Systems Engineering*. Prentice Hall International, London UK, 1996.

R. Gasch. Dynamic behaviour of a simple rotor with a cross-sectional crack. *In: IMechE Conference on Vibrations in Rotating Machinery (Cambridge)*, 178(76):123–128, 1976.

G. Halliday, R. Resnick, and J. Walker. *Fundamentos de Fisica 3*. 7th, rio de janeiro, 379p. edition, 2007.

R. Isermann. Model based fault detection and diagnosis methods. *Proceedings of the American Control Conference*, pages 1605–1609, 1995.

D. Jung and H. DeSmidt. A new hybrid observer based rotor imbalance vibration control via passive autobalancer and active bearing actuation. *Journal of Sound and Vibration*, pages 1–24, 2018. URL https://doi.org/10.1016/j.jsv.2017.11.024.

R. Kalman. A new approach to linear filtering and prediction problems. *Trnas. ASME J. Basic Engineering*, 82:34–45, 1960. URL https://doi.org/10.1115/1.3662552.

E. H. Koroishi. *Controle de Vibracoes em Maquinas Rotativas utilizando Atuadores Eletromagneticos*. PhD thesis, Universidade Federal de Uberlanida, 2013.

E. H. Koroishi, V. Steffen-Jr, and J. Mahfoud. Fuzzy control of rotor system using an electromagnetic actuator. *MATEC Web of Conferences 1*, 2012. URL https://doi.org/10.1051/matecconf/20120109003.

M. Lallane and G. Ferraris. *Rotordynamics Prediction in Engineering*. 2nd edition, 1997.

L. S. Leao, A. A. Cavalini-Jr, T. S. Morais, G. P. Melo, and V. Steffen-Jr. Fault detection in rotating machinery by using the modal state observer approach. *Journal of Sound and Vibration*, 458:123–142, 2019. URL https://doi.org/10.1016/j.jsv.2019.06.022.

D. G. Luenberger. Observing the state of a linear system. *IEEE Transactions on Military Electronics*, 9:74–80, 1964. URL https://doi.org/10.1109/TME.1964.4323124.

R. Market, R. Platz, and M. Seidler. Model based fault identification in rotor systems by least squares fitting. *International Journal of Rotating Machinery*, 7(5):311–321, 2001. URL https://doi.org/10.1155/S1023621X01000264.

I. W. Mayes and W. G. R. Davis. The vibrational behaviour of a cracked shaft containing a transverse crack. *IME Conf. Vibrations in Rotating Machinery*, 168(6), 1976.

L. Meirovitch. *Dynamics and Control of Structures*. 1990.

T. H. Mohamad, Y. Chen, Z. Chaudhry, and C. Nataraj. Gear fault detection using recurrence quantification analysis and support vector machine. *Journal of Software Engineering and Applications*, 11:181–203, 2018a. URL https://doi.org/10.4236/jsea.2018.115012.

T. H. Mohamad, M. Samadani, and C. Nataraj. Rolling element bearing diagnostics using extended phase space topology. *Journal of Vibration and Acoustics*, 140, 2018b. URL https://doi.org/10.1115/1.4040041.

T. H. Mohamad, A. A. Cavalini-Jr, V. Steffen-Jr, and C. Nataraj. Detection of cracks in a rotating shaft using density characterization of orbit plots. *K.L. Cavalca, H.I. Weber (Eds.), Proceedings of the 10th International Conference on Rotor Dynamics – IFToMM*, 2:90–104, 2019. URL https://doi.org/10.1007/978-3-319-99268-6_7.

T. S. Morais. *Contribuicao ao Estudo de Maquinas Rotativas na presenca de naolinearidades*. PhD thesis, 2010.

T. S. Morais, V. Steffen-Jr, and J. Mahfoud. Control of the breathing mechanism of a cracked rotor by using electro-magnetic actuator: numerical study. *Latin American Journal of Solids and Structures*, 9:581–596, 2012. URL https://doi.org/10.1590/S1679-78252012000500004.

T. S. Morais, D. Hogapian, V. Steffen-Jr, and J. Mahfoud. Modeling and identification of electromagnetic actuator for the control of rotating machinery. *Shock and Vibration*, 20:171–179, 2013. URL https://doi.org/10.1155/2013/473072.

T. Pafelias. Dynamic behavior of a cracked rotor, 1974.

C. A. Papadopoulos. Some comments on the calculation of the local flexibility of cracked shafts. *Journal of Sound and Vibration*, 278:1205–1211, 2004. URL https://doi.org/10.1016/j.jsv.2003.12.023.

E. A. Ribeiro, J. T. Pereira, and C. A. Bavastri. Passive vibration control in rotor dynamics: Optimization of composed support using viscoelastic materials. *Journal of Sound and Vibration*, 2015. URL https://doi.org/10.1016/j.jsv.2015.04.007.

P. N. Saavedra and L. A. Cuitiño. Crack detection and vibration behavior of cracked beams. *Computers and Structures*, 79:1451–1459, 2001. URL https://doi.org/10.1016/S0045-7949(01)00049-9.

M. Samadani, C. A. K. Kwuimy, and C. Nataraj. Model-based fault diagnostics of nonlinear systems using the features of the phase space response. *Communications in Nonlinear Science and Numerical Simulation*, 20:583–593, 2015. URL https://doi.org/10.1016/j.cnsns.2014.06.010.

J. T. Sawicki, M. I. Friswell, Z. Kulesza, A. Wroblewski, and J. D. Lekki. Detecting cracked rotors using auxiliary harmonic excitation. *Journal of Sound and Vibration*, 330:1365–1381, 2011. URL https://doi.org/10.1016/j.jsv.2010.10.006.

R. A. Serqay and J. W. Jewett-Jr. *Principios de fisica: Eletromagnetismo*, volume 3, 941p. 2008.

J. D. Simon and S. K. Mitter. A theory of modal control. *Information and Control*, 13: 316–353, 1968. URL https://doi.org/10.1016/S0019-9958(68)90834-6.

S. Skogestad and I. Postlethwaite. *Multivariable Feedback Control*. 2nd edition edition, 1996.

S. Skogestad and I. Postlethwaite. *Multivariable Feedback Control*. 2005.

R. Storn and K. Price. Differential evolution: A simple and efficient adaptative scheme for global optimization over continuous spaces. *International Computer Science Institute*, 12:1–16, 1995.

F. A. C. Viana, F. C. G. Oliveira, J. A. F. Borges, and V. S. Jr. Differential evolution appplied to the design of a three-dimensional vehicular structure. In *International Design Engineering Technical Conferences and Computers and Information in Engineering Conference*. Las Vegas, Nevada, 2007. URL https://doi.org/10.1115/DETC2007-34290.

J. Zhao. Vibration based damage identification of time-varying dynamical systems, 2013.